New Materials & Processes for Radiation Detection

Andrew James Blue

UNIVERSITY
of
GLASGOW
Department of Physics and Astronomy

Thesis submitted for the degree of Doctor of Philosophy

31st March 2005

Abstract

Semiconducting materials have been used for over 40 years, with the majority of work focussing on the use of silicon. This thesis details the work done on the development of novel radiation detectors. Fabrication processes for the production of GaN diodes were developed using both e-beam and photolithographic techniques. Devices were fabricated on a range on GaN wafers, and were electrically characterised by CCE and I-V measurements. Defect characterisation was performed using microwave absorption (MWA), thermally stimulated current (TSC) and photoluminescence (PL) techniques. A common defect with activation energy of ∼0.67 eV was found for two types of Emcore grown GaN material using both TSC and MWA measurements. The variety of trap levels found throughout the materials is consistent with previous results, suggesting numerous and material dependent defect levels in thin GaN films. Photoluminescence spectra were also used to determine the molar fraction of Al present in an Emcore AlGaN wafer, which was found to be ∼ 10%. PL was also able to show that increasing TMG flow rates in MOCVD growth can significantly increase both point and dislocation defects. The activation of Compound Semiconductor Technologies (CST) grown Magnesium doped GaN was also verified using PL spectra.

Tokushima grown GaN Schottky 1 mm diameter pad detectors were tested for its suitability as a detector for the super Large Hadron Collider (sLHC)

in which the estimated 10 year hadron fluence is up to 1x10^{16} cm^{-2}. The charge collection efficiency was observed to drop to 62% after the material was irradiated with a neutron fluence of 10^{14} ncm^{-2}, to 6% after 10^{15} ncm^{-2}, and then to 4.5% after 10^{16} ncm^{-2}. The charge collection efficiency dropped to 14% after 10^{16} pcm^{-2}. Leakage currents after all irradiations remained in the 10^{-11} A region at a bias voltage of 15 V. Characterisation of radiation induced defects were indicates an increase in non-radiative recombination centres. This was shown through a decrease in photoluminescence peaks, and through the decrease in the instantaneous carrier lifetimes from MWA and PC measurements. An increase in asymptotic lifetimes suggests that excess carriers undergo a multi-trapping process after irradiation. PL measurements also indicate a rapid decrease in intensity for the yellow band peak, indicating a transformation of point defects into non-radiative centres. Dislocation defects appear to be unchanged with irradiation.

Emcore grown GaN and AlGaN wafers were also investigated for use as a photon (UV) detector. Novel interdigitated metal-semiconductor-metal (MSM) contacts were successfully fabricated utilising finger spacings of 25, 50 and 100 μm. Such detectors have been optimised for the metal contact schemes used for Schottky contacts, allowing for the possibility to use Pd contacts for semi-transparent contacts. Experiments showed that the leakage current could be reduced by decreasing the finger pitch of interdigitated MSM diodes. A ratio of 1000:1 is seen for levels of photocurrent against dark current. Full UV characterisation of the diodes showed a responsivity of ~30 mA/W when operated unbiased, which remained relatively flat across the bandgap. A design for the first ever position sensitive GaN UV detector utilising interdigitated finger diodes is proposed. Such a detector is suitable for energy dispersive Circular Dichroism (CD) measurements used in conjunction with the Synchrotron Radiation Source at Daresbury. The finished design allows the diodes to be separated by distances of millimetres, whilst the detective quantum efficiency will be determined by the pitch of the fingers. The detector can also be operated unbiased.

To allow for the fabrication of so-called 3D Schottky detectors, etch recipes used with an STS ICP etch system for the creation of uniform diameter, fine pores in silicon were optimised. A maximum aspect ratio of 14:1 was achieved for 10 μm diameter holes. Work done on parameter ramping has allowed the possibility to increase this ratio. 3D detectors fabricated using this modified recipe showed a drop from 60% to 5% after irradiation with 4.5×10^{14} pcm^{-2}. An alternative version of this recipe was used for the creation of several novel devices, including a silicon mask for metal contacts, and a microfluidic mixing device. Work was also completed on the first ever switched process etching of GaAs using a non-carbon based chemistry. Aspect ratios of 4.5:1 were achieved for 10 μm holes in this material.

.

"If you understood everything I said, you'd be me"

Miles Davis

Acknowledgements

This work would not be have been done if it weren't for the help of a number of people in the Detector Development group and the Electrical Engineering Dept at Glasgow, and especially those who have supervised my work over the past 3 (and a bit) years - **Mahfuzur** and **Val**. I would also like to thank **Ken** for his help in his (multiple) corrections and to **Jon Cooper** for his support as my second supervisor. I must also thank PPARC for my funding and Surface Technologies Systems for their sponsorship, especially **Leslie Lea** and **Ian Johnston**.

A big thanks must also be given to **Liam** for being an unpaid supervisor/teacher, an above average office mate and for not shouting at me for all the stupid questions I have asked him over the years, and to **James** who has assisted me "big style" in the GaN work and the drinking of Eastern European beer. While on the subject of office mates, I'd like to say thanks to **Steve**, **Adwan**, **Pamela** and **Vic** for not telling me to turn the music down too often.

I'd also like to thank the numerous technicians who have made my life a lot easier. These include **Fred** , **John**, **Meg** and **Lina** from the Detector group and those from the dry etch, bio, nano & optics labs at engineering, especially **Haiping**, **Margaret**, **Linda**, **Eve** and **Dave**.

I have been able to do a large part of this work through association with

certain lovely people at Vilnius University. A big thanks goes to **J. Vaitkus**, **E. Gaubas**, **Vidmantkus**, **Paulos**, and of course **Marius**. Thanks to Marius, I have now fulfilled my lifelong dream of seeing a modern interpretation of a (still to this day) unknown Shakespeare play in Lithuanian. Closer to home (ie RAL), **Spyros** was invaluable for his help with the UV detection section of my work.

I've had great help from nearly all those I've worked with over the past years, whether it be helpful advice from **Richy**, **Giulio**, **Patrick**, **Keith** or **Chris Parkes**, playstation action with **Dave D** or a friendly pint down the pub with **Julien**, **Stan**, **Christian** or **Gav** or many caparinis on a tropical island in Brazil with **Chris Adams**. Shabba!

I would not have managed to get through this past while (on and off the field) without **Francesco**. He was there to help take results during the day, and there to share a drink with whilst I complained nothing was working. As we both always seemed to be around the dept post 6pm, we successfully managed to work our way through most of the restaurants and pubs in Glasgow. Only Optimo remains! Cheers Francesco.

Over the last 3 years (and counting) I haven't managed to meet a better bunch of friends as **John** and **Tatjana**. Whether it was regular trips for lunch (strictly 12pm), sessions of silent hill into the "wee small hours", support in the more depressing times of a PhD, or the hospitality they've shown to me in my visits to their homes both in Glasgow and Munich, they have been nothing short of being "pure magic". Without this work, I could not have made such good friends and for that I am thankful.

Finally, I thank those I could turn to when I didn't want to talk about Schottky barriers: my family, my friends **Ally**, **Colin** and **Anthony** (what-ever continent he may be on now), fellow sputniks **David**, **Martyn** and **Nicky** and my lovely girlfriend **Clare** who has put up with me going on about Schottky barriers these past 3 years (and a bit).

End the praise. Thanks for your attention. God Bless and goodnight.

Declaration

Except where explicit reference is made to the work of others, this dissertation is the result of my own work. None of this material has been submitted for any other degree at the University of Glasgow or any other institution.

A Blue

Contents

6 UV GaN detectors 121

List of Figures

List of Tables

Chapter 1

Introduction

For the last 40 years, silicon has been the most commonly used semiconducting material for radiation detectors. However, in recent times there has been an increased interest in the study of alternative semiconducting materials. In this thesis, work will be presented on the process development, fabrication and evaluation of new materials: namely the semiconductor gallium nitride (GaN) as a material for detecting both particle and ultraviolet (UV) radiation. Furthermore, work has been done on deep reactive ion etching (DRIE) processing of silicon in order to fabricate 3D detectors - an alternative diode geometry using a standard semiconducting material. This section will now provide a background to the history of these detectors and the processes necessary for their production.

1.1 Gallium Nitride

Gallium nitride (GaN), along with AlN & InN, are III-nitride semiconductors. These materials are characterised by a wide bandgap. (E_g = 3.39, 6.2 & 1.97 eV respectively). Selected electrical and material properties of GaN are given in Table 1.1 along with those of Si, GaAs and another wide bangap

	Si	GaAs	GaN	4H-SiC
Bandgap (eV)	1.12	1.4	3.39	3.3
Bandgap Type	Indirect	Direct	Direct	Indirect
Crystal Structure	Diamond	Zincblende	Wurtzitic	Wurtzitic
Density (gcm^{-3})	2.328	5.32	6.15	3.2
Mobility ($cm^2V^{-1}s^{-1}$) μ_e	1500	8500	1000	900
μ_h	450	400	30	20
Breakdown Field (Vcm^{-1})	3×10^5	4×10^5	3×10^6	3×10^6
Thermal Conductivity ($Wcm^{-1}K^{-1}$)	1.5	0.46	1.5	4.9

Table 1.1: Selected electrial and material properties of various semiconductors

semiconductor, 4H-SiC. GaN was first synthesised in 1938 by Juza and Hahn [1]. It was not until 1969 that the first generation of large area layers on sapphire substrates was achieved [2]. In recent years, however, there has been a great increase in the study of such III-Nitride semiconductors, primarily due to their direct, wide bandgaps. It was only in 1990 that the first AlGaN substrate was fabricated [3]. For $Al_xGa_{1-x}N$, the bandgap is calculated as

$$E_g(x) = E_gGaN(1-x) + E_gAlN(x) - bx(1-x) \tag{1.1}$$

where E_gGaN = Bandgap of GaN, E_gAlN = Bandgap of AlN, x = molar fraction of Al and b is the "bowing" parameter (∼0.8 [4]).

1.2 GaN as a Radiation Detector

The ability to fabricate such ternary alloys gives GaN a major advantage for radiation detection. The bandgap of GaN, along with its ternary and quarternary compounds (eg InGaN, which was created in 1993 [5]), span the continuous range of the electromagnetic spectrum, making such a material suitable for applications such as high-brightness light emitting diodes and lasers [6, 7].

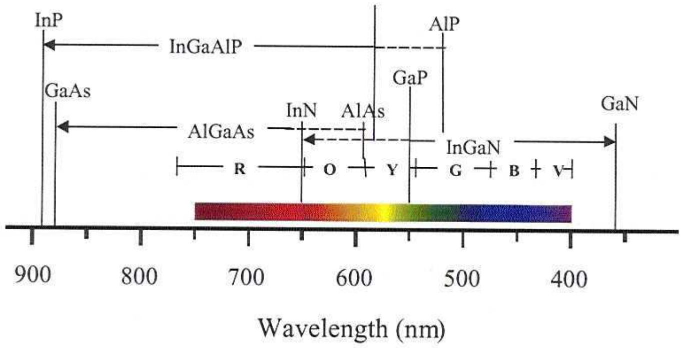

Figure 1.1: The various ternary and quarternary materials used for LED's with the wavelengths indicated

Additionally, as GaN has a bandgap of 3.39 eV, its maximum detectable wavelength is

$$\lambda_{CUT} = \frac{hc}{E_g} = \frac{1.24\mu m}{3.39eV} = 340nm \tag{1.2}$$

The high bandgap material is not sensitive to visible light and ensures that GaN has a higher signal-to-noise ratio for UV detection than, for example, silicon. By adding varying fractions of Al, the bandgap can be adjusted to ensure the detector is completely "solar blind", so that no filters are required. This work describes the investigation of (Al)GaN as a UV detecting material, outlining both e-beam and photolithographic fabrication processes developed for the production of UV detectors from (Al)GaN. Such detectors will be shown to be a viable option for use in protein folding experiments such as circular dichroism (CD).

GaN is also suitable for high temperature and high power electronics [8]. Due to its high density and breakdown field [9], GaN has also recently been thought of as a possible alternative to silicon as a particle detector for use in harsh radiation environments [10]. Its use as a particle detector for the Large Hadron Collider (LHC) and its possible upgrade, sLHC, were investigated through the irradiation of GaN with neutrons, protons and X-rays. Fluences of up to 1×10^{16} particles cm^{-2} were used, and subsequent changes in operating efficiencies of the devices shown.

1.3 Defect Characterisation

As GaN is a relatively new material, it is necessary to study the defects that may be present in the crystal lattice, and their possible influences on its operating performance. For (Al)GaN, the defect density is thought be as high as $10^{15}cm^{-2}$ [11]. As well as being caused by impurities, the vast majority of these defects are thought to be structural defects, introduced at the growth stage. In this work, various types of GaN were investigated for their as-grown defects. Furthermore, radiation induced defects were also studied with a view to determine their possible detrimental consequences. Evaluation of such defects will be shown through studies of photoluminescence (PL), microwave absorption (MWA), photoconductivity (PC) and thermally stimulated currents (TSC).

1.4 ICP etching

The final chapter in this work will detail investigations of the improvement of the deep reactive ion etching (DRIE) dry etching of silicon and gallium arsenide using a Surface Technology Systems (STS) [12] inductively coupled plasma (ICP) tool. Such technology makes possible the fabrication of a new geometry of detector - the 3D detector. "3D" detectors are thought to be a viable alternative to standard planar technologies, with applications ranging from X-ray detection to a future extremely radiation hard detector for the LHC.

Chapter 2

Fabrication techniques

2.1 Introduction

This chapter will discuss the main processes that are involved in the fabrication of both semiconductor and MEMS (Micro-Electro-Mechanical Systems) devices. These include lithography (both optical and e-beam), surface preparation, thin film deposition and lift-off. There is also an explanation of the processing of 3D silicon devices using dry etching techniques and the accompanying plasma theory that forms the basis of such a process.

2.2 Lithography

Lithography is used to transfer a pattern of geometrical shapes onto the surface of a substrate. It transfers this pattern via a layer of resist, which is applied to the surface of the substrate then exposed to the pattern and developed. From this stage, the substrate can be etched, or metal can be applied using the shape of the patterned resist. Several techniques for lithography exist using sources ranging from optical (UV) to non-optical (e-beam, protons, X-ray). Each technique has particular advantages, such as resolution (minimum feature size), registration (minimum overlay accuracy of 2 or more patterns) or pattern transfer time. Consequently, two different structures might require their own lithographic method, depending on their specific requirements. In this work, the fabrication of UV GaN detectors was carried out using e-beam and optical lithography, while devices made in silicon for 3D structures other devices used only optical lithography techniques.

2.2.1 Photo lithography

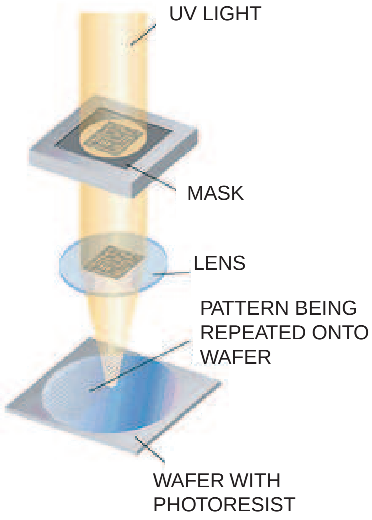

Figure 2.1: Schematic diagram of optical lithography

Optical lithography (or photolithography) transfers patterns onto a resist-covered substrate using ultraviolet light. The resist is exposed to UV light through a mask bearing the desired pattern (Fig 2.1). Therefore - for a positive resist - the only areas of resist exposed to the light are those beneath the transparent sections of the mask. As the resist is light sensitive, its chemical properties change when exposed to the light. After washing the sample in a developing fluid, the areas of resist that were exposed to the UV dissolve, leaving the remaining resist on the sample in the shape of the mask design.

There are two ways of performing photolithography; contact printing, and projection printing. For contact printing, the mask is in contact with the sample, whereas for projection printing, the mask is a distance away from the sample and lenses are used to focus the light through the mask. For contact printing, there is no need for expensive optics but the transferred pattern is affected by any inhomogeneities in the resist thickness. This does not occur in projection systems where there is also less defect generation as the mask and sample are not in contact. For these reasons, projection printing is preferentially used in industry, and was the method used in this work.

Photoresist

A photoresist is composed of 3 compounds: a base resin, a photosensitive component and an organic solvent. The photosensitive components are made up of long chain carbon polymers, and come in two polarities: negative and positive (Fig 2.2). For positive resists (which was the polarity of resist used in this work), these long chain molecules break up under exposure to UV light (chain scission), with the exposed areas dissolving more quickly in developing fluid. For negative resists, several polymer chains tend to join together under UV exposure (cross-linking), resulting in exposed resist dissolving at a slower rate.

The type of resist which is chosen depends on the resist's sensitivity, which is a measure of the amount of light energy needed to create a chemical change

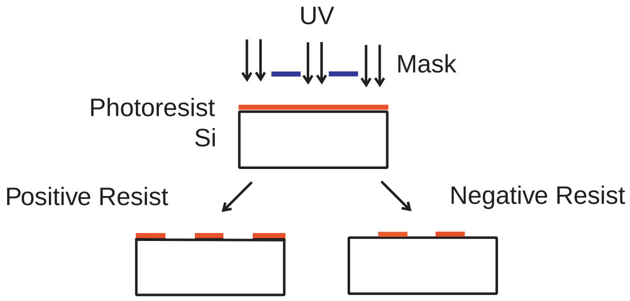

Figure 2.2: Effects of positive and negative resists

in the resist, and the resolution, which determines the minimum feature size which can be transferred onto the photoresist.

Resist application

The failure to remove debris and dust particles from the surface of the material before resist application will lead to degradation in the quality of pattern transfer. To remove such contaminants, samples are cleaned in an ultrasonic bath in the following solvents:

- Opticlear for 5 minutes
- Heated Acetone (40^oC) for 5 minutes
- Methanol for 5 minutes
- Iso propanol (IPA) for 5 minutes
- RO water for 5 minutes
- Dried using N_2

Fabrication of devices is performed in a "cleanroom", where the humidity, temperature and density of dust particles can be controlled. The cleanrooms in this work were class 10000 (10000 dust particles $> 0.5\mu m/$cubic foot), with class 100 work cabinets (100 dust particles $> 0.5\mu m/$cubic foot).

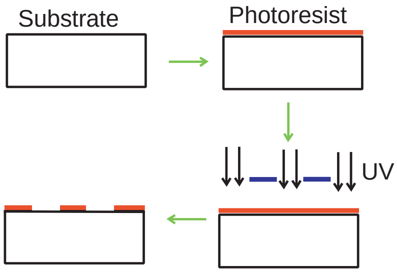

Figure 2.3: The fabrication steps for photolithography

The transfer of patterned resist onto a substrate is done in several stages (Fig 2.3). To apply the photoresist to the surface of the sample, the sample is placed on a vacuum chuck. This chuck is able to spin round at a speed that is determined by the user (measured in revolutions per minute). A HDMS (hexamethyldisilazane) based primer is applied to the surface of the sample and spun on. HMDS is used to improve photoresist adhesion to oxides. The HMDS reacts with the oxide surface in a process known as silylation, forming a strong bond to the surface. At the same time free bonds are left which readily react with the photoresist, enhancing the photoresist adhesion.

The photoresist is then applied to the wafer surface in small quantities using a filtered syringe, and is spun at a set speed and time to determine the thickness of the resist layer. For photoresists, the last two digits in the name give an indication of its thickness when spun at 4000 rpm for 30 s.

For example, the most commonly used resist, Shipley 1818, can achieve a thickness of 1.8 μm, whereas for AZ4562, its thickness is 6.2 μm. Although S1818 is the most commonly used photoresist, in this work it is not suitable for all processes. An example of this is its unsuitability for use as a mask for dry etching. In this case a more resilient photoresist such as AZ4562 should be used (This will be covered later on in chapter 7).

The sample is placed in an oven (90^oC) for 30 minutes to remove any remaining solvent in the resist. The sample is then exposed in the projection printer (or mask aligner) for a time determined by the photoresist type and feature sizes. It is then developed in a developer solution for a time and type determined by the resist type. (Examples of such times are given in table 2.1)

Resist Type	S1818	AZ4562
Spin Resist	4000 rpm for 6 s	1500 rpm for 60 s
Soft bake	30 min at 90^oC	30 min at 90^oC
Exposure	4.2 s	30 s
Development	1:1 H20:Microposit (2 mins)	4:1 H20: AZ400K developer (4 min)

Table 2.1: Application parameters for varying types of resists

A post bake is then done for 30 minutes for samples which use the photoresist as an etch mask. The perfect photoresist pattern should be one with sharp edges (90^o resist profiles) along the geometries of the required design. This situation is not always realised as photolithographic pattern transfer can be affected by diffraction, leading in some cases to incomplete exposure or the broadening of the features. Modifications to this standard process are shown in chapter 6 for the production of UV detectors from GaN.

2.2.2 E-Beam

Whereas the incident exposure source for photolithography is UV (em radiation), for e-beam it is electrons. Using Rayleigh's criterion [14]

$$W_{min} = k\frac{\lambda}{NA} \tag{2.1}$$

where W_{min} is the minimum feature size, λ is the wavelength of the source and k and NA are constants related to the resist and aperture, we see that the limit of the resolution is proportional to the wavelength.

As the wavelength of multi-keV electrons is much shorter than the wavelength of UV, the resolution is therefore improved, resulting in the ability to write smaller sized features ($\sim 10nm$). In addition, as no physical masks are used (instead the design is written in a pattern controlled by a CAD file), e-beam is a more flexible tool, as changing designs doesn't imply higher expenses and long delays. The main disadvantage of e-beam lithography is the speed of pattern writing, as the e-beam writes one pixel at a time (serially) whereas optical lithography writes all pixels instantaneously (parallel) and is consequently much quicker.

E-Beam Machine

The e-beam machine (or beamwriter) used was the Leica EBPG5 HR100 [15]. Fig 2.4 shows the main components of the beamwriter. The electrons are generated by an electron gun at the top. The electron gun is usually made of a material that can emit a suitable current density of electrons, such as a single crystal of lanthanum bromide (LaB_6) or a tungsten filament. The condenser lenses are used to focus the beam size to a set diameter, known as the spot size. The blanking plates are used to switch the beam on and off, while the final set of lenses is used to direct the beam of electrons within the scanning field to positions on the substrate below. The aperture controls the current density of the beam. The substrate is on a mechanical stage controlled by an interferometer, which can be moved so the scanning field can impinge on every part of the substrate.

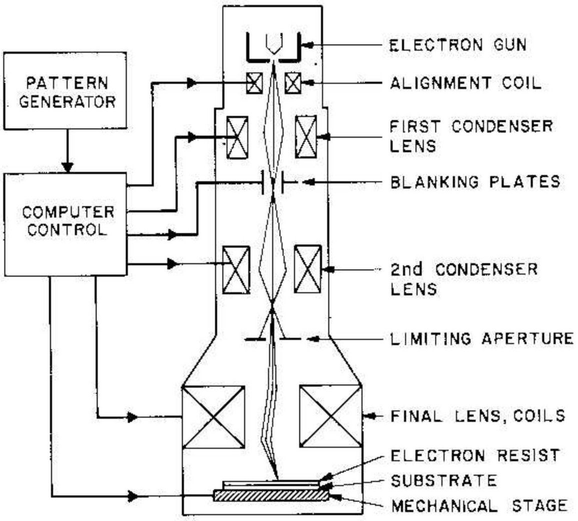

Figure 2.4: Schematic diagram of e-beam machine [13]

E-Beam Parameters

The patterns used in e-beam lithography are designed in a CAD package (Wavemaker or L-edit) and are stored as GDS file types. The GDS files are then transferred to a computer called CATS (Computer Aided Transcription System) where they can be changed into files readable by the program BELLE (Beamwriter Exposure Layout for Lithographic Engineers) (Fig 2.5). Once in BELLE, parameters of the pattern writing can be set and an indication of the job time is given. The parameters are shown in Table 2.2.

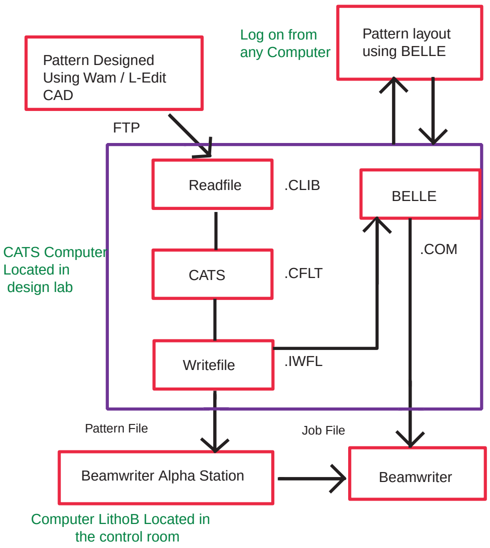

Figure 2.5: Computer and filetypes used for e-beam lithography

The writing time of a job can be calculated as

$$time = \frac{total\ charge}{beam\ current} = \frac{area \times dose(charge/area)}{beam\ current} \tag{2.2}$$

Also, the spot size increases linearly with the beam current. A spot size of 160nm has a beam current of 24 nA. This means a $1cm^2$ substrate requiring a dose of 300 μC$/cm^2$ would take

$$Job\,time = \frac{1 \times 300\mu C}{0.024\mu A} = 12500s = 3.47\ hrs \tag{2.3}$$

Larger spot sizes are therefore used for larger features to reduce write times. The smallest features that can be written are ~30 nm features using a 12 nm spot size with a beam energy of 100 kV. Registration (using suitable markers) can be done to 50 nm, a vast improvement on photo lithography, which is limited to ~5 μm.

Parameter	Consequence
Beam Energy (kV)	20, 50 or 100. Beam energy controls the minimum writable feature
Job Type	Simple - for a 1 layer pattern Registration - if job is to be written on a previous layer
Sample Size	Can range from 0.5 mm^2 to 5" mask plates (in special holders)
Spot Size (nm)	Measure of the physical size of the beam. Smaller spot sizes achieved when operating with small apertures and at 100 kV.
Dose	Measure of charge/area (how long the beam stays on one area). Value used is determined by the type of resist used
Resolution	Patterns are written in blocks of a size = 32000 resolution steps (nm)

Table 2.2: Parameters for e-beam jobs

A major problem associated with e-beam jobs is stitching errors. Stitching errors can occur when the block size (which is controlled by the resolution) is smaller than the pattern size and so the pattern is written in a matrix of block sized areas. Consequently, shapes that occur on block boundaries can be written incorrectly as a small error can occur in the alignment of adjacent blocks.

E-Beam Resist and Application

The most commonly used e-beam resist is PMMA (polymethyl methacrylate), which is a resist with a long carbon chain monomer. The incident electrons interact with the atoms of the resist, producing a high concentration of secondary electrons. These interactions cause the chemical bonds of the resist to be broken (chain scission) into smaller molecular fragments. These smaller fragments have a reduced molecular weight, resulting in the irradiated areas dissolving more quickly in the developing fluid MIBK (methyl isobutyl ketone). The fabrication techniques used for e-beam lithography are similar to those used for photo-lithography (Parameters are given in Table 2.3).

Step	Parameters
Spin Resist	Applied with pipette and spun at 5000 rpm for 60 s
Soft bake	30 min at 180^oC to remove solvent
Pattern Writing	Spot size, dose and energy dependent on resist type and size and density of features
Development	Sample developed in solution of 1:1 MIBK:IPA for 60 s at 23^oC

Table 2.3: Application parameters for e-beam resists

Chapter 6 will show in more detail the optimisation of e-beam parameters necessary for the fabrication of GaN detectors with interdigitated finger diodes with spacings <10 μm.

2.3 Lift-Off

For the application of metal contacts using the patterned resist, we use a technique known as lift-off. A thin layer of metal is deposited on the surface of the sample (on top of the patterned resist) using evaporation techniques. Such a deposition is highly directional so that no metal is deposited on the sidewalls of the developed resist. This causes a break in the metal layer continuity along the profile of the resist/surface interface. The sample is then placed in acetone where any remaining resist is subsequently dissolved. This leaves well-defined contact regions in the shape of the initial mask design (Fig 2.6).

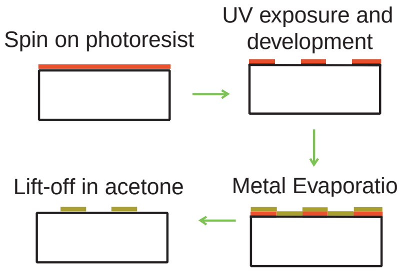

Figure 2.6: Process sequence for photolithographic lift-off

2.3.1 Surface Preparation

When fabricating Schottky contacts, the control of the metal-semiconductor interface is very important. Ideally, the interface should be defect and oxide free, and atomically smooth. Contacts formed on materials with superficial oxide layers will have electronic properties that vary from theoretical predictions. Principally, the size of the contact potential, which is theoretically determined by the difference of the metal's work function and the semiconductor's electron affinity, will instead be defined - and reduced - by the properties of any oxide layer present. This effect is known as Fermi pinning. To minimise the effects of surface states, samples can be cleaned in dilute hydrochloric acid (HCl), hydrofluoric acid (HF) or Aqua regia (3M HCl: 1M HNO_3) before the metal is applied to the surface.

2.3.2 Lift-off Enhancement

To reduce the chances of an imperfect lift-off - when some or all of the unwanted metal remains on the surface - processes can be optimised to encourage an overhang on the surface of the resist edges. Two such techniques are chlorobenzene soaks (photolithography) and bi-layers of resist (e-beam)

Chlorobenzene Soak

After the photoresist is spun on, the sample is baked in the 90^oC oven for 15 minutes. Once removed, it is placed in a solution of chlorobenzene for 15 minutes. This soaking process hardens the surface skin of the resist, reducing the dissolution of this top layer, causing a pronounced overhang in the resist (Fig 2.7). The sample is then baked for a further 15 minutes and developed for $1\frac{1}{2}$ times the usual developing time.

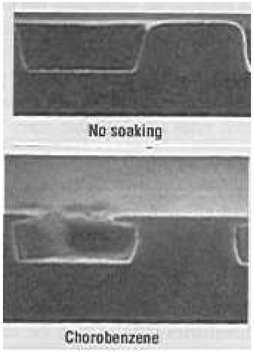

Figure 2.7: Effects of a chlorobenzene soak on the resist profile [14]

Bi-layer resists

Two layers of resist with varying molecular weights can be used to create an overhanging shape (Fig 2.8). A layer of high molecular weight resist is spun on top of a layer of low molecular weight resist. The higher molecular weight resist on top has fewer molecules in its resist layer.

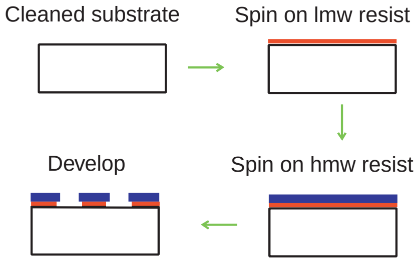

Figure 2.8: Effects of a bi-layer resist on the profile

2.4 Etching

In many cases, it is desirable to pattern defined shapes not only on the surface but also into the bulk of a material. The ability to create 3D structures such as channels and vias in a material can have applications ranging from pixel detectors with p-n junctions, where isolated pillars of p or n-type material may be fabricated, to microfluidic devices, where channels are made to permit the movement of precisely calibrated volumes of fluids in a silicon substrate.

The etching of a substrate can be performed using liquid chemicals (wet-etching) [16] or by using plasmas (dry etching), which remove areas of a substrate via chemical and/or physical (sputtering) interactions. For dry etching, the etch rate is less susceptible to change from small variations in the wafer temperature than for wet etching. The dry etches are also more anisotropic (Fig 2.9) and produce less chemical waste. For these reasons, dry etching was the principal technique used in this work.

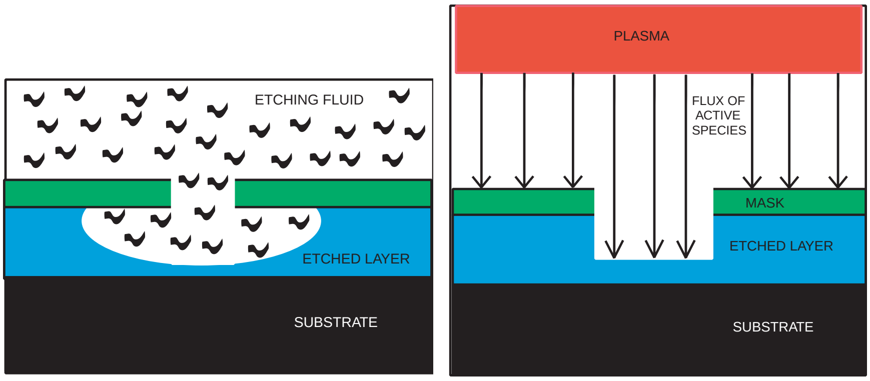

Figure 2.9: Examples of the etch effects of wet and dry etching techniques

2.4.1 Dry Etching

Dry etching involves the use of plasmas to remove unmasked portions of a substrate, leaving the mask and areas under the mask untouched. A plasma is defined as a partially ionized gas, where a small fraction of the gas contains dissociated atoms or molecular fragments called radicals, or ions in the form of charged atoms or molecules. It is these ion species that perform the removal of the etch layer either through sputtering or, along with the radicals, through chemical reactions. The processes which can occur in the most common method of plasma generation -DC glow discharge -, are shown in Table 2.4. Typically, radicals and charged species account for 1% and 0.01% of the total plasma, respectively [17].

Plasma Generation

A plasma can be generated when a DC bias is applied between two electrodes in the presence of a gas at low pressure (Fig 2.10). The conduction process is depends on the presence of ions. As the bias is increased, several different current-voltage regimes are seen (Fig 2.11) indicating different processes

Name	Reaction
Disassociation	$e^* + AB \rightleftharpoons A + B + e$
Atomic Ionisation	$e^* + A \rightleftharpoons A + +e + e$
Molecular Ionisation	$e^* + AB \rightleftharpoons AB^+ + e + e$
Atomic Excitation	$e^* + A \rightleftharpoons A^* + e$
Molecular Excitation	$e^* + AB \rightleftharpoons AB^* + e$

Table 2.4: Processes occurring in a glow discharge (* and + indicate energetic and charged atoms/molecules, respectively)

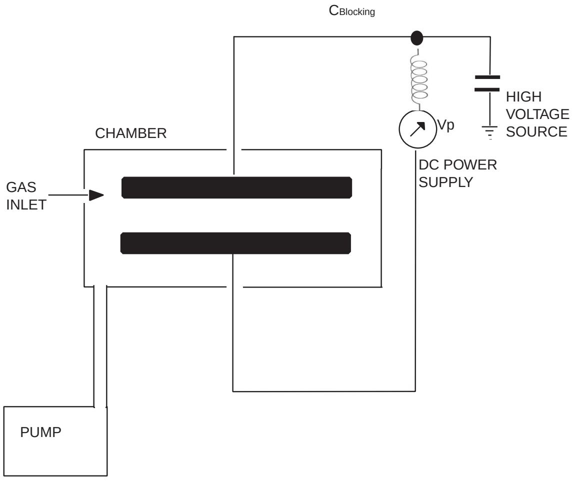

Figure 2.10: Schematic structure of a DC plasma

occurring between the electrodes and the gas.

Natural ionisation caused by cosmic rays and background radiation creates a minute current when a small electric field is created across the electrode. This region is known as the background ionisation. As the voltage is increased the current increases steadily until saturation occurs. At this point, the electric field cannot create any new ionisation in the gas.

Beyond this regime, (Townsend regime) production of secondary electrons occurs via collisions, along with the emission of secondary electrons from

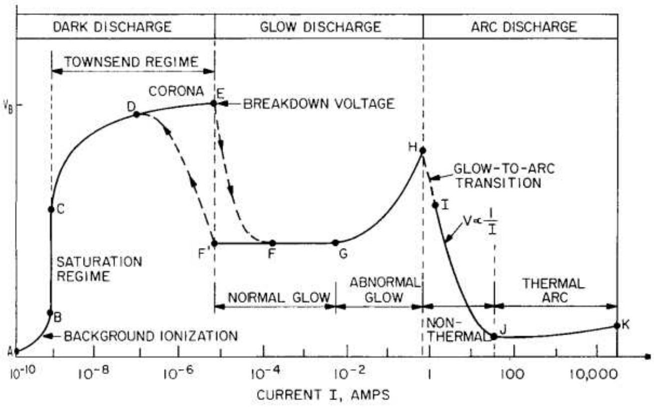

Figure 2.11: Varying current voltage regimes for DC discharging [17]

ions striking the cathode surface. These two processes lead to an exponential increase in the current levels, rising up until the breakdown voltage is reached. At this stage, electrons ($< 15eV$) begin to interact inelastically with the atoms in the gas, exciting core electrons to a higher energy state. After a short time, de-excitation occurs along with the emission of energy in the visible spectrum. This light emission is known as a glow discharge.

There are areas between the cathode and anode for which no light emission occurs. These are known as dark space regions, as illustrated in Fig 2.12. At the cathode, the electrons have too low an energy to create optical

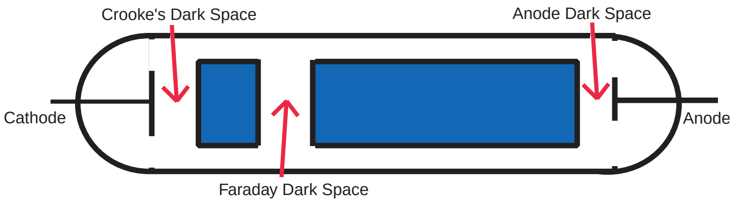

Figure 2.12: The dark space regions of a DC plasma

emission. This area is known as Crooke's dark space. The Faraday dark space occurs as the electrons have been accelerated away from the cathode, consequently too few electrons are left able to cause optical emission. Finally, as the anode acts as a sink for the electrons, there is too small a density of electrons in the vicinity of the anode to permit emission. This results in the Anode dark space.

Due to the Crooke's dark space, ions that drift and diffuse to the edge of this region are accelerated to the cathode. By placing substrates on the cathode, we can use ion bombardment to encourage sputtering and chemical reactions with the substrate surface. To prevent a charge build-up on the surface of the substrate, etching tools drive the plasma using an AC signal instead of a DC signal (Fig 2.13). The varying electric field is in the RF (radio frequency) range and is set at a standard frequency of 13.65MHz.

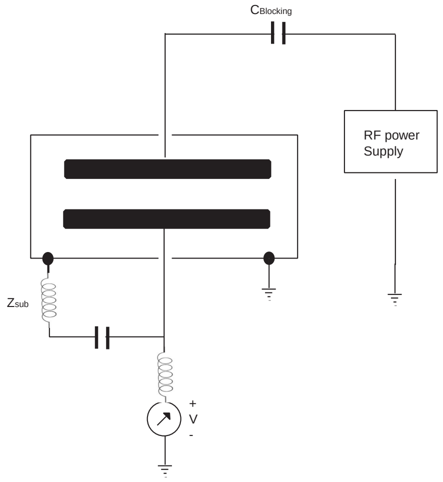

Figure 2.13: Schematic structure of a RF plasma

At low frequencies, the plasma and the width of the dark spaces pulsate in time with the applied signal. However, when the frequency is greater than 10kHz, the ions are too heavy and therefore too slow to be able to follow the changes in voltage. The electrons are mobile enough to oscillate between the electrodes, giving each a negative charge after striking the surface. This results in a dark space at each electrode, and a voltage drop between the plasma and each electrode. The potential drops for a parallel plate reactor are related by

$$\frac{V_1}{V_2} = \left(\frac{A_2}{A_1}\right)^q \tag{2.4}$$

where V is the the potential between the plate and the plasma, A is the area of the plate and the exponent q ranges from 1 to 2.5. The most common RF plasma reactor for applications such as RIE (reactive ion etching) uses such a parallel plate configuration, but with one larger electrode grounded. Using a smaller cathode increases the potential drop to the cathode.

Chemistry of a plasma etch

A range of gases can be used in RIE for etching of substrates. The gas used to etch silicon in this work was SF_6. The chemistry of the etching is highly complex and is not completely understood [18], but the general processes involved in the etch can be described as follows:

The formation of ion and radical species by electron impact dissociation is shown by

$$SF_6 + e^- => S_xF_y^+ + S_xF_y^* + F^* + e^- \tag{2.5}$$

$$O_2 + e^- => O^+ + O^* + e^- \tag{2.6}$$

The oxygen reacts with the surface of the silicon forming an oxide layer

$$O^* + Si(s) => Si(s) - n0 => SiO_n(sf) \tag{2.7}$$

where (s) and (sf) are surface and surface film respectively, and where $-$ indicates a chemical bond. This layer is removed by the plasma prior to the etching by the fluorine radical.

$$SiO_n(sf) + F^* => SiO_n(sf) - F \tag{2.8}$$

$$SiO_n(sf) - nF => Ion\ Energy => SiF_x(ads) + SiO_xF_y(ads) \tag{2.9}$$

The F is adsorbed onto the surface and removed by ion bombardment. Finally, the F is able to etch the Si through adsorption, followed by product formation then desorption as a gas

$$Si + F^* => Si - nF \tag{2.10}$$

$$Si - nF => Ion\ Energy => SiF_x(ads) \tag{2.11}$$

$$SiF_x(ads) => SiF_x(g) \tag{2.12}$$

Etch effects

Along with the chosen gas, varying parameters such as the process power, pressure and gas flow rates can alter the performance of a dry etch. The quality of the finished etched substrate is usually compared in the following categories [19]:

- Etch rate - The velocity at which the etched layer will be removed in the vertical direction below the mask
- Selectivity - The ratio of etched material to etched mask
- Uniformity - A measure of how uniform the flux of active species is on the surface of the wafer
- Directionality - The ability of the process to etch only the areas to be etched, and not the mask or areas under the mask

The effect of varying parameters on the etch quality will be shown in more detail in Chapter 7.

2.4.2 Inductively Coupled Plasma

A variation of the standard RIE is to increase the density of ion species by using a HDP - high density plasma - source. One such configuration is the Inductively Coupled Plasma (ICP) system (Fig 2.14), where the RF power is coupled to a plasma through an oscillating magnetic field (inductive coupling) instead of an oscillating electric field (capacitive coupling) [19].

The operating power levels of an ICP system are up to 2 kW instead of the few hundred Watts as is standard for capacitively coupled (CC) RF systems. This results in higher plasma densities of up to 10^{18} electrons m^{-3}. The ICP is operated at a pressure of 1-20 mTorr, far lower than that for CC systems. This is desirable for both etching and deposition applications, as the mean free path is increased and little scattering of ions or active species occurs before hitting the wafer. Higher densities also mean higher fluxes of ion and active species, which in turn increases etch rates.

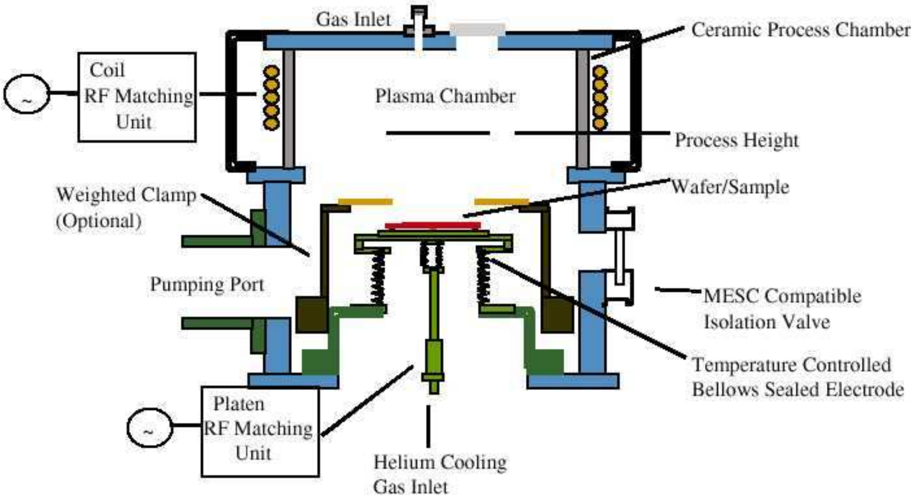

Figure 2.14: Schematic diagram of an inductively coupled plasma (ICP) machine [20]

ASE^{TM} **Process**

An ICP can be used for advanced silicon etching (ASE^{TM}) techniques [20, 21, 22, 12]. This process switches between periods of passivation and etching processes (C_4F_8 and SF_6 respectively). In the passivation step, a thin layer is deposited on the surface and sidewalls. In the following etch process, the passivation is removed from the bottom of the holes with the aid of ion energy. As the lateral etch rate is much slower than the vertical etch rate, high aspect ratios (around 13:1) and well-defined holes (with minimal etch damage) can be achieved.

$$CF_4 + e^- => CF_x^+ + CF_x^* + F^* + e^- \tag{2.13}$$

$$nCF_x^* => nCF_2(ads) => nCF_2(f) \tag{2.14}$$

$$nCF_2(f) + F^* => Ion\ Energy => CF_x(ads) => CF_x(g) \tag{2.15}$$

The use of the ASE^{TM} process for the production of Si devices is shown in chapter 7, as well as the use of parameter ramping - the variation of powers and pressures through the course of an etch - to enhance the upper aspect ratio of holes in Si.

Chapter 3

Detector theory

3.1 Introduction

To understand the use of GaN as both a UV and particle detector, a review of detector theory is presented in this chapter. The concepts of semiconductor crystal structure, carrier transport and metal-semiconductor contacts are outlined, with an emphasis placed on the theory of Schottky barriers. This type of operation of semiconductors is important when using wide band-gap materials, due to the extreme difficulty in fabricating p-n junctions in such materials. Also covered are the ways in which various types of ionising radiation create charge (signal) in detector material. In this chapter, images and information have been taken from the following books: "Physics of semiconductor devices" by Sze [23], "Metal Semiconductor Contacts" by Rhoderick [24] and "Radiation Detection and Measurement" by Knoll [25].

3.2 Solid State Theory

3.2.1 Crystal Structure

The constituent atoms of a semiconductor are arranged in a 3 dimensional periodic structure. This structure is referred to as a lattice, where a lattice is defined as being an infinite array of points in space arranged so that every lattice point has identical surroundings. For every semiconductor there is a unit cell which, when repeated, generates the lattice. Shown in Fig. 3.1 are three examples of such unit cells; the simple cubic, the body centred cubic, and the face centred cubic.

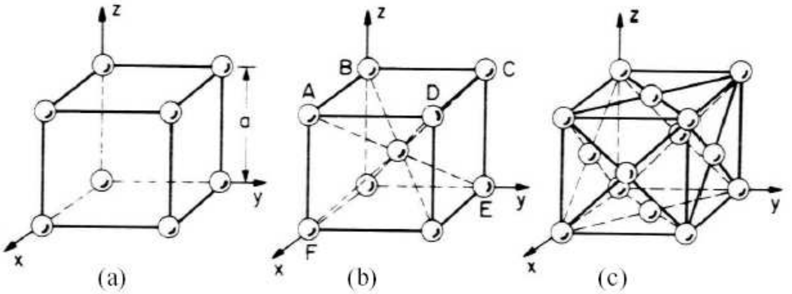

Figure 3.1: Examples of the (a) - simple cubic, (b) - body-centred cubic and (c) - face-centred cubic lattice structures [23]

A simple cubic lattice consists of an atom at the 8 corners of a cube each separated by a distance a, known as the lattice constant. For the body centred cubic, a similar structure is found, with the addition of an atom at the centre of the cube. Finally for the fcc, an atom is situated at the centre of each of the six faces of the cubic lattice, as well as one in each of the eight corners. These lattices have atoms with 6, 8 and 12 nearest neighbours respectively.

Semiconductors, such as Si, GaAs and GaN have more complex crystal structures (Fig 3.2). Silicon has a unit cell (with lattice constant $a =$ 0.543nm) which derives from the cubic-crystal family, with a diamond lattice structure. This can be visualised as two inter-penetrating fcc sub-lattices, with one sub-lattice displaced by $\frac{1}{4}$ of the distance along a diagonal of the cube. For silicon, each atom in the unit cell is of the same type. For many compound semiconductors the structure is identical, apart from each fcc sub-lattice constituting a different type of atom. This type of unit cell is called zinc blende. Wurtzite is the hexagonal close packing analogue of zinc-blende structures (which is cubic close packing) and is the most common structure for GaN (Fig 3.3). The lattice constants for wurtzite GaN are $a = 0.319$ nm and $c = 0.5165$ nm.

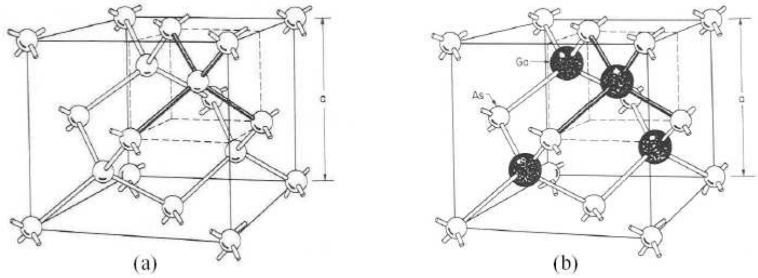

Figure 3.2: Examples of the (a) - diamond and (b) - zincblende lattice [23]

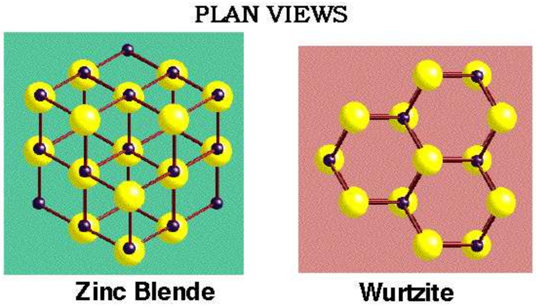

Figure 3.3: Examples of the planar views of (left) zinc-blende and (right) wurtzite structures [26]

Semiconductors can be classed into two types: elemental and compound. Elemental semiconductors are made of crystals deriving from one type of atom eg Si, Ge. Compound semiconductors are made up of more than one type of atom, such as GaN or InP. These compound semiconductors belong to the III-V group of semiconductors. This is because the first and second elements can be found in group III and group V of the periodic table respectively.

In compound semiconductors, the difference in electro-negativity leads to a combination of covalent and ionic bonding, whereas for elemental semiconductors the bonding is completely covalent. Ternary semiconductors are formed by the addition of a small quantity of a third element to the material, for example

$$Al_xGa_{1-x}N \tag{3.1}$$

The subscript x refers to the percentage of the element contained in the material.

3.2.2 Energy Bands

The electrons in an isolated atom are arranged into discrete energy levels. An example of this can be seen for the hydrogen atom, described by Bohr's model:

$$E_H = \frac{m_0 q^4}{8\varepsilon_0^2 h^2 n^2} = \frac{-13.6}{n^2}\ eV \tag{3.2}$$

where m_0 is the mass of an electron at rest, ε_0 is the permittivity of free space, h is Planck's constant and q is the electron charge. For the ground state (where the principle quantum number is n = 1) the electron will occupy the energy level, $E = -13.6eV$. This changes when two atoms of the same type are not far apart. In this case for each n value there is a doubly degenerate level, containing electrons with different spin states. This is due to Pauli's exclusion principle for fermions. As the atoms become closer, the energy levels for each n value will split into two.

When N atoms of the same type are brought together, the levels split into a seemingly continuous band of energies, consisting of N separate but extremely close levels. When the spacing decreases to the order of the lattice constant of the crystal, the energy band splits into two, forming a gap in the allowable energy of the electrons (Fig 3.4). This gap is known as the forbidden gap or bandgap. The band above is known as the conduction band, while the band below is known as the valence band. The width of the band gap determines if the material is a conductor, insulator or semiconductor.

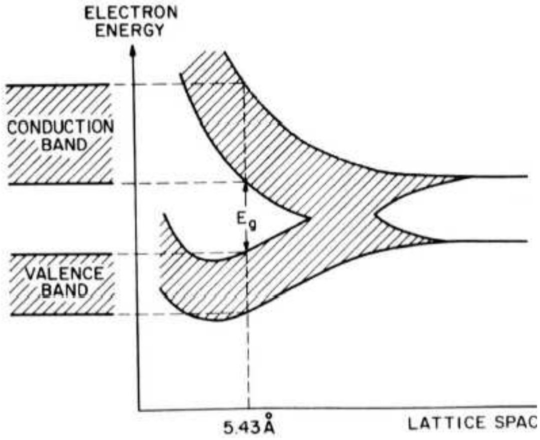

Figure 3.4: Energy bands for insulators, semiconductors and conductors [23]

In an insulator, the valence band is full and the conduction band is completely empty. The bandgap is so large that at room temperature, no applied electric field is able to raise electrons from the valence band to the conduction band. In a conductor, the conduction band is either partially filled, or the valence and conduction bands overlap, resulting in the absence of a bandgap. Electrons can then be raised from the valence band to the conduction band, gaining kinetic energy and hence able to conduct electricity.

For a semiconductor, thermal vibrations are enough to break the covalent bonds of the electrons to the atoms. When a break occurs, an electron is freed and a hole is created. A hole is analogous to an electron in every way apart from its positive charge. This means that holes can be influenced by an electric field, but will travel in the opposite direction to an electron.

3.2.3 Carrier Transport Phenomena

To use semiconducting materials as detectors, we must be able to collect electrons and holes created by the ionising effects of incident radiation. We can predict the movement of these carriers by studying how they are affected by large concentration gradients (diffusion) and by applied electric fields (drift).

Diffusion

The thermal energy of an electron can be derived from the theorem for equipartition of energy. The theorem states that a free particle will have $\frac{1}{2}kT$ units of energy per degree of freedom, where k denotes Boltzmann's constant and T the temperature. Therefore the kinetic energy of an electron moving in 3-D space is given by

$$\frac{1}{2}m_n v_{th}^2 = \frac{3}{2}kT \tag{3.3}$$

where m_n is the effective mass of electrons and v_{th} is the average thermal velocity. The electrons will be scattered by scattering centres such as lattice atoms, and consequently move in random directions, resulting in zero net displacement for each electron over a suitably long period. We denote the average time between collisions as the mean free time, τ_c. The mean free path (the average distance between collisions) can then be described as

$$l = v_{th}\tau_c \tag{3.4}$$

However, if there is a high concentration of carriers, then these carriers will tend to move from an area of high concentration to an area of low concentration, resulting in a diffusion current. For a simple model, we take a 1D semiconductor of length $x = 2l$, with $x = 0$ positioned at the midpoint. On average, half of the carriers to the left of the zero will pass through zero after one mean free time, and half of the carriers on the right of the zero will pass through zero within the same period of time. The net flux of carriers from left to right is then given by

$$F = \frac{1}{2}v_{th}\left[n(-l) - n(l)\right] \tag{3.5}$$

Taking the first two expressions from the Taylor series expression of this flux gives us [23]

$$F = -v_{th}l\frac{dn}{dx} \tag{3.6}$$

We define the diffusivity as

$$D = -v_{th}l \tag{3.7}$$

The diffusion current is therefore defined as

$$J_n = -qF = qD\frac{dn}{dx} \tag{3.8}$$

Drift

An electron in a semiconductor can be affected by an electric field, E, so that the electron begins to accelerate in a direction opposite to that of the electric field, experiencing a force, Eq. The velocity at which the electron moves when under the influence of an electric field is called the drift velocity,

v_d. The electron will retain this velocity until it eventually collides with something, such as a lattice atom or an impurity atom. The drift velocity can be calculated by equating the momentum gained by an electron ($m_n v_n$) with the momentum applied to the electron between collisions ($-qE\tau_c$). ie

$$m_n v_n = -Eq\tau_c \tag{3.9}$$

Equation 3.9 can be simplified to give

$$v_n = -\frac{q\tau_c}{m_n}E = -\mu_n E \tag{3.10}$$

giving

$$\mu_n = \frac{q\tau_c}{m_n} \tag{3.11}$$

where μ_n is the electron mobility. Using equation 3.7 and equation 3.11

$$D_n = \frac{kT}{q}\mu_n \tag{3.12}$$

Equation 3.12 is known as the Einstein Relation, and it relates mobility to diffusivity. μ_n is affected by temperature. Increasing the temperature can decrease the mobility, as the increase in lattice vibrations reduces the mean free time of the carriers. However, the mobility can also increase with temperature as impurity centres within a semiconductor have a reduced effect. Listed in Table 3.1 are values for μ_n for various semiconductors, along with other important electronic properties.

The saturation velocity v_s describes the maximum velocity with which an electron travels through a semiconductor. v_s is reached when the relationship between v_d and E is no longer linear, the drift velocity begins to plateau at sufficiently large fields due to enhanced phonon emission. If detectors made from semiconductors are operated at a high enough bias, the collection time for the carriers can be in the order of nanoseconds.

Property	Si	GaAs	4H-SiC	GaN
Bandgap E_g (eV)	1.12	1.42	3.25	3.4
Breakdown Field E_B $(MVcm^{-1})$	0.25	0.4	3.0	4.0
Electron Mobility μ $(cm^2V^{-1}s^{-1})$	1350	6000	800	1300
Hole Mobility μ $(cm^2V^{-1}s^{-1})$	450	400	120	30
Saturation Velocity v_s (10^7cms^{-1})	1.0	2.0	2.0	3.0
Diffusivity D_n $(Vscm^{-2})$	34.97	155.4	20.72	33.67

Table 3.1: Electronic properties for selected semiconductors

3.3 Metal Semiconductor Contacts

Electron-hole pairs created by ionising radiation have to be collected at electrodes, to be passed on to read-out electronics. These electrodes can be made using metals which form either Ohmic or Schottky contacts. The performance of these metal semiconductor junctions depends on parameters of both materials. The most important parameters are described below.

The work function of a metal, ϕ_m, is described as the amount of energy it takes to raise an electron from the Fermi level, E_F, to the vacuum level, or equivalently, to a state outside the surface of the metal. E_F is the energy level at which the probability of an electron residing at that energy is exactly $\frac{1}{2}$. This derives from the Fermi-Dirac distribution

$$F(E) = \frac{1}{1 + e^{\frac{E-E_F}{kT}}} \tag{3.13}$$

where $F(E)$ is the probability of occupation of an electron at an energy level E. The equivalent work function for a semiconductor is ϕ_s It is the energy taken to raise an electron from E_F to the vacuum level. Another important parameter for semiconductors is the electron affinity, χ_s, which is the difference in energy between an electron at the conduction band, E_c, and the vacuum level (qV_n is the energy taken to raise an electron from the Fermi level to the conduction band). These definitions give us

$$q\phi_m = q(\chi_s + V_n) \tag{3.14}$$

and can be seen in Fig 3.5.

3.3.1 Schottky Barriers

As stated earlier, one of the most common uses for metals on semiconductors are for Ohmic or Schottky contacts. An Ohmic contact is one with a very low resistance, allowing the potential difference across the contact to be proportional to the current flowing through it. If only ohmic contacts are used, then the leakage current is so large that it makes it impossible to extract the signal from the noise due to the leakage current. For this reason, rectifying contacts are used. These can be made using p-n junctions, or Schottky contacts. Due to the difficulty in creating p-type regions in n-type substrates, Schottky contacts are used for the creation of rectifying contacts on GaN.

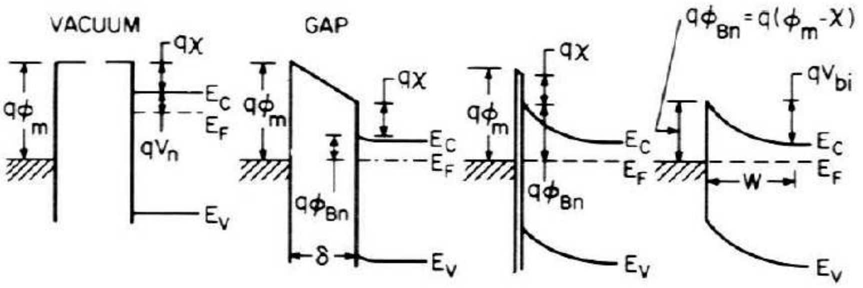

Figure 3.5: The formation of a Schottky Barrier [23]

The Schottky barrier is caused by a potential arising from the work functions of the materials. Fig 3.5 shows what happens to the energy levels when a metal is brought towards a semiconductor. At the far left, the materials are not in contact and therefore not in thermal equilibrium. When the materials are connected by a thin wire of length, δ, the Fermi levels for each material begin to adjust to be the same. In an n-type semiconductor where

$$\phi_m > \phi_s \tag{3.15}$$

realignment is caused by electrons flowing from the semiconductor to the metal. This causes a negative charge to be present at the metal surface, and a positive charge in the semiconductor. This positive charge arises from the uncompensated positive donor ions in a region depleted of electrons. As the concentration of donors is much less than the concentration of electrons, n, these positive donor ions occupy a layer of semiconductor. This is referred to as the depletion layer, and is of a thickness W. This layer causes E_c and E_v to bend. When δ starts to become infinitesimally small as shown at the far right of the diagram, an intimate Schottky contact is formed.

At this point, there exists at zero bias a built-in potential of qV_{bi}. The height of the Schottky barrier formed on an n-type semiconductor is given by

$$q\phi_{bn} = q(\phi_m - \chi_s) \tag{3.16}$$

For a p-type semiconductor, we have

$$q\phi_{bp} = E_g - q(\phi_m - \chi_s) \tag{3.17}$$

The bandgap of a semiconducting material is equal to the sum of the barrier heights on n-type and p-type substrates

$$q(\phi_{bp} + \phi_{bn}) = E_g \tag{3.18}$$

Equation 3.16 shows that choosing different metals with different values of ϕ_m leads to varying Schottky barrier heights. A range of ϕ_m and resultant Schottky barrier heights on GaN are shown in Table 3.2. The above argument assumes a simple single surface state. Non-intimate contacts result in barrier heights defined by surface states rather than the work function. The band structure of a metal-semiconductor contact can be altered by applying an

Metal	ϕ_m (eV)	ϕ_{bn} (eV)
Cs	2.14	-1.96
In	4.12	-0.02
Au	5.1	1
Pd	5.12	1.02
Ni	5.15	1.05

Table 3.2: Work function and resultant Schottky barrier heights on GaN ($\chi = 4.1eV$) for selected metals [24]

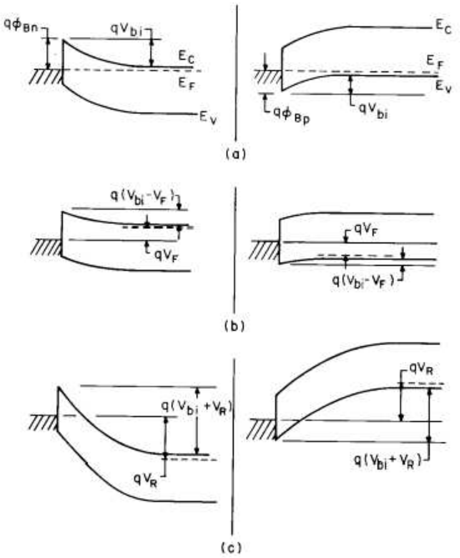

Figure 3.6: The effect of an applied bias on Schottky barriers on n and p-type material [13]

external bias. The effect of this is shown in Fig 3.6. The size of W, the depletion width can be expressed as

$$W = \sqrt{\frac{2\epsilon_S}{qN_D}(V_{bi} - V)} \tag{3.19}$$

where V is the applied external bias. This equation is based on the abrupt approximation (which is the case for a Schottky barrier), where $\rho = qN_D$ for $x < W$, and $\rho = 0$ and $\frac{dV}{dx} = 0$ for $x > W$. The resulting capacitance per unit area of the depletion region is given by

$$C = \sqrt{\frac{q\epsilon_s N_D}{2(V_{bi} - V)}} = \frac{\epsilon_S}{W} \tag{3.20}$$

Plotting a graph of $1/C^2$ vs V, we can extract N_D from the gradient of the line and V_{bi} as the intercept on the x-axis (assuming N_D is constant throughout the depletion region).

3.3.2 Schottky Effect

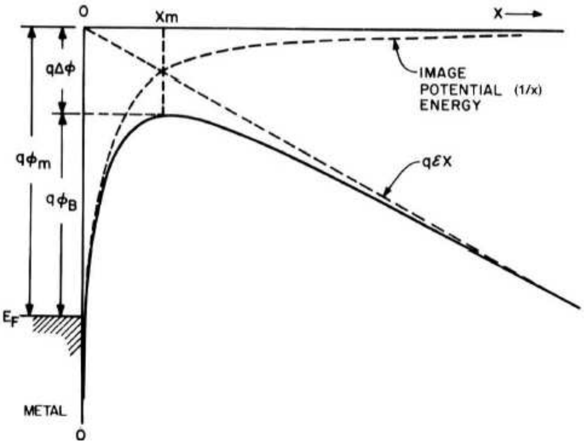

Figure 3.7: The energy band diagram for a metal-vacuum interface [23]

The Schottky effect describes the the image force between the electron and the surface of the metal. Considering the metal-vacuum case, the minimum energy needed to remove an electron from the surface of a metal is the work function, ϕ_m (Fig 3.7). When an electron (with a charge $-q$) is a distance x away from the metal surface, we can describe this as being equivalent to a positive charge, q, located at $-x$, with respect to the metal (Fig 3.8). The attractive force between each charge and the metal surface is the same, and for the positive charge q, the attractive (or image) force felt is given by

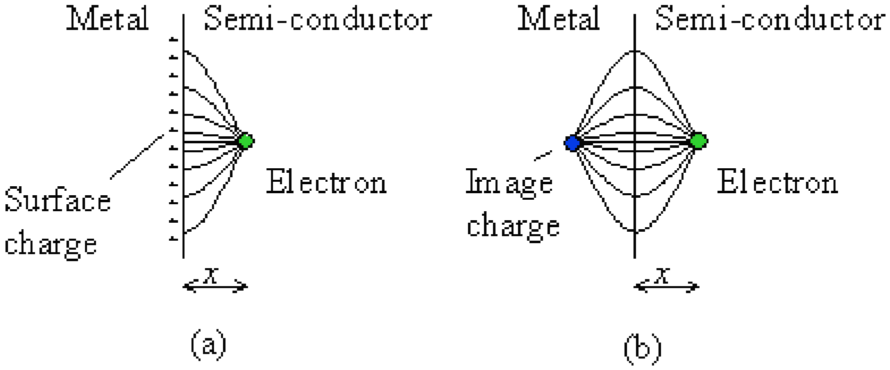

Figure 3.8: (a) - Field lines and surface charges due to an electron in close proximity to a perfect conductor and (b) - the field lines and image charge of an electron [27]

$$F = \frac{q^2}{4\pi\varepsilon_o(2x)^2} = \frac{q^2}{16\pi\varepsilon_o x^2} \tag{3.21}$$

This force gives the charge an energy

$$E_P = \int_{\infty}^{x} F(x)dx = \frac{q^2}{16\pi\varepsilon_o x} \tag{3.22}$$

With an applied external field, ξ, the total potential energy is then given by

$$E_{P_T}(x) = \frac{q^2}{16\pi\varepsilon_o x} + q\xi x \tag{3.23}$$

The maximum lowering x_m, is given when $dE_{P_T}/dx = 0$, so eqn (3.23) simplifies to

$$\frac{q^2}{16\pi\varepsilon_0 {x^2}_m} = \xi q \tag{3.24}$$

For the semiconductor/vacuum system, we replace ε_o with ε_s, the permittivity of the semiconductor, giving

$$x_m = \sqrt{\frac{q}{16\pi\varepsilon_s\xi}} \tag{3.25}$$

The effect of this image force is that the barrier that an electron has to surmount from a metal to a semiconductor is lowered by an amount, $\Delta\phi$, which is given by

$$\Delta\phi = \sqrt{\frac{q\xi}{4\pi\varepsilon_0}} = 2\xi x_m \tag{3.26}$$

The location and magnitude of the reduced barrier height can be seen in Fig 3.9.

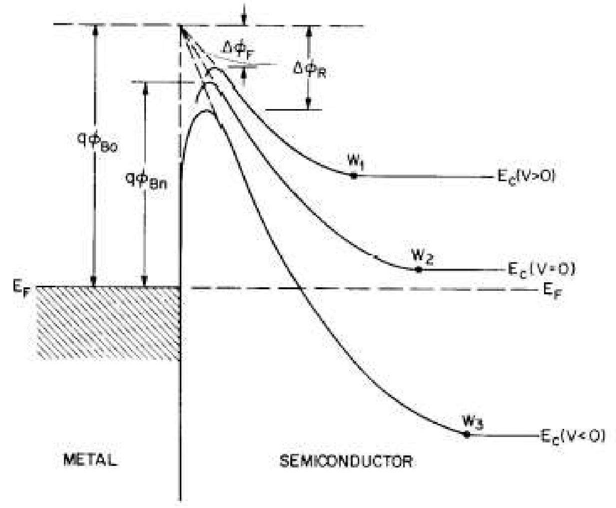

Figure 3.9: The energy band diagram for a metal-vacuum interface with the Schottky effect for n-type semiconductors [23]

3.3.3 Current Transport Processes

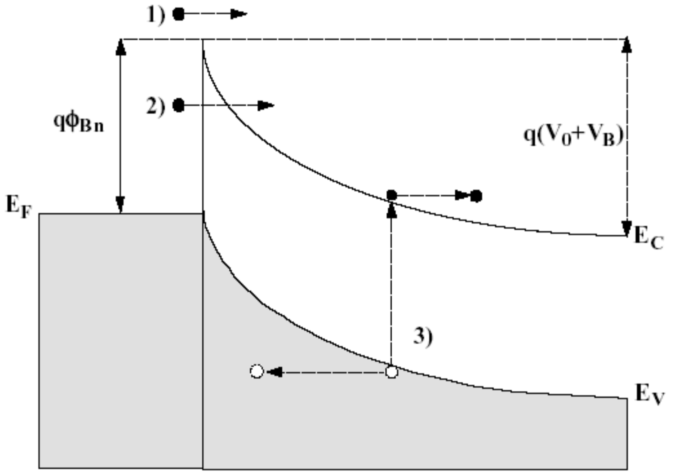

Figure 3.10: Schematic diagram indicating the main current transport processes in a semiconductor [13]

The current across a metal-semiconductor junction is mainly due to majority carriers. Three distinctly different mechanisms exist (Fig 3.10):

1. The transport of electrons over the potential barrier into the metal. This is done either by diffusion of carriers from the semiconductor into the metal, or thermionic emission of carriers across the Schottky barrier
2. Quantum-mechanical tunnelling through the barrier, where the wave-nature of the electrons is taken into account, allowing them to penetrate through thin barriers.
3. Recombination of charges in the space charge region

For a given junction, a combination of all three mechanisms could exist. However, typically one finds that only one limits the current, making it the dominant current mechanism. For Schottky diodes operated at room temperature, the dominant mechanisms are thermionic emission and diffusion. Current voltage characteristics for Schottky diodes can be estimated by combining thermionic emission theory and diffusion theory. The diffusion of carriers is controlled by the region through which they diffuse. This can be seen in Fig 3.9 where the electron potential energy is plotted against distance, taking into account the Schottky effect for a metal semiconductor barrier. The smoothing of the top of the curve is due to the electric field caused by the ionised carriers and the potential of the electrons as they near the metal surface.

The complete expression for current transport described by the thermionic-diffusion theory is [23]

$$J = J_S \left(\exp \frac{qV}{kT} - 1 \right) \tag{3.27}$$

where

$$J_S = A^{**} T^2 \exp \left(\frac{-q\phi_{Bn}}{kT} \right) \tag{3.28}$$

J is the current density (Acm^{-2}), J_S is the saturation current density and A^{**} is the effective Richardson's constant. From this relationship, we can calculate the barrier height from current-voltage measurements using

$$\phi_{Bn} = \frac{kT}{q} \ln \frac{J_s}{A^{**} T^2} \tag{3.29}$$

3.4 Radiation Detection

The basic principle of operation for semiconducting radiation detectors is that incident radiation loses energy as it passes through the detector. The number of electron-hole pairs that are created in the detector is proportional to the energy deposited in the detector. Using Ramo's Theorem [28], charge is then induced at the electrodes from the movement of these created carriers under an applied electric field, with the induced charge being proportional to the distance the carriers travel normalised to the detector thickness.

However, the way in which energy loss occurs is strongly dependent on the type and energy of the incident radiation. The following section describes how heavy charged particles, fast electrons, neutrons and photons lose their energy.

3.4.1 Heavy Charged Particles

For heavy charged particles such as alpha particles, energy loss occurs through Coulomb interactions with the orbital electrons in the absorber material and the charge of the incident particles (for radiation detectors we ignore alternative nuclear interaction events such as Rutherford scattering). On entering the absorber material, the charged particle interacts simultaneously with many electrons, either by excitation (raising an electron to a higher shell within the absorber atom), or ionisation (completely removing an electron from the absorber atom). Each time an interaction occurs, the charged particle loses energy, and consequently loses velocity. This process continues until the particle is stopped.

The specific energy loss of a charged particle, S, is defined as

$$S = -\frac{dE}{dx} \tag{3.30}$$

This is also referred to as the limiting stopping power. For fast particles, the Bethe-Bloch formula [25] gives the energy loss for a known charge state and velocity as

$$-\frac{dE}{dx} = \frac{4\pi e^4 z^2}{m_0 v^2} NB \tag{3.31}$$

where

$$B = Z\left[\ln\frac{2m_0v^2}{I} - \ln(1-\frac{v^2}{c^2}) - \frac{v^2}{c^2}\right] \tag{3.32}$$

v and ze are the velocity and charge of the incident particle, N and Z are the number density and atomic number of the absorber atoms, m_0 is the electron rest mass and e is the electronic charge. I is an experimentally determined parameter accounting for the average excitation and ionisation potential of the absorber. Only the first term in equation 3.31 is significant for non-relativistic particles.

From equation 3.31 we note that energy loss for fast particles is proportional to $1/v^2$. The slower an incident particle is, the greater time it spends near electrons in the absorber, and consequently the Coulomb and therefore energy transfer is large. We can also see from equation 3.31 that energy loss is also proportional to z^2. This means the more charge an incident particle has, the greater the energy loss.

The specific energy loss of charged particles can be plotted against the distance the particle penetrates into the absorber. This is known as a Bragg curve. The Bragg curve for a 5.48 MeV α particle in GaN is shown in Fig 3.11. The range of such a particle in GaN was calculated using the SRIM package [29]

3.4.2 Fast Electrons

For fast electrons, energy loss in an absorber occurs at a slower rate relative to heavy charged particles. In addition, as electrons are of the same size as the electrons in the absorber, large deviations can occur in collisions. Electron nuclear interactions can also occur, also significantly changing the particle's path. These effects result in a modified version of the Bethe-Bloch equation

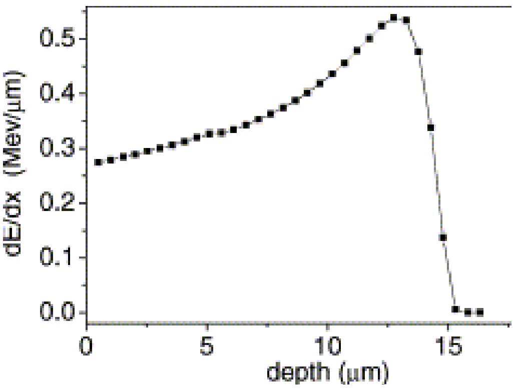

Figure 3.11: The specific energy loss of a 5.48MeV α particle in GaN

[25]

$$-\left(\frac{dE}{dx}\right)_c = \frac{2\pi e^4 NZ}{m_0 v^2} A \tag{3.33}$$

where

$$A = \left[\ln \frac{m_0 v^2 E}{2I^2(1-\beta^2)} - (\ln 2)\left(2\sqrt{1-\beta^2} - 1 + \beta^2\right) + (1-\beta^2) + \frac{1}{8}\left(1-\sqrt{1-\beta^2}\right)^2\right] \tag{3.34}$$

and $\beta = v/c$.

As well as these collisional interactions, energy loss can occur through radiative processes such as bremsstrahlung, in which X-rays are released when the electron decelerates suddenly. The specific energy loss due to radiative processes is given by [25]

$$-\left(\frac{dE}{dx}\right)_r = \frac{NEZ(Z+1)e^4}{137 m_0 c^4}\left(4ln\frac{2E}{m_0 c^2} - \frac{4}{3}\right) \tag{3.35}$$

The total linear stopping power for electrons is therefore

$$\left(\frac{dE}{dx}\right) = \left(\frac{dE}{dx}\right)_c + \left(\frac{dE}{dx}\right)_r \tag{3.36}$$

with the ratio of specific energy losses given as

$$\frac{(dE/dx)_r}{(dE/dx)_c} \sim \frac{EZ}{700} \tag{3.37}$$

Radiative processes tend to dominate when the energy of the electron is greater than $\sim 10MeV$.

3.4.3 Neutrons

As with photons, neutrons carry no charge and therefore do not undergo Coulomb interactions with the absorber material. Consequently, incident neutrons can often travel through centimeters of material without interacting. On interaction, a neutron is either altered in energy and direction, or disappears and is replaced with the product of secondary reactions. However, unlike photons, these interactions often create heavily charged particles.

Neutron interactions are either fast (high energy) or slow (low energy) neutron interactions. Slow neutron interactions include elastic scattering between absorber nuclei, in which relatively little energy is transferred in the collisions, and inelastic nuclear reactions. The former type of reaction is then not useful for detecting slow neutrons as little ionisation takes place. The high probability of elastic scattering, however, acts to reduce the incident neutrons to thermal equilibrium with the absorber.

The most efficient way to detect such neutrons is from the products of secondary reactions from neutron-induced nuclear reactions. The (n,p), (n,fission) and (n,α) reactions produce secondary radiations in the form of charged particles which can be detected. The (n, γ) interaction can also occur, but is hard to measure due to the difficulty in detecting the γ emission.

For fast neutrons, detection becomes harder with increasing energy levels. However, the energy transferred on scattering is increased, creating the secondary products known as recoil nuclei, which receive energy from the neutron collisions. If the energy of the neutron is high enough, inelastic scattering can occur, causing the recoil nuclei to be raised to a higher excited energy state. After a short time, the recoil nucleus de-excites, and γ rays are released. The nucleus loses a greater fraction of energy in this process than it would from an elastic collision and, consequently, such a reaction can complicate the detection of fast neutrons.

Each energy value of neutrons has a corresponding collision probability or cross-section, σ, associated with it. For N nuclei per unit volume, the macroscopic cross-section Σ is

$$\Sigma = N\sigma \tag{3.38}$$

and the reaction rate density (RRD) as

$$RRD = \phi(r,E)\Sigma(E)dE \tag{3.39}$$

where $\phi(r)$ is the neutron flux.

3.4.4 X-rays/ γ-rays

There are three main processes by which a photon can interact with an absorber: photoelectric absorption, Compton scattering or pair production. All three processes allow energy transfer from the photon to the absorbing material. The two main characteristics of photon interactions with an absorbing material are that

- Due to their smaller interaction cross-section, photons penetrate much further into a material than charged particles do
- A photon beam passing through a material undergoes a reduction in intensity, but not in energy

This second characteristic arises because a photon is either removed from the beam by absorption (photoelectric effect or pair production), scattering (Compton), or it undergoes no interactions and passes straight through the material. Those that do pass straight through the material retain their original energy. The attenuation that occurs for a beam of photons passing through a material is described by

$$I(x) = I_0 \exp(-\mu x) \tag{3.40}$$

where I_0 is the initial beam intensity, x is the thickness of the absorber and μ is the absorption coefficient, which depends on the absorbing material and is related to the total cross-section.

Photoelectric Effect

For the photoelectric effect, an incident photon disappears completely on interaction with an absorber atom. A photoelectron is freed from a bound state in the absorber atom. The photoelectron will have an energy given by

$$E = h\nu - E_b \tag{3.41}$$

where E_b is the energy of the electron in its bound state. The photoelectric effect is the dominant interaction process for low energy γ-rays and X-rays. The probability of photoelectric interaction also increases with the atomic number, Z, of the absorber material as shown by

$$\tau \sim const. \times \frac{Z^n}{E_\gamma^{3.5}} \tag{3.42}$$

where $4 < n < 5$, depending on the photon energy.

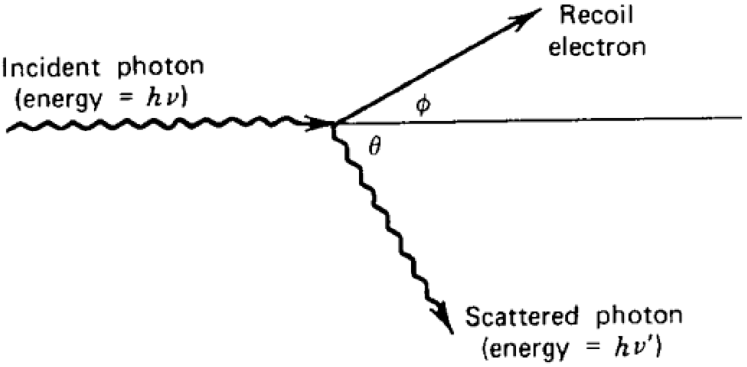

Figure 3.12: Compton scattering of a photon incident on a "free" electron [13]

Compton Effect

Compton scattering (Fig 3.12) occurs between an incident photon and an electron from an absorber atom. On interaction, the photon is scattered at an angle θ relative to its original direction. The electron which is struck by the photon (known as the recoil electron) gains energy from the collision and it too is scattered at an angle ϕ. Solving simultaneous equations for the conservation of energy and momentum, the energy transfer and scattering angle are related through

$$h\nu' = \frac{h\nu}{1 + \frac{h\nu}{m_0c^2}(1 - cos\theta)} \tag{3.43}$$

where m_0c^2 is the rest mass energy of an electron (0.511 MeV). The probability of Compton scattering increases linearly with Z.

Pair Production

If an incident photon has an energy of at least $2m_0c^2$ (1.022 MeV), it can be transformed into an electron-positron pair. The produced positron eventually slows down and annihilates, generating two back-to-back photons. As pair production dominates only at very high energies, the probability of occurrence is very low. The relative importance of these three processes for a range of photon energies can be seen in Fig 3.13.

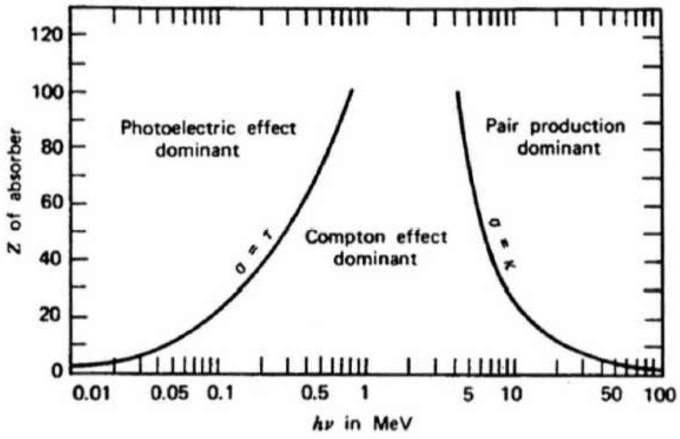

Figure 3.13: The relative importance of the photoelectric effect, Compton scattering and pair production over a range of energies [30]

The following chapters will now show the experimental results for the interaction of protons and neutrons (Chapters 4 & 7) and γ-rays and X-rays (Chapters 4 & 6) with fabricated GaN and 3D Si detectors.

Chapter 4

GaN as a radiation hard detector

4.1 Introduction

As stated previously, GaN is a solar blind material (E_g=3.42 eV), and consequently it has a higher signal-to-noise ratio for UV than, for example, silicon. This has led to its use in developments in technologies such as lasers and high-brightness light emitting diodes in the blue and UV wavelengths. However, due to its high density (6.15 gcm^{-3}) and high threshold voltage, GaN is now being recognised as a possible material on which to fabricate ionising radiation detectors. This avenue of research is encouraged by the desire to investigate viable alternatives to silicon as a radiation hard material, as detailed by the requirements of an upgraded Large Hadron Collider at CERN [31]. For such an accelerator, detecting materials must be able to operate after receiving an estimated 10 year fluence of up to 1×10^{16} hadrons/cm^2. This work will detail the first results taken on the variation of leakage current and degradation of charge collection efficiency of GaN Schottky pad diodes after irradiation with fluences of protons, neutrons and X-rays.

4.2 Radiation Hard Materials

4.2.1 Radiation Damage

Radiation damage describes the detrimental consequences of exposure to radiation. The severity of the damage depends on such parameters as the type of incident particle (charged or neutral) and its energy (Details for 1 MeV particles are given in Table 4.1). Generally, heavier particles are slower, stopped easily and deposit almost all their energy in a short distance. For the same energy for electrons (1 MeV), the particle is already relativistic.

Characteristic (Radiation E=1MeV)	Alpha (α)	Proton (p)	Beta (β) or Electron (e)	Photon (γ or X-ray)	Neutron (n)
Symbol	${}^4_2\alpha$ or He^{2+}	${}^1_1p$ or H^{1+}	${}^{0}_{-1}e$ or β	${}^0_0\gamma$	${}^1_0n$
Charge	+2	+1	-1	neutral	neutral
Ionisation	Direct	Direct	Direct	Indirect	Indirect
Mass (amu)	4.00277	1.007276	0.000548	-	1.008665
Velocity (cm/sec)	6.944×10^8	1.38×10^9	2.82×10^{10}	2.998×10^{10}	1.33×10^9
β	2.3%	4.6%	94.1%	100%	4.6%
Range in air (cm)	0.56	1.81	319	82,000*	39,250*

Table 4.1: Comparison of ionising radiation (* range based on a 99.9% reduction)

There are 3 main macroscopic effects associated with the energetic hadron irradiation of high-resistivity silicon diodes [32]:

1. n-type material undergoes type inversion and becomes effectively p-type under bias. Further irradiation changes the effective doping concentration, N_{eff}, consequently increasing the depletion voltage.
2. An increase in leakage current occurs proportional to the irradiation fluence, caused by the creation of recombination/generation centres. This

increase in leakage current results in increased noise and contributes to a higher power consumption.

3. A decrease in charge collection efficiency is noted, caused by charge carrier trapping.

4.2.2 Requirements of a Radiation Hard Detector

The tracking of ionising particles requires high spatial resolution, short signal duration and good energy resolution. In addition to measuring accurately the momenta of charged particles from the bending of their trajectories in a magnetic field, there must exist a capability of distinguishing secondary from primary interaction vertices. These requirements form the basis of the design features of all experiments at high luminosity colliders, such as the LHC.

The Large Hadron Collider (LHC) at the European Laboratory for Particle Physics (CERN) is due for completion in 2007. The LHC will be used to test the validity of the Standard Model of elementary particle interactions and for the possible discovery of new physics. The LHC will provide proton-proton interactions at a centre of mass energy of 14 Tev and will be operated at a nominal luminosity of 10^{34} $cm^{-2}s^{-1}$ for around 10 years, with a predicted fluence of fast hadrons, at the tracking elements closest to the beam, equivalent to 10^{15} cm^{-2} 1 MeV neutrons. The proposed upgrade of the LHC, sLHC, would see the luminosity rise to 10^{35} $cm^{-2}s^{-1}$, increasing the expected total fluence of fast hadrons to above 10^{16} cm^{-2}.

Current silicon detectors would be unable to operate at the required LHC fluence, due to macroscopic effects. Therefore, through the RD50 [10] collaboration, 3 main areas are being investigated for the development of radiation hard detectors.

- Material Engineering - Includes work on the defect engineering of silicon (enrichment with oxygen, oxygen dimers) and the possible use of alternative materials (SiC, GaN)
- Device Engineering - Improvements on standard planar detector designs (3D detectors, thinning of bulk material)
- Variation of detector operational conditions - Investigation into possible improvements in performance through operation at lower temperatures or with forward bias

In this work, semi insulating GaN was irradiated with fluences of protons, neutron and X-rays. Diodes were measured for any deterioration in charge collection efficiencies and for increases in leakage currents

4.3 Parameters for GaN as a Radiation-Hard Material

The work in this chapter details the first examination of GaN as a radiation hard detector. For this reason, details are included of some standard parameters associated with particle detection, the full derivation of which have have not yet been shown.

4.3.1 Radiation Length

The radiation length, χ, is defined as being the length of absorber in which a particle will lose all but 1/e of its energy to bremsstrahlung. An approximation (to within 2.5%) formulated by Dahl [33] can be used to calculate χ

as

$$\chi = \frac{716.4 \times (A/\delta)}{Z(Z+1)\ln(287/\sqrt{Z})} \tag{4.1}$$

where Z and A are the nuclear charge and atomic weight of the material respectively, and δ is the density of the material. For a compound semiconductor, the radiation length is approximated as

$$\frac{1}{\chi} = \sum \frac{w_j}{\chi_j} \tag{4.2}$$

where w_j and χ_j are the fraction by weight and radiation length for the j th element. Using eqn (4.2)

$$\chi_{Ga} = \frac{716.4 \times (69.7/5.9)}{31(31+1)\ln(287/\sqrt{31})} cm = 2.16\ cm \tag{4.3}$$

Similarly we find

$$\chi_N = 30.56\ cm \tag{4.4}$$

The fraction by weight for Ga and N in GaN are calculated as follows

$$w_{Ga} = \frac{A_{Ga}}{A_{Ga} + A_N} = \frac{69.7}{69.7 + 14} = \frac{69.7}{83.7} = 0.833 \tag{4.5}$$

Similarly

$$w_N = \frac{14}{69.7 + 14} = \frac{14}{83.7} = 0.167 \tag{4.6}$$

Therefore, the radiation length for GaN can be calculated as

$$\frac{1}{\chi_{GaN}} = \frac{w_{Ga}}{\chi_{Ga}} + \frac{w_N}{\chi_N} = \frac{0.833}{2.16} + \frac{0.167}{30.56} = 0.386\ cm^{-1} \tag{4.7}$$

giving

$$\chi_{GaN} = 2.56\ cm \tag{4.8}$$

The equivalent numbers for various semiconducting materials are given in Table 4.2.

Property	Diamond	4H-SiC	Si	GaN
E_g (eV)	5.5	3.27	1.12	3.39
μ_e (cm^2Vs^{-1})	1800	800	1500	1000
μ_h (cm^2Vs^{-1})	1200	115	450	30
e-h energy (eV)	13	8.4	3.6	8-10
Displacement (eV)	43	25	13-20	10-20
Density (gcm^{-3})	3.52	3.21	2.33	6.15
Radiation Length χ_0 (cm)	12.2	8.7	9.4	2.56
e-h pairs/χ_0 $(10^6 cm^{-1})$	4.4	4.5	10.1	2-3

Table 4.2: Properties of diamond, 4H-SiC, Si and GaN crystals

4.3.2 Threshold Energy

Bulk damage in a material is primarily caused by an incoming particle displacing a primary knock-on atom (PKA) from its lattice site, creating an interstitial and a vacancy. This pair of defects is known as a Frenkel pair. To calculate the energy required to create a Frenkel pair, it is necessary to know the displacement threshold energy, T_d of the absorbing material. The threshold energy of gallium, T_d^{Ga}, is known to be 45eV [34] but is unknown for nitrogen. Due to the close proximity of Zn and Ga, and N and O in the periodic table, an analogy between GaN and ZnO (where T_d^{Zn}=50 eV and T_d^{O}=55 eV [35]), then suggests that T_d^{N} can be approximated as $\sim$ 30-50 eV.

For elastic scattering in which a particle with mass m_p and energy E_p collides with an atom with a mass m_{atom}, the maximum energy that can be imparted to a recoil particle E_R^{MAX} can be calculated using the relationship [32]

$$E_R^{MAX} = 4E_P \frac{m_p \times m_{atom}}{(m_p + m_{atom})^2} \tag{4.9}$$

We can then calculate the energy a neutron needs to create a Frenkel pair in

Ga as

$$E_P = \frac{E_R^{MAX}}{4}\frac{(m_p + m_{Ga})^2}{m_p * m_{Ga}} = \frac{43eV}{4}\frac{(940 + 65509)^2}{940 * 65509} \sim 800\ eV \tag{4.10}$$

Similarly, for $T_d^N \sim$ 30-50 eV, we find

$$E_P \sim 120 - 200\ eV \tag{4.11}$$

The energy a neutron needs to create a Frenkel pair from Ga-Ga in GaN is then

$$E_P^{Ga} = \frac{E_R^{MAX}}{4}\frac{(m_p + m_{GaN})^2}{m_p \times m_{GaN}} = \frac{43eV}{4}\frac{(940 + 55892)^2}{940 \times 55892} \sim 660\ eV \tag{4.12}$$

For the creation of a Frenkel Pair from N-N in GaN is

$$E_P \sim 460 - 770\ eV \tag{4.13}$$

4.3.3 NIEL Hypothesis

The NIEL hypothesis [36] (Fig 4.1) allows comparison to be made between displacement damage caused by fluences of varying hadronic interactions (p, π, e, n). Using an hadronic fluence, Φ_h, producing damage equivalent to a fluence, Φ_{eq}, of 1MeV neutrons, the hardness factor κ of a material can be found using

$$\kappa = \frac{\Phi_{eq}}{\Phi_h} \tag{4.14}$$

For each interaction leading to displacement damage a primary knock-on atom with recoil energy E_R is produced. The proportion of recoil energy given to displacement damage depends on the recoil energy itself and is calculated using the Lindhard Partition Function, $P(E_R)$ [37]. Using the Lindhard partition function, the NIEL is calculated as the displacement damage cross-section, given by

$$D(E) = \sum_{\upsilon} \sigma_{\upsilon}(E) \int_0^{E_R^{Max}} f_{\upsilon}(E, E_R) P(E_R) dE_R \tag{4.15}$$

υ denotes every possible interaction of an incoming particle with energy E leading to a displacement within the lattice. σ_{υ} is the corresponding cross-section for interaction υ to occur. $f_{\upsilon}(E, E_R)$ is the probability that an incoming particle of energy E will produce a PKA with recoil energy E_R in the reaction υ. The integration is over all possible recoil energies E_R.

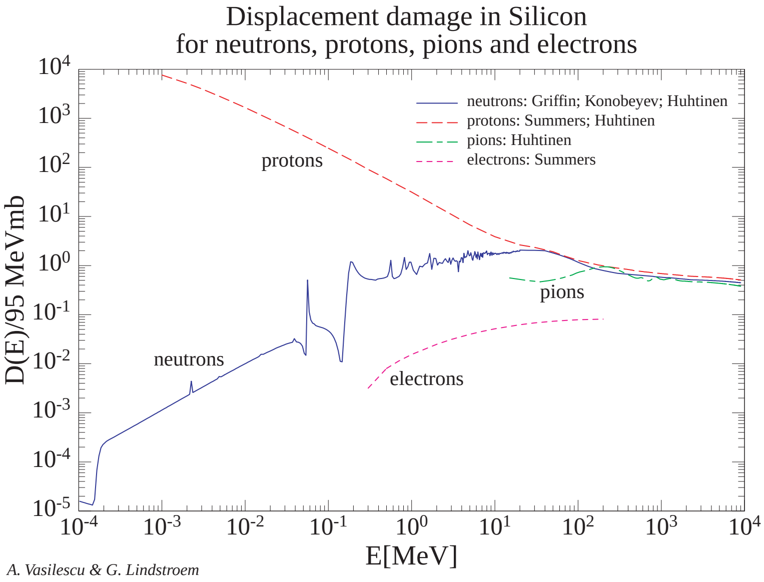

Figure 4.1: Displacement damage in Si for various hadrons [36]

Although the Lindhard Partition function is well known for Si [38] and has been calculated recently for GaAs [39] and SiC [40], no calculation has yet been made for GaN. For this reason, fluences of hadrons will be given in real terms as opposed to 1 MeV neutron NIEL equivalences. Current work by S. Dittongo et al [41] has recently questioned the validity of the NIEL hypothesis.

4.3.4 e-h Pair Yield

The yield, Y, of a semiconducting material is the number of e-h pairs created by a MIP (minimum ionising particle) in a thickness x. Using the specific ionisation dE/dx and the electron hole pair creation energy, δ, we have

$$Y = \frac{(dE/dx) \times x}{\delta} \tag{4.16}$$

dE/dx is calculated using the Bethe-Bloch equation for relativistic electrons (as shown in eqn (3.33) of Chapter 3). For a compound semiconductor XY,

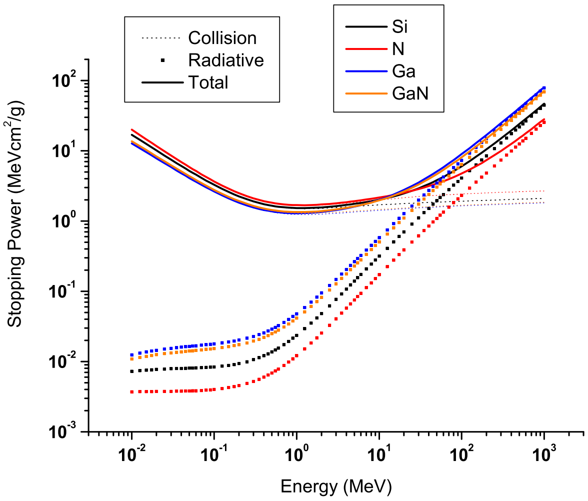

Figure 4.2: Specific energy loss (stopping power) for silicon, gallium, nitrogen and gallium nitride [42]

$$\frac{dE}{dx} = \sum w_j \times \frac{dE}{dx}_j \tag{4.17}$$

For GaN

$$\frac{dE}{dx}_{GaN} = 0.833 \times \frac{dE}{dx}_{Ga} + 0.167 \times \frac{dE}{dx}_{N} \tag{4.18}$$

The stopping powers for Si, Ga, N and GaN are shown in Fig 4.2. From this graph we can see that for a 1 MeV electron in GaN

$$\frac{dE}{dx}_{MIP} = 1.12\ MeV/cm \tag{4.19}$$

From the linear relationship shown in Fig 4.3 we have $\delta_{GaN} \sim 8.9\ eV$. Therefore, using eqn (4.16), our yield from a 1 MeV electron in 1 μm GaN can be calculated as

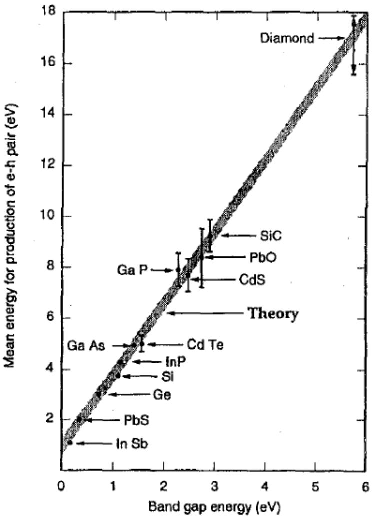

Figure 4.3: Mean energy for calculation of an electron-hole pair in various materials [43]

$$Y = \frac{581(eV/\mu m) \times 1(\mu m)}{8.9(eV/eh\ pair)}) \sim 65\ eh\ pairs \tag{4.20}$$

4.4 Charge Collection Efficiency Measurements

4.4.1 CCE using Am^{241} Source

Unlike silicon. where the standard detector wafer thickness is $\sim$ 300 μm, the typical thickness of GaN epilayers grown on sapphire is $\sim$ 2μm. Using the value given from eqn (4.17), the number of e-h pairs created by a MIP in 2 μm of GaN can be calculated as

$$n(eh/2\mu m) = Y/\mu m \times 2/\mu m = 65 * 2 = 130 \tag{4.21}$$

This low number of e-h pairs indicates that using MIPS (for example from a Sr^{90} source) is not suitable for calculating the charge collection efficiency (CCE) of GaN detectors. An α particle source was found to be more suitable. Seen in Fig 4.4 is the Bragg curve for Am^{241} 5.48 MeV α particles in GaN. Integrating under the curve we find that the energy deposited in 2 μm of GaN ~ 533KeV, corresponding to 6×10^5 e-h pairs

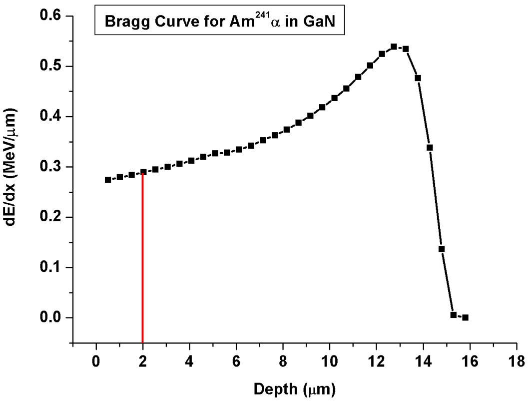

Figure 4.4: Bragg Curve for GaN [29]

$$n(eh) = \frac{533000eV}{8.9eV} = 59888 \sim 6 \times 10^5 \tag{4.22}$$

4.4.2 Experimental Set-up

The CCE measurement setup is shown in Fig 4.5.The sample to be measured is housed with the Am^{241} source in a chamber, which is held under vacuum

(≤20 mbar). The sample is connected to an Ortec 141 charge sensitive pre-

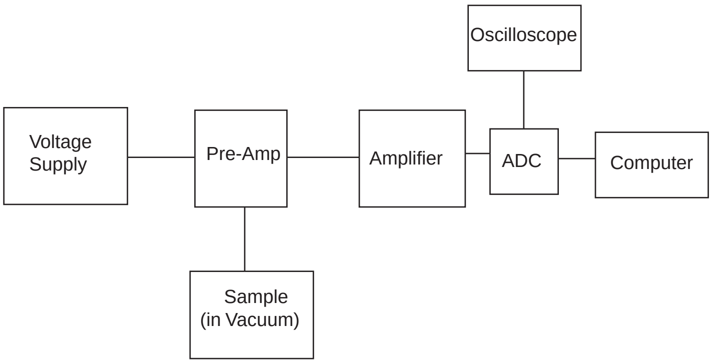

Figure 4.5: Experimental setup for CCE measurements

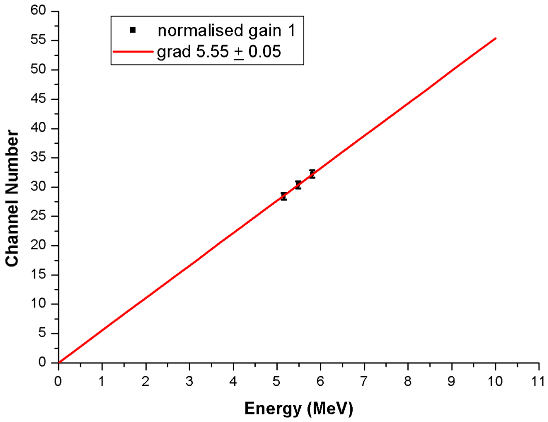

Figure 4.6: Calibration of energy *v's* channel number scale using various spectroscopic sources

amplifier which is connected to an Ortec amplifier, with shaping time of 1 μs. The sample can be biased using a voltage supply to a maximum of 2 kV. The amplifier is connected to a multichannel pulse height analyser. An oscilloscope is used to display α-induced signals in the detector.

4.4.3 Calibration

Spectra of the spectroscopic sources Am^{241}, Pu^{239} and Cm^{244} were taken using a silicon surface barrier diode. As the energies of the particles were known, a linear relationship was made between the energy and the channel number in the data acquisition software (Fig 4.6). To calculate the correct CCE for the GaN samples from the calibration, a correction for the different values of electron-hole pair creation energies, δ, has to be made

$$CCE(\%) = \frac{(E_M) \times (\frac{\delta_{GaN}}{\delta_{Si}})}{E_D} = \frac{E_M \times \frac{8.9}{3.6}}{E_D} \tag{4.23}$$

where E_M and E_D are the measured and deposited energy, respectively. An example of the α-induced peaks can be seen in Fig 4,7

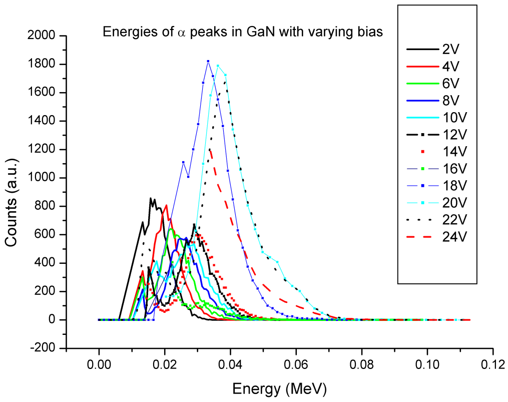

Figure 4.7: α-induced peaks in GaN for varying bias

4.5 Results

The material used for testing was semi-insulating GaN, grown by Tokushima University using Metal Organic Chemical Vapour Deposition (MOCVD) techniques onto an Al_20_3 (0001) substrate. The material was 2 μm thick, grown on a buffer layer of 2 μm n^+ GaN (Fig 4.8). The properties of the layers were changed by variation of the substrate temperature and the Tri-Methyl-Gallium (TMGa) flow rate during growth [44].

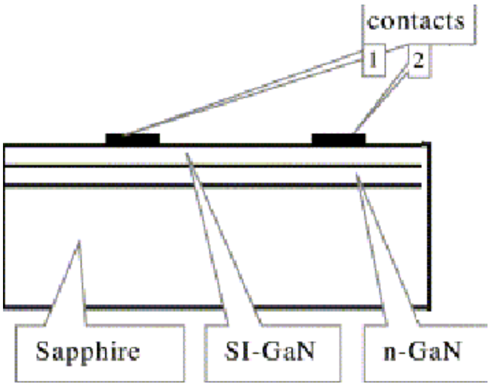

Figure 4.8: MOCVD grown semi-insulating GaN

Au Shottky pad contacts were realised by the manufacturers. I-V characteristics were taken using a Keithley electrometer, and CCE values were measured for a range of applied voltages.

4.5.1 Pre-Irradiation

The I-V for the as-grown GaN showed a leakage current of ~ 2 pA up to 15V (Fig 4.9). From this measurement the resistivity was determined to be ~ 1×10^8 Ωcm. A maximum CCE of 97% was seen to occur at 15 V. The CCE increased linearly with the applied bias (Fig 4.10).

4.5.2 Neutron Irradiation

Irradiation Facilities

Neutron irradiations were performed at the TRIGA reactor at the Jozef-Stefan Institute in Ljubljana, Slovenia. The samples were irradiated in the

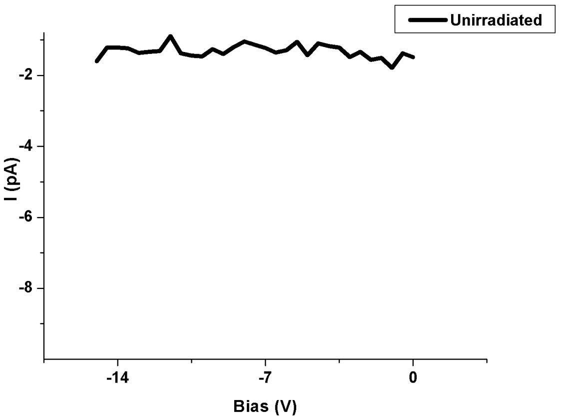

Figure 4.9: Current-Voltage characteristic for unirradiated GaN

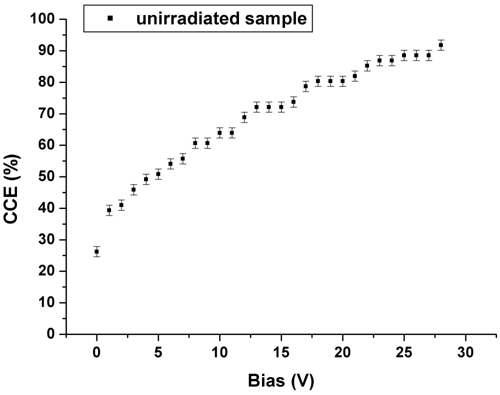

Figure 4.10: CCE for unirradiated GaN

outer tube of the reactor core. The source was tunable by reactor power from $2{\times}10^{9}$ $ncm^{-2}s^{-1}$ to $2{\times}10^{10}$ $ncm^{-2}s^{-1}$ (Fig 4.11). In pulsed mode operation fluences of 10^{14} ncm^{-2} were obtained in 20ms, yielding an effective fluence of 10^{15} $ncm^{-2}s^{-1}$.

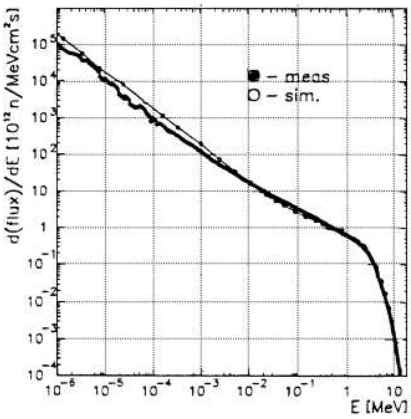

Figure 4.11: Neutron fluence of TRIGA reactor [45]

Results

Diodes were irradiated with fluences of $5{\times}10^{14}$, $1{\times}10^{15}$ and $1{\times}10^{16}$ ncm^{-2}. Fig 4.12 shows the leakage currents measured for the diodes post-irradiation. Fig 4.13 shows a non-linearity of leakage current variation with fluence. This

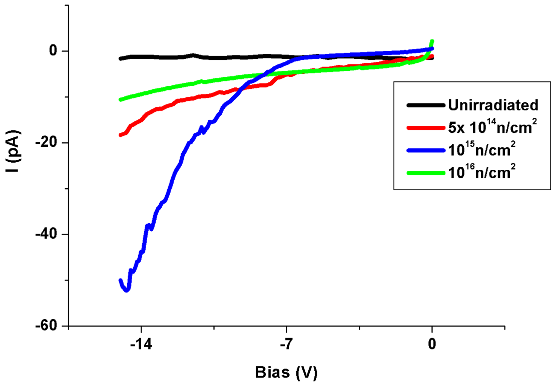

0

Figure 4.12: Current-Voltage characteristics for different fluences of neutron irradiated GaN

differs from previous observations in Si [38], for which

$$I = \alpha \Phi_{eq} V \tag{4.24}$$

where α is the current related damage rate. However, such non-linear effects have been seen before in another wide bandgap material, SiC [46]. The CCE values for 10^{14} - 10^{16} ncm^{-2} irradiated GaN can be seen in Fig 4.14, with the leakage current and CCE changes after irradiation shown in Table 4.3. The neutron irradiated samples showed a decrease in CCE with fluence, while

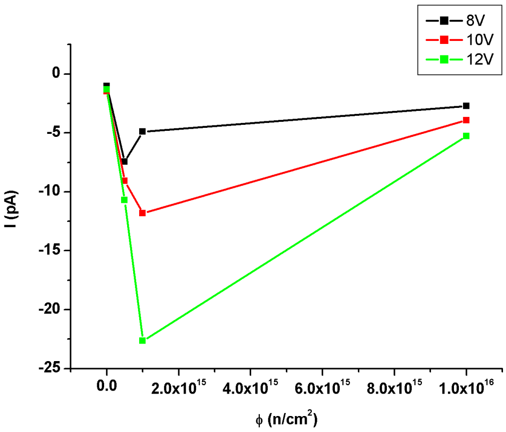

Figure 4.13: Leakage current against fluence

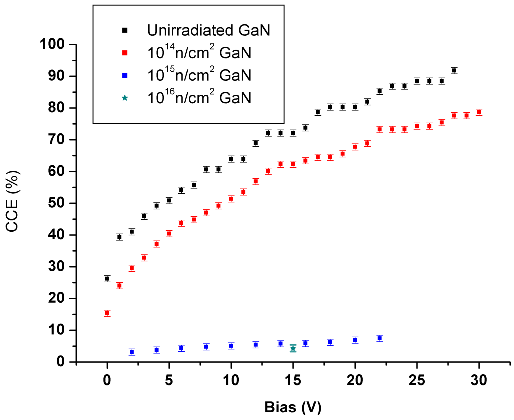

Figure 4.14: CCE for all n irradiated GaN

the leakage current showed a non-linear increase with fluence. One possible explanation for this is the introduction of deep level acceptor states in the material. These acceptor states will capture free electrons generated in the material, reducing leakage current levels, but also reducing measured CCE levels. Evidence of deep level trapping/de-trapping was seen in the increase in low-level noise in the CCE measurement set-up for 10^{15} ncm^{-2} and 10^{16} ncm^{-2} samples. A more detailed investigation of radiation induced trapping is discussed in Chapter 5.

	I(pA)(15 V)	$\times$ I_{UN}(pA)	CCE(%)(15 V)	CCE Drop(%)	CCE_{MAX}(%)
Unirradiated	1.6	1	72.12	0	96.78 (30 V)
10^{14} ncm^{-2}	18.3	11.44	62.28	9.84	78.7 (30 V)
10^{15} ncm^{-2}	50	31.25	6	66.12	7.4 (22 V)
10^{16} ncm^{-2}	10.55	6.59	4.45	67.67	4.45 (15 V)

Table 4.3: Effect of neutron irradiation on the leakage current and CCE of GaN diodes

4.5.3 Proton Irradiation

Irradiation Facilities

Proton irradiation was performed at CERN, Geneva. The irradiation zone used was IRRAD-1, where samples can be exposed to a 24 GeV/c proton beam. Fluences of up to 3×10^{13} $pcm^{-2}s^{-1}$ are achievable. Irradiations were performed by M. Glaser and M. Moll.

Results

A GaN diode was irradiated to a fluence of 1×10^{16} pcm^{-2}. As for the neutron irradiations, measurements were made of the I-V characteristic and of the CCE for varying bias voltages (Figs 4.15 & 4.16). The low levels of leakage current measured (20 pA at 15 V) were similar to the currents measured in the 10^{16} ncm^{-2} irradiated sample, however CCE levels were higher for the $1{\times}10^{16}pcm^{-2}$ than for the $1{\times}10^{16}$ ncm^{-2} irradiated diode.

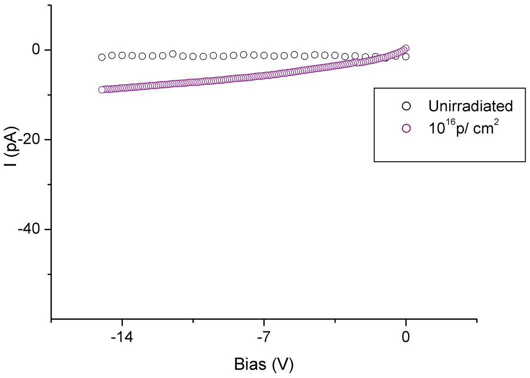

Figure 4.15: Current-Voltage characteristic for proton irradiated GaN

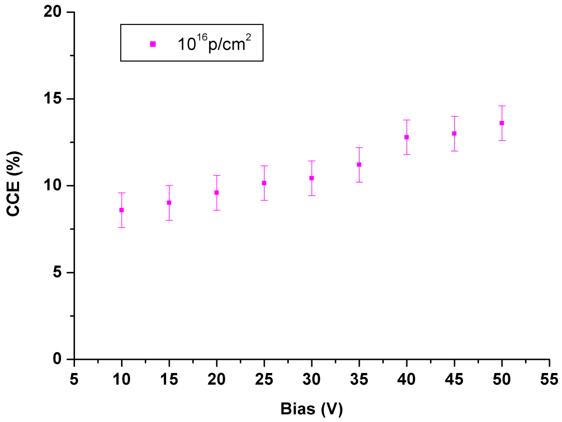

Figure 4.16: CCE for proton irradiated GaN

4.5.4 X-ray Irradiation

Irradiation Facilities

The X-ray irradiation was performed at the Imperial College Reactor Centre [47].

Results

A GaN diode was irradiated with 600 MRad of 10 keV X-rays. Shown here are the I-V characteristic (Fig 4.17) and CCE (Fig 4.18) post irradiation.

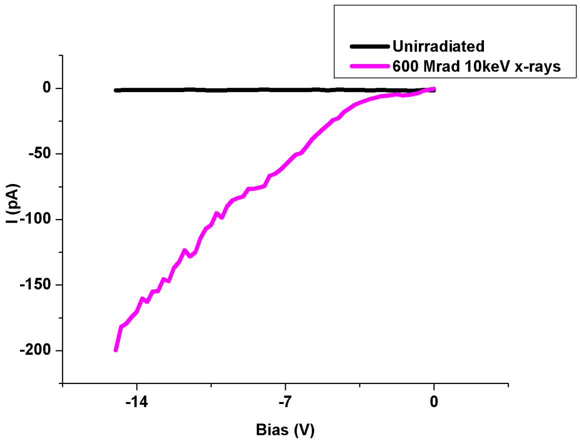

Figure 4.17: Current-Voltage characteristic for X-ray irradiated GaN

A notable increase in leakage current was seen (300 pA at 15 V), although no degradation was observed in CCE level. This combination of effects may be attributed to surface damage, which would contribute significantly to the leakage current but have no effect on the space charge region, and hence CCE values.

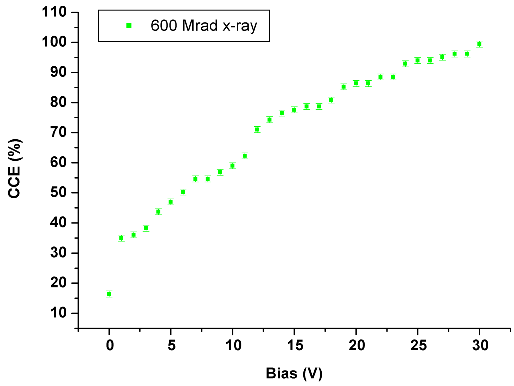

Figure 4.18: CCE for X-ray irradiated GaN

4.5.5 Comparisons

In contrast to GaN, the most recent data taken for irradiated DOFZ Si n-in-n microstrip detectors [48] (Table 4.4) show CCE values of 100% for a NIEL equivalence of 3.52×10^{14} ncm^{-2} after increasing the operating voltage from 70 to 500V. At the highest fluence measured, 4.40×10^{15} ncm^{-2}, the CCE showed a decrease to 30% CCE at 850 V, higher than the CCE measured for GaN. This suggests that it is possible to extract a higher CCE from DOFZ Si than from GaN.

However, this requires a substantial increase in operating voltage, and a possible decrease in operating temperature. Such changes substantially increase the power necessary for the continuous operation of a detector. The values of CCE for the GaN samples tested here required no reduction in temperature and no significant increase in operating voltage.

Material	Fluence (p)	Fluence (n)	CCE_{MAX} %	V @ CCE_{MAX}
GaN	Unirrad	Unirrad	97	30
GaN	10^{14}	-	79	30
GaN	10^{15}	-	7.4	22
GaN	10^{16}		4.45	15
GaN	-	10^{16}	13.5	30
Si n in p	Unirrad	Unirrad	100	70
Si n in n	6x10^{14}	3.52x10^{14}	100	500
Si p in n	7x10^{14}	4.11x10^{14}	100	500
Si n in n	6x10^{14}	3.52x10^{14}	100	500
Si n in n	1.10x10^{15}	6.46x10^{14}	75	800
Si n in n	3x10^{15}	1.7x10^{15}	60	820
Si n in n	7.5$10^{15}$	4.40x10^{15}	30	850

Table 4.4: Effect of neutron irradiation on the leakage current and CCE for GaN and silicon detectors [48]

4.6 Summary and Future Work

The GaN samples tested in this work have been shown to possess good electrical properties, ensuring its effectiveness as a detection material. The low leakage currents measured allow detectors to run at low noise levels at high biases. A drop of 18% in CCE is measured after the material is irradiated with a fluence of 10^{14} ncm^{-2}. Although this drop is significant, the diode requires no increase in operating voltage. The diodes were also tested pre- and post-irradiation at room temperature. Stabilising both the operating bias and temperature is beneficial when considering the power necessary for continuous operation of a detector.

However, the disadvantages of the tested material are twofold :-

1. The material shows a rapid decrease in CCE values for very high hadronic fluences

2. The material is only 2 μm thick

The yield of material is also an issue for GaN (and most other alternative materials to Si) as a viable detecting material for large experiments. GaN grown on sapphire cannot utilise many diode configurations, as contacts cannot be realised to the back of the substrate. An increase in thickness of GaN from 2 μm would also be necessary for its use as a tracking detector.

However, further work is necessary before conclusions can be made for GaN as a rad-hard material. Currently, investigations are about to begin using thicker GaN. Together with up to 25 μm thick GaN, now commercially available, one manufacturer [49] has now produced bulk (>250 μm) GaN, and made it available for initial characterisation. If such thicknesses of material can be seen to be as a radiation-hard as 2 μm GaN, then there is a possibility that GaN could be used for certain specialised areas, such as synchrotron radiation monitoring, currently an area explored using another wide bandgap material, CVD diamond [50].

Chapter 5

Defect Characterisation

5.1 Introduction

When characterising the electrical properties of semiconducting radiation detectors, it is necessary to take into account the defects they may possess and their possible impact on operating performance. For (Al)GaN, the defect density is thought to be as high as $10^{15}\ cm^{-3}$ [11]. As well as being caused by impurities, the vast majority of these defects are thought to be structural defects, introduced at the growth stage. This chapter will describe the investigations of various types of GaN for evidence of traps and discuss their possible detrimental consequences. These include GaN pre - and post - irradiation with neutrons, protons and X-rays (as described in the previous chapter), as-grown Emcore [51] GaN & AlGaN; Mg doped GaN (before and after p-type activation of the Mg) and GaN grown with a variety of MOCVD growth parameters. Evaluation of defects was carried out through studies of photoluminescence (PL), microwave absorption (MWA), photoconductivity (PC) and thermally stimulated currents (TSC).

5.2 Defects

5.2.1 Effects of Defects

Defects can alter the operation of a semiconducting detector in three main ways.

- Defects with low activation energies can act as donors or acceptors, modifying the doping concentration of a semiconductor operated at room temperature
- They can reduce the S/N of the detectors. This occurs if a filled trap releases an electron or hole while e-h pairs are being collected after generation from deposited energy, increasing the noise of the signal. Alternatively, generated charge can be trapped, preventing it from being swept to the electrode and degrading the signal.
- Modification of the electric field distribution within the SCR can also occur if the defect is charged

Defects can be classified into two types: radiative and non-radiative. For radiative centres, a photon will be emitted on de-excitation. This does not occur for non-radiative centres, where the energy difference is dissipated by some other means, most commonly as lattice vibrations (phonons).

Defects are commonly introduced at the growth stage, and are therefore intrinsic to the material. Further defects, however, can be introduced via ageing effects throughout the operational lifetime of the detector. The results from chapter 4 suggested that the degradation in CCE and variations in leakage current after irradiation were due to radiation induced defects.

However, it is also important to detail the as-grown defects associated with GaN. (The average density of defects in GaN has been reported to be in the order of 10^{15} cm^{-3} [11]). The following section outlines the most prominent defects in GaN and details their origin.

5.2.2 Defects in GaN

Nonintentionally doped GaN is usually n-type, and can have electron concentrations n $\geq 10^{18}$ cm^{-3}. The dominant donor is believed to be the nitrogen vacancy, V_N. The binding energy of this donor is subject to controversy, with reported values ranging from 17-42 meV [52, 53, 54] A further V_N deep level donor state is believed to exist at $\sim$ 0.12 eV. Si, Mg and C can all also act as donor states. A wide range of acceptor states in GaN is detailed in Fig 5.1. As well as the donor and acceptor states detailed above, there are more than 30 recognised defect levels in GaN [11]. The next section will discuss briefly the causes of such defects in GaN.

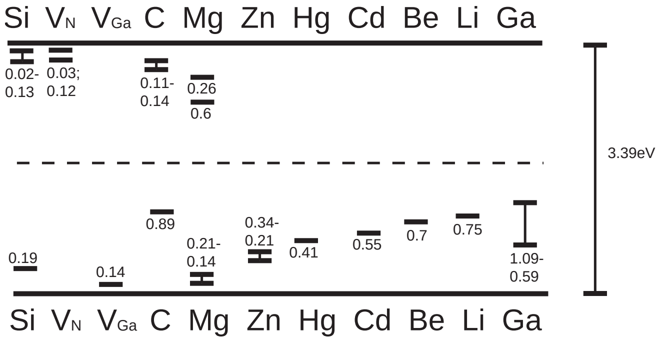

Figure 5.1: Donor and acceptor levels in GaN, where V_{Ga} and V_N denote Ga and N vacancies, and where *Ga* indicates a Ga atom in a N atom site (substitutionals) [55]

Point Defects

Point defects describe defects caused by the absence of an atom from its lattice position, by the switching of atom type in a crystal (eg a Ga atom at a lattice point where a N atom should reside) or by the appearance of an atom between allowed positions in a crystal structure (Fig 5.2). These are known as vacancies, substitutionals and interstitials respectively. Point defects can also occur from the introduction of an impurity atom at a lattice point, or through the creation of Frenkel pairs by incident ionising radiation (detailed in chapter 4). As-grown point defects in GaN are believed to be most commonly Ga vacancies. Such defects can be identified from photoluminescence spectra, as a band peaking at around 2.2 eV.

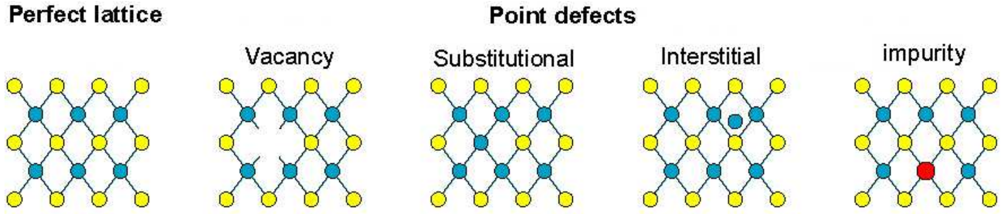

Figure 5.2: Examples of a perfect lattice (left) and types of point defects (right) in a crystal

Dislocation defects

Of the two main types of dislocations that can occur within a crystal structure, edge dislocations and screw dislocations (Fig 5.3), the latter is most common in GaN. It is caused during the growth process when the hexagonal columns of GaN twist as they grow laterally from the substrate, causing 60^0 basal plane dislocations. There is a lattice mismatch ($\sim$13.5%) between the

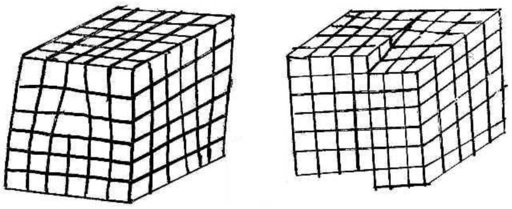

Figure 5.3: Examples of an edge dislocation (left) and a screw dislocation (right) in a crystal

sapphire substrate and GaN and there is also a thermal mismatch. The thermal expansion coefficients for sapphire and GaN are $\frac{\Delta a}{a} = 7.5 \times 10^{-6}\ K^{-1}$ and $\frac{\Delta a}{a} = 5.59 \times 10^{-6}\ K^{-1}$. respectively. For GaN, such dislocation defects are seen as peaks at ~2.85 eV in PL spectra.

Several methods can be used to identify defects in materials. Photoluminescence, Microwave absorption (MWA), Photoconductivity (PC) and Thermally stimulated current (TSC) methods were used in the present work. Details of each method and their results will now be described.

5.3 Photoluminescence

5.3.1 Theory

Photoluminescence spectroscopy is a contactless, nondestructive method of probing the electronic structure of materials. A monochromatic light source with known photon energy illuminates the surface of a material, where some of the light is absorbed by exciting electrons into a permitted higher energy state. When the electron returns to its equilibrium state, light is released. The energy of the emitted light gives an indication of the energy difference between the equilibrium and excited states of the electron. In a semiconductor, therefore, this energy difference may relate to the bandgap, or to a defect of known energy. The intensity of emitted light - or photoluminescence - can also give an indication of the intensity of transitions occurring.

There are four main applications [56] for which photoluminescence can be used:

- Bandgap determination. The most common radiative transition in semiconductors is across the bandgap.
- Impurity levels and defect detection. Radiative transitions in semiconductors involve localised defect levels. The photoluminescence energy associated with these levels can be used to identify specific defects, and the intensity of photoluminescence can be used to determine their concentration.
- Recombination mechanisms. Recombination can involve both radiative and nonradiative processes. The amount of photoluminescence and its dependence on the level of photo-excitation and temperature are directly related to the dominant recombination process. Analysis of photoluminescence helps to understand the underlying physics of the recombination mechanism.
- Material quality. In general, nonradiative processes are associated with localised defect levels, whose presence is detrimental to material quality and subsequent device performance. Thus, material quality can be characterised by quantifying the amount of radiative recombination.

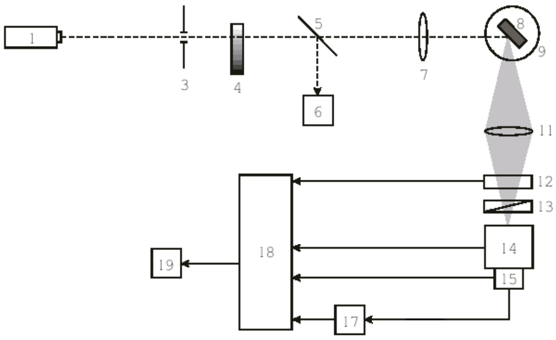

Figure 5.4: Schematic diagram of the photoluminescence measurement setup

5.3.2 Experimental Setup

The experimental setup for the PL measurements is detailed in Fig 5.4. Room temperature photoluminescence measurements were carried out using a continuous wave (cw) He-Cd laser operating at 325 nm (1). The laser passed through a pinhole (3), a filter (4) and series of lenses (7 & 11). The intensity of the laser was measured using a beamsplitter (5) and photodiode gauge (6). A particular wavelength from the photoluminescence emanating from the sample (8) was selected using a mechanical shutter (12), a polariser (13) and monochromator (14). The intensity of the specified wavelength was then measured using a photo-multiplier tube (15) and single photon counter (17), which passed the signal to the computer (19) via a control unit (18).

5.3.3 Results

Pre Irradiated GaN

Fig 5.5 shows the PL spectrum taken from as-grown GaN before irradiation. The spectrum shows a good agreement with previous measurements of GaN [57, 58], with the observed spectra showing four bands. An ultraviolet band

(UVB) peak at 3.4 eV is attributed to band-to-band recombination. This ultraviolet band is accompanied by a violet band (VB) peak at 3.36eV, a yellow band (YB) peak at 2.18 eV and a blue band (BB) peak at 2.85 eV. The blue band peak has been interpreted as evidence of a high density of dislocations [59]. The yellow band is attributed to point defects, eg Ga vacancies [59, 60], whereas the violet peak is thought to be caused by donor-acceptor recombination [57].

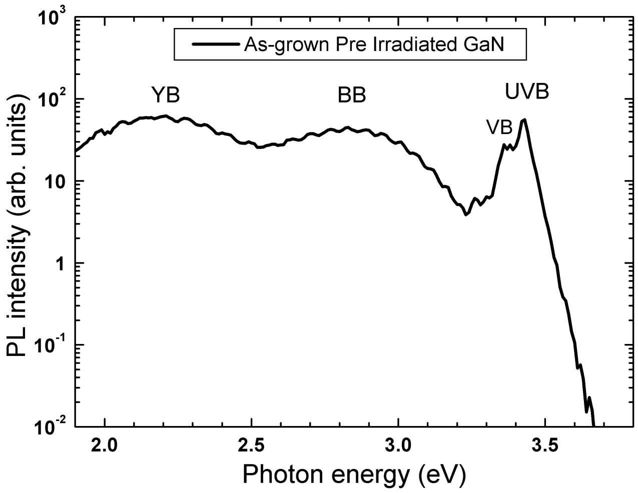

Figure 5.5: Photoluminescence spectra for GaN pre-irradiation

Post Irradiated GaN

PL spectra were measured after irradiation of GaN with X-rays, neutrons and protons as detailed in chapter 4. It was found that the intensities of all 4 peaks dropped by a significant amount (Fig 5.6 & Table 5.1). This can be attributed to an increase in non-radiative recombination through radiation

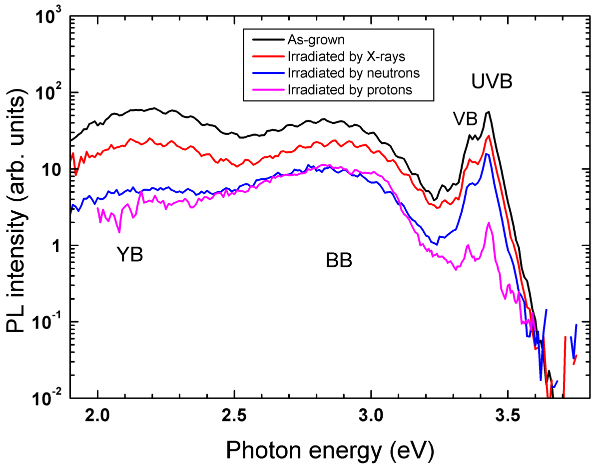

Figure 5.6: Photoluminescence spectra from GaN post-irradiation with X-rays, neutrons and protons

Material/Sample	Band to Band	Violet Band	Blue Band	Yellow Band
Non-irradiated	-	-	-	-
X-rays	2.1	2.2	1.9	2.6
n irrad	3.5	4.2	4.3	11.2
p irrad	35	33	5	11

Table 5.1: Factor of decrease in intensity of PL bands for GaN post irradiation

introduced defects. This increase in radiation induced defects is a possible explanation for the degradation in CCE levels for the irradiated diodes shown in chapter 4. Furthermore, the intensity of the YB peak falls more dramatically than the UVB, VB and BB peaks. This suggests that point defects may undergo a modification under irradiation, transforming many into non-radiative recombination centres. However, those defects caused by dislocations, indicated by the intensity of BB peak, seem to undergo no such transformation.

Emcore Material

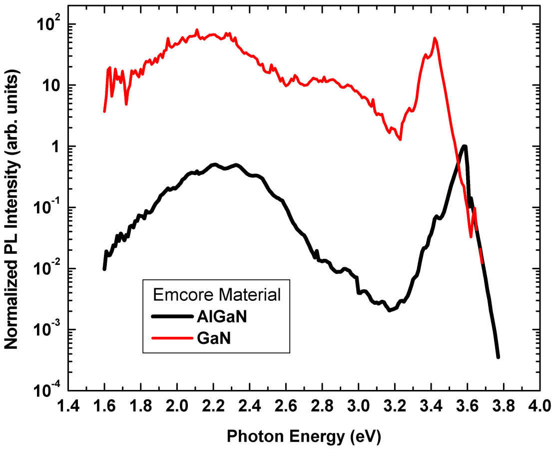

Figure 5.7: Photoluminescence spectra for Emcore AlGaN and GaN material

Two wafers grown by MOCVD by Emcore [51] were tested. Both wafers were unintentionally doped. The resistivity of the wafers and the Al molar fraction of the AlGaN wafer were not supplied by the manufacturers. A PL spectrum was measured for a sample of Emcore AlGaN (Fig 5.7). The spectrum shows a very large YB peak, indicating a very high density of point defects, possibly introduced at the growth stage of the Al capping layer. It has been shown previously that the intensity of the YB peaks depends on the Al molar fraction [61]. As the molar fraction of Al in the AlGaN was not supplied by the manufacturers, the Al content was calculated using the PL spectrum as follows. The bandgap of AlGaN is found using

$$E_g(x) = E_gGaN(1-x) + E_gAlN(x) - bx(1-x) \tag{5.1}$$

where E_gGaN $= 3.2$ eV, E_gAlN $= 6.2$ eV, $x =$ molar fraction of Al and b is the bowing parameter (∼0.8 [4]). The band-to-band recombination peak for the AlGaN sample is situated at 3.6 eV. Therefore

$$3.6 = 3.2(1-x) + 6.2(x) - x(1-x) \tag{5.2}$$

Solving for x, we find

$$x \sim 0.1 \tag{5.3}$$

Therefore, the Al molar fraction of the material is 10%. The PL spectrum for an Emcore GaN sample is also shown in Fig 5.7. The intensities for all peaks at the same light intensity (9 mW) are higher for GaN than for the AlGaN. This suggests that the AlGaN has a greater number of non-radiative centres, and consequently, is of poorer material quality.

Tokushima Material

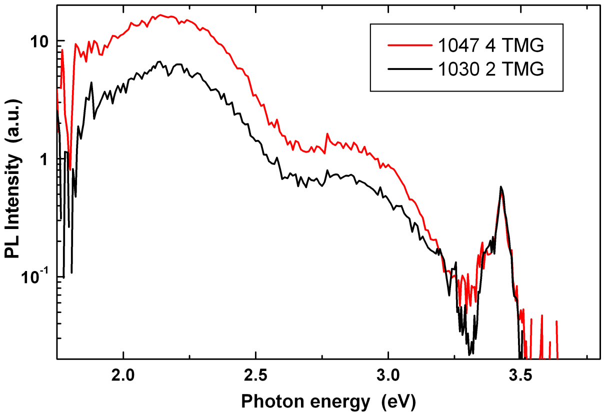

Figure 5.8: Photoluminescence spectra for GaN grown with varied TMG flow rate (2 and 4 TMG indicates double and 4 times the standard TMG flowrate, respectively)

Tri-methyl gallium (TMG) and ammonia are commonly used as precursors for Ga and N in GaN when grown using the MOCVD method. To investigate the effect of altering the flow rates of the pre-cursors, GaN wafers with varying TMG flow rates were supplied by Tokushima University. The effect of doubling the TMG flow rate can be seen from the PL spectra in Fig 5.8. It can be seen that although the intensities of the UV peaks are similar, there is an increase in intensity of the YB and BB peaks with increased TMG flow rate, suggesting that the increased TMG flow rate has introduced a greater density of defects into the material.

Mg Doped GaN

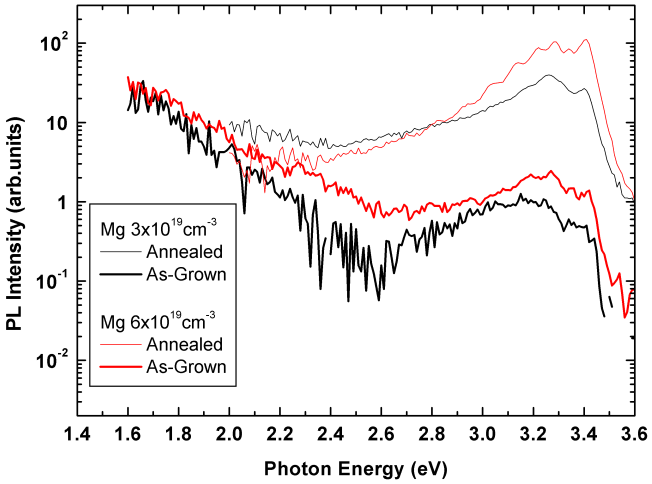

Figure 5.9: Photoluminescence spectra for as-grown and annealed (activated) Mg doped GaN

2 GaN wafers were grown by Compound Semiconductor Technologies [62]. The wafers were doped with 3.2×10^{19} and 6.2×10^{19} atoms cm^{-2} of Mg, which acts as an acceptor in GaN, and is used for the production of p-type material. The material was annealed at 1100^0C for 5 minutes to activate the Mg. PL

spectra for both samples were taken before and after activation of the dopant (Fig 5.9). Before annealing, small peaks occur at 3.264 eV in the samples, indicating that they are already partially activated. The increase in these peaks can be seen for both samples after activation.

5.4 Microwave Absorption & Photoconductivity

5.4.1 Theory

Microwave absorption (MWA) [63, 64, 65] is an effective, non-invasive tool for the monitoring of excess carrier behaviour due to recombination and trapping processes in semiconductors. In a semiconductor, bound electrons will not absorb microwaves. For microwaves to be absorbed, a material is needed that contains free electrons - electrons contained in the conduction band and able to carry current if a voltage is applied across it. This condition can arise if semiconductors are exposed to light, which creates e-h pairs. From the intensity and period over which the microwaves are re-emitted on de-excitation, we can gain an indication of the relaxation time of the excess carriers and, consequently, the existence of defects.

For photoconductivity (PC) measurements, the increase in conductivity of the semiconductor due to photogenerated current is recorded through the drop in voltage across a resistor. Similarly as for MWA, the time dependence in the fall of conductivity (and hence voltage drop) gives an indication as to the relaxation time of the generated carriers.

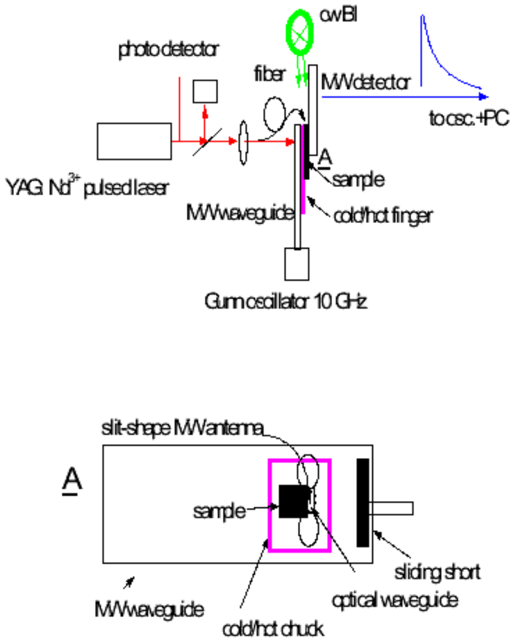

Figure 5.10: Schematic set-up for MWA and PC measurements

5.4.2 Experimental Setup

In the set-up in Fig 5.10, a pumped Nd-Yag laser was used with second and third harmonic generators to produce 3 excitation wavelengths: UV (266 nm), Green (532 nm) and IR (1064 nm). Using various filters the source could produce any one, two, or all three signals simultaneously. For MWA, the source has a pulse duration of 10-100 ns, to satisfy the approximation of a δ-pulse (a 30 ps light pulse was used for PC measurements), and is focused ($\sim$2 mm) onto the surface of the sample. Microwaves with a frequency of 10-21 GHz and power of 100-200 mW are generated by a Gunn diode source and used to probe the excited area of the sample. A MW detector is then used to measure in either reflection or absorption mode. Transients of the reflected or transmitted microwaves are recorded by a digital oscilloscope. The same setup was used for PC measurements, using wire connections to the metal contacts on the GaN.

The relaxation curve of the PC decay and MW absorption/reflection has two characteristic parts: a transient, non-exponential part and an asymptotic exponential part. The effective lifetime for the asymptotic part (τ_{asym}) is given by the time it takes for the amplitude to decrease to 0.1 of its peak value, and is determined by a fitted exponential function.

5.4.3 Results

Irradiated GaN

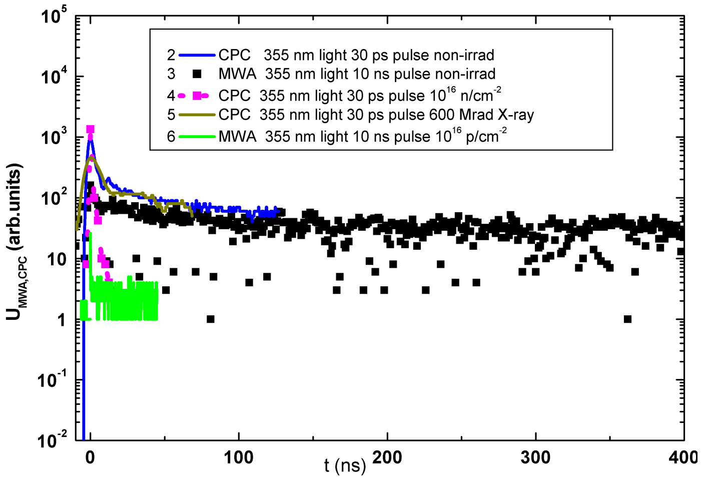

Figure 5.11: MWA & CPC (contact PC) measurements of the transient non-exponential section of de-excitation for pre-and post-irradiated GaN

Fig 5.11 shows the non-exponential section of the decays from MWA and PC measurements of the pre-and post-irradiated GaN in the *ns* time

Material/Sample	τ_{in} (ns)
Non-irradiated	100-500
X-rays	80
n irrad	20
proton irrad	10

Table 5.2: Summary of the transient decay lifetimes in the pre-and post-irradiated GaN samples

region. Table 5.2 shows a rapid decrease in τ_{in} after irradiation with neutrons, protons and X-rays, indicating an increase in non-radiative recombination. This result agrees with those given previously, where the fall in intensity for all PL spectra measured in the post irradiated GaN was attributed to an increase in non-radiative recombination.

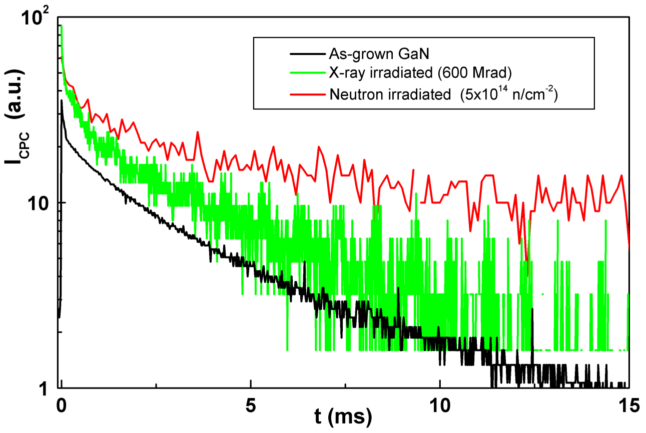

Figure 5.12: PC measurements of the asymptotic section of de-excitation for pre- and post-irradiated GaN

Fig 5.12 shows the asymptotic section of the decay from MWA measurements in the unirradiated, X-ray and neutron irradiated samples. These show an increase in values for τ_{as} relative to pre-irradiation values. One possible explanation for this is that the generated excess carriers are undergoing multi-trapping processes, due to radiation induced trapping centres, and subsequently increasing the values for τ_{as}.

Emcore material

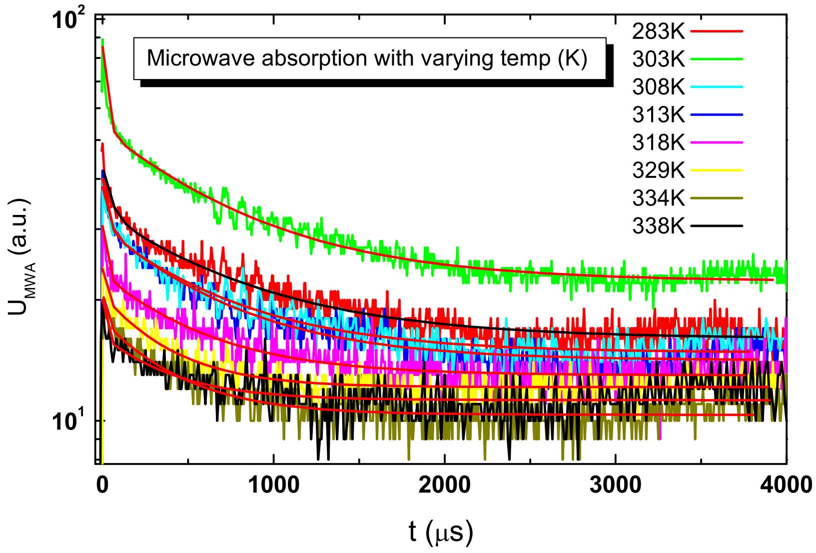

Figure 5.13: MWA measurements for Emcore AlGaN material, performed at varying temperatures

The MWA measurements for the Emcore supplied AlGaN are shown in Fig 5.13. The operating temperature for the measurements varied from 283 K to 338 K. The activation energy of the traps was found by plotting the approximate values for the instantaneous and asymptotic lifetimes against the inverse of kT (Fig 5.14). Traps estimated to have activation energies of 0.675 eV and 0.201 eV were measured. Both are in close agreement with previously published activation energies in (Al)GaN [66, 67].

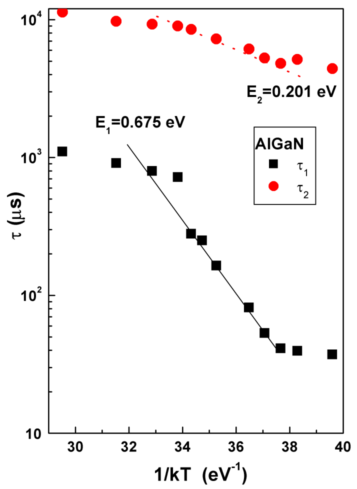

Figure 5.14: The activation energies of traps in AlGaN derived from the temperature variation of MWA measurements

5.5 Thermally Stimulated Currents (TSC)

5.5.1 Theory

Thermally stimulated current (TSC) measurements provide another way of investigating deep level traps in semiconductors in which samples are first reduced to a low temperature, then slowly heated. Any filled traps within the material will empty at a temperature T when the energy corresponding to the trap is close to kT. The activation energy, E_d of a trap can be calculated using the equation [58]

$$E_d = T_m k \times \ln(T_m^4/\beta) \tag{5.4}$$

where β is the heating rate (K/s) and T_m is the temperature (in K) at which the current peak occurs.

5.5.2 Experimental Setup

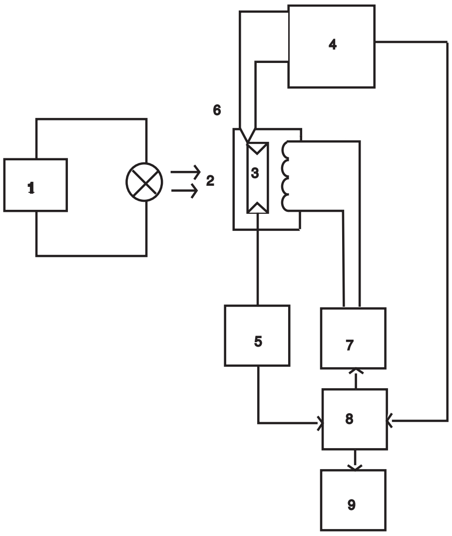

Figure 5.15: Schematic diagram of the TSC measurement setup

The experimental setup for TSC measurements is detailed in Fig 5.15. The wire bonded samples were held within a liquid nitrogen cryostat (3). This allowed measurements to be made in the temperature range 100-300 K. The temperature of the sample was determined from the output voltage of a previously calibrated thermocouple (6) attached to a voltmeter (4), and the heating was controlled by a programmable power supply (7). The TSC current was measured using an electrometer (5), and the samples could be illuminated through a removable cover on the front of the chamber (2), using a halogen lamp source (1). The output was then passed to a PC (9).

5.5.3 Results

Emcore GaN

The thermally stimulated current for the GaN sample was measured at a bias voltage of 5 V. The voltage range for measurements was limited by the leakage current. Fig 5.16 and Table 5.3 show a number of traps with their associated calculated activation energies.

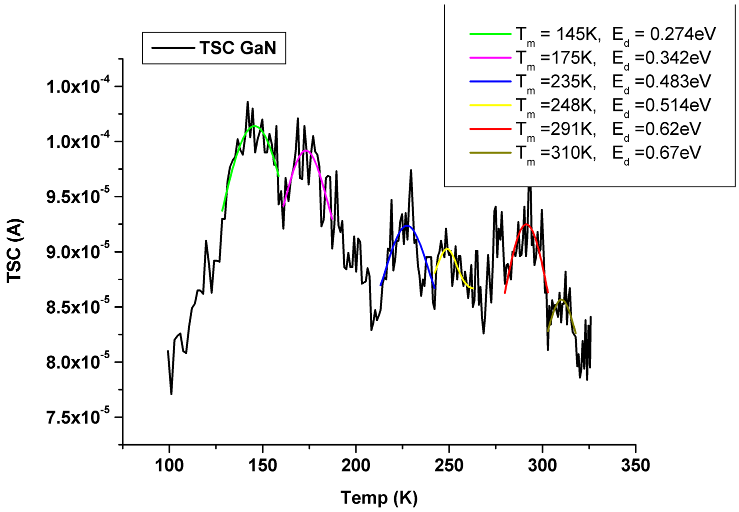

Figure 5.16: TSC measurements for Emcore GaN

Temperature (K)	E_d(eV) (Measured)	E_d(eV) (Referenced)
145	0.27	0.25 [68]
175	0.34	0.35 [69, 68]
235	0.48	0.45 [68]
248	0.52	0.53 [69]
291	0.62	0.62 [69]
310	0.67	

Table 5.3: Activation energy of defects in GaN identified through TSC measurements

The defect levels measured are similar to those reported in previous work

[69, 68]. The differences between the reported and measured activation energies can be attributed to the low heating rate. The defect at 0.67 eV was also identified in the AlGaN sample, suggesting that this trap is not caused by the growth of the Al capping layer, but is in fact, a homogeneous native defect.

Tokushima GaN

A GaN sample grown by Tokushima University was measured for thermally stimulated current at negative bias voltages of 5V, 10V and 15V. The TSC measurements in Fig 5.17 show a defect with an activation energy of 0.57 eV, which is present for all biases, and has been reported previously [66] However, a defect with an activation energy of ∼0.2 eV can only be be seen with an increased applied bias. Such an effect has not been reported on GaN elsewhere.

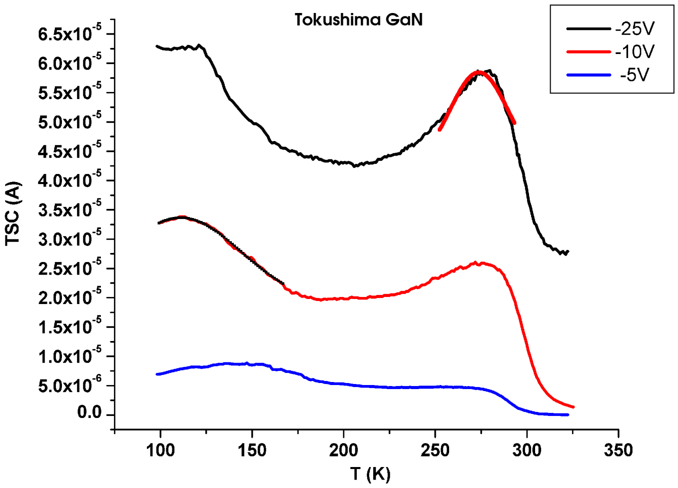

Figure 5.17: TSC measurements for Tokushima grown GaN

5.6 Summary and Future Work

Various techniques have been used to characterise defects in a wide range of GaN materials. Samples irradiated with X-rays, protons and neutrons have been investigated using photoluminescence, MWA and PC measurements. Results indicate an increase in non-radiative recombination centres. This was shown through a decrease in all PL peaks, and through the decrease in the instantaneous carrier lifetimes from MWA and PC measurements. An increase in asymptotic lifetimes suggests that excess carriers undergo a multi-trapping process after irradiation. PL measurements also indicate a rapid decrease in intensity for the YB peak, indicating a transformation of point defects into non-radiative centres. Dislocation defects appear to be unchanged with irradiation.

Photoluminescence spectra were also used to identify the molar fraction of Al present in an Emcore AlGaN wafer, which was found to be $\sim$10%. PL was also used to show that increasing TMG flow rates in MOCVD growth can significantly increase both point and dislocation defects. The activation of Mg doped GaN was also verified using PL spectra.

A common defect with activation energy of $\sim$0.67 eV is found for two types of Emcore GaN material using both TSC and MWA measurements. The variety of trap levels found throughout the materials is consistent with previous results, suggesting numerous and material dependent defect levels in thin GaN films. Such inhomogeneities in material will also be discussed in the following chapter, where leakage currents for Schottky contacts are shown to vary significantly between similarly grown wafers, and suffer from PPC (persistent photoconductivity) effects.

Chapter 6

UV GaN detectors

6.1 Introduction

Due to the the recent advances in growth technologies [70], GaN has recently become the focus of intense interest [11]. Its direct wide energy bandgap (3.4 eV) makes it a highly promising material for photon detection in the UV range. The addition of Al can lower the cutoff wavelength from 365 to 200 nm. Consequently, no short pass filter is necessary for selective UV detection. Potential uses for GaN UV detectors [71] range from space - based, military and environmental applications to proteomics - the study of proteins. One such example of protein structure studies is that of Circular Dichrosim (CD) [72].

This work details the development of fabrication processes for UV MSM (metal-semiconductor-metal) detectors using (Al)GaN. The effects of varying parameters such as the material composition, diode geometry, surface passivation and Schottky metals are also presented, with the optimised parameters subsequently implemented in the design for a 46-channel diode array to be operated for use in CD measurements using synchrotron radiation; the first time that such MSM detectors have been used for position sensitive detection.

6.2 GaN UV Detectors

In recent years, several different styles of photodiodes have been fabricated on III-nitrides [73]: photoconductors, Schottky photodiodes, metal-semiconductor-metal photodiodes, p-n/p-i-n photodiodes and phototransistors (Fig 6.1). Photoconductors suffer from high levels of persistent photoconductive effects (PPC) and poor UV/visible ratios [74]. Schottky diodes consist of an ohmic contact and a Schottky contact, which is transparent to UV, and can simultaneously act as a barrier to electromagnetic radiation with larger wavelengths. Their time response is RC-limited, and they have proven to be good devices for certain applications [75]. P-n/p-i-n photodiodes have been fabricated recently, although difficulties in doping (Al)GaN to make p-type material still remain a problem [76].

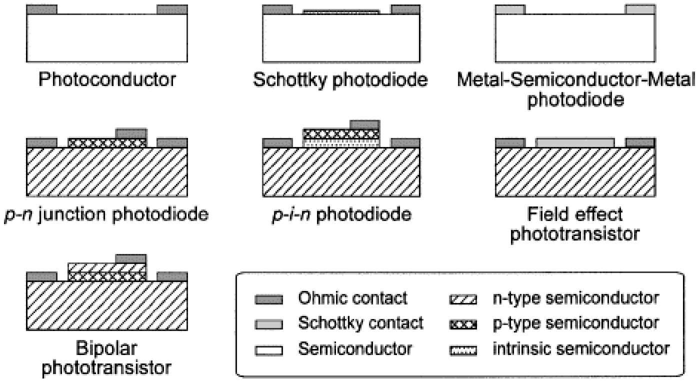

Figure 6.1: Examples of different types of (Al)GaN photodetectors [11]

Metal-Semiconductor-Metal (MSM) photodiodes consist of two Schottky contacts, where the active layer is the area between the contacts. The responses of these devices have been shown to be linear with optical power and have very high UV/visible ratios [77]. Fabrication of MSM diodes is also less complex, with the ability to realise both contacts at the same time, unlike the standard Ohmic-Schottky contact configuration, which requires an ohmic contact with a different contact composition to be annealed (at around 900°C for GaN). MSM UV detectors have been fabricated in this work. The following sections will now describe the design and fabrication process development for such detectors.

6.2.1 Diode Designs

Two diode geometries were used in this work. Initial diode designs used for material characterisation consisted of a 300 μm diameter pad, with a 200 μm wide ring separated from it by a 100 μm gap (Fig 6.2). Such a design is similar to the pad/guard-ring structure used in common pad detectors. However for GaN, metal (ohmic) contacts cannot be realised on the back surface due to the insulating sapphire, and so in this case the "guard-ring" acts as a standard Schottky contact.

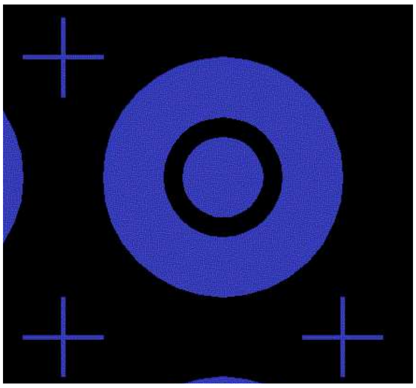

Figure 6.2: An example of pad/ring MSM diode design

For the final UV detectors, interleaving (MSM) finger diodes were employed. Finger diodes (Fig 6.3) are formed using comb-like patterns. This

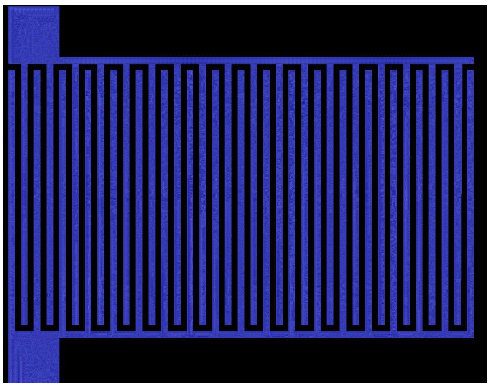

Figure 6.3: An example of an Interleaving finger MSM diode design (Finger pitch & width = 25 μm)

structure is thought to be optimised for UV detection in GaN since:

1. The small pitch between the electrode fingers results in the incident photon being nearer to an electrode. This means that the collection time for generated e-h pairs is reduced.
2. Even though the electrodes are close together (10 μm possibly), using the interleaving finger geometry means the active area (area between the fingers) is not compromised

The diodes were designed using the CAD package, Wavemaker. 3 different finger diodes were used, of overall dimension 2000 μm × 1700 μm, and finger pitch, equal to finger width, 25, 50 and 100 μm. Attached to the sides of the diodes were a set of square bonding pads (200 μm per side).

6.2.2 Diode Fabrication

Two types of lithography were used for fabrication of the diodes

- Photolithography

- E-beam (for features <5 μm)

The following section will now detail the process developed for the fabrication of MSM UV detectors from GaN using photo and electron-beam lithography.

Cleaning

The material was cut into 1 cm^2 squares using a diamond saw. A similar sample cleaning procedure was used for both lithographic techniques. A solvent clean was performed to remove any dirt or remnants of wax left from the cutting of the wafer. The samples were immersed in a beaker of Opticlear and heated in a 60^oC water bath for 10 minutes, followed by 10 minutes in an ultrasonic bath. This was repeated using methanol, acetone and isopropanol. The samples were then dried with an N_2 gun and placed in an oven at 90^oC for 5 minutes.

E-beam

E-beam resist patterning

An electron sensitive resist was applied on top of the substate by spin coating. The most commonly used resist, polymethyl methacrylate (PMMA), was used with different molecular weights and concentrations, varying from 8% '2010' to 12% '2041'. In each case, the resist was applied with a pipette and spun at 5000 rpm for 30 s. The samples were baked for 30 minutes at 180^oC. The sample was then placed in the beamwriter with the desired pattern and was written with a defined dose and spot size.

Dose Tests

To optimise the quality of the written job, a series of dose tests were performed, varying the dose from 200 to 350 μCcm^{-2}. Shown in Fig 6.4 & 6.5 is the improvement after several iterations of dose and developing parameters.

Figure 6.4: Effect of optimising the dose for 10 μm pad features: (left) - Dose=350 μCcm^{-2}; (right) - Dose=250 μCcm^{-2}

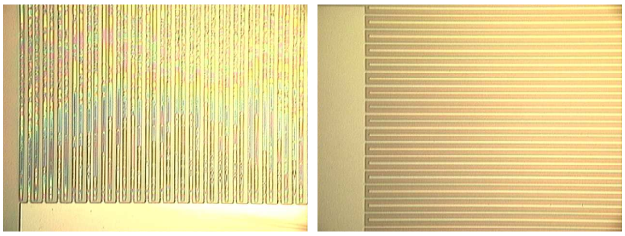

Figure 6.5: Effect of optimising the dose for 3 μm Finger diodes: (left) - Dose=350 μCcm^{-2}; (right) - Dose=250μCcm^{-2}

As an increase in dose required the e-beam to be incident on a spot for longer, the cumulative effect of backscattering resulted in the damage in the resist as seen above. The optimal dose was found to be 250μCcm^{-2} for a 60 s development step.

Bi-Layer Resists

As detailed in Chapter 2, bi-layers of resist are often use to enhance lift-off success. After trying various combinations, a noticeable improvement in lift-off was found when 8% 2010 resist was spun on 12% 2041 resist. The samples were developed in 23^oC 1:1 MIBK:IPA for 60 s. The improvement can be seen in Fig 6.6.

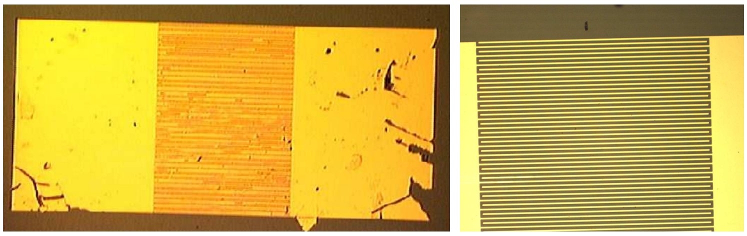

Figure 6.6: Improvement of lift-off using bi-layer resists

Metallisation

To remove any oxide layer from the surface, the samples were cleaned in a 1:1 HCl:RO water solution for 1 minute. Metallisation was performed using a Plassys evaporator. Either a single metal or a combination of metal layers could be deposited. Overall thicknesses of >150 nm were used to help prevent scratching and piercing of contacts by the wire bonds. For lift-off, the samples were placed in heated (60^oC) acetone for 5 minutes. In the event of failed lift-off, unwanted metals were removed in the following solutions: Au (NaI:I:H_20), Ti (HF), Ni (HCl), Pd (Aqua Regia -HCl:HNO_3)

Photolithography

Photoresist patterning

S1818 was the photoresist used for fabrication of the diodes. The photoresist was applied using a syringe and spun at 4000 rpm for 30 s. The samples were soft baked for 30 minutes at 90^oC to remove any remaining solvent in the resist. The samples were then exposed for 4.2 s using a Karl Suss Mask aligner. For improvement of lift-off definition, the samples were soaked in chlorobenzene for 15 minutes after UV exposure. Development was done using a 1:1 microposit : RO water solution for 150 s.

Metallisation

Metallisation was performed in a similar fashion to that described previously. Examples of finished diodes using photolithographic and e-beam techniques are shown in Figs 6.7 & 6.8.

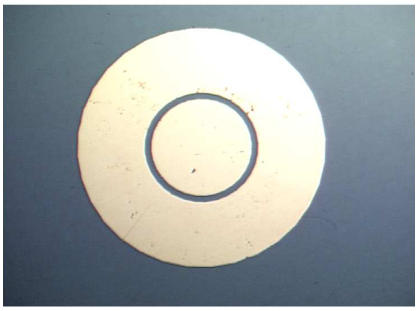

Figure 6.7: Example of a GaN fabricated pad/ring detector using photolithographic techniques

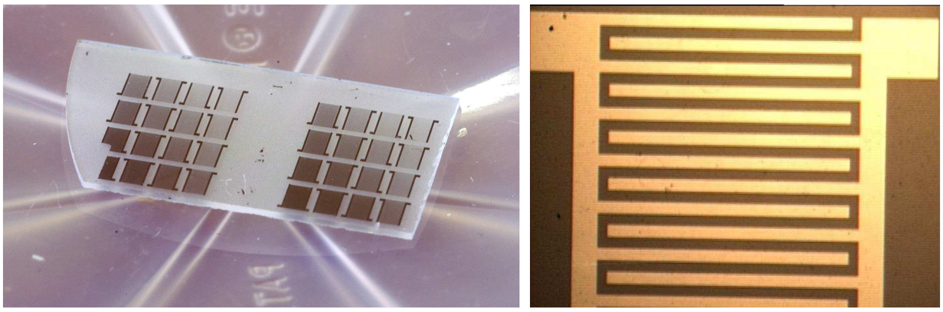

Figure 6.8: Example of GaN fabricated MSM finger diodes using e-beam techniques (left) - An array of 25, 50 and 100μm finger contacts; (right) - 100μm finger contact

6.2.3 Electrical Characterisation

To test the performance of the Schottky contacts on the samples, diodes were wire-bonded using a Hesse and Knipps Bondjet 710M and I-V characteristics were taken using a Keithley 237 electrometer.

Emcore GaN

Fig 6.9 shows the leakage current versus bias voltage for 3 sets of identical pad/ring diodes fabricated on Emcore AlGaN and GaN diodes. Pd(150 nm)/Au(200 nm) was used for the Schottky contact. As both contacts are Schottky and were identical, only one polarity of bias is shown. It can be seen that the leakage current is significantly higher for the AlGaN material.

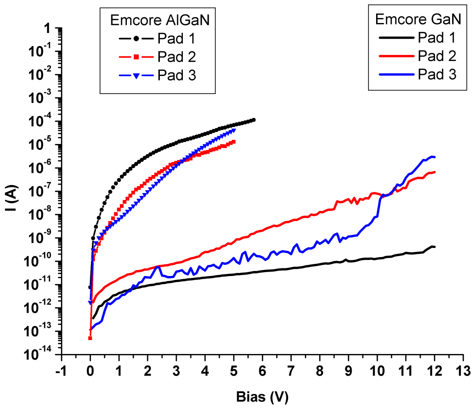

Figure 6.9: I-V characteristics for diodes on Emcore GaN & AlGaN

The dark current (and hence the conductivity) of the GaN is lower than that of the AlGaN by 3 orders of magnitude (10^{-4}A and 10^{-7} A respectively at 6 V). We can also see that the leakage current varies significantly with position of the contacts on the wafer.

Tokushima GaN

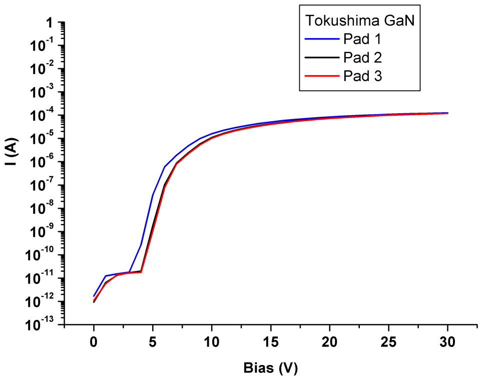

Figure 6.10: I-V characteristics for diodes on Tokushima GaN

Fig 6.10 shows the leakage current for identical diodes fabricated on Tokushima GaN. The results show a lower leakage current than for both Emcore materials.

6.2.4 Persistent Photoconductivity

PPC (Persistent photoconductivity) is prevalent in III-Nitrides. Fig 6.11 shows a series of I-V characteristics for AlGaN diodes after periods (at room temperature) in a light tight probe station. Estimation of the ppc levels was made by fitting an exponential decay to levels of leakage current at 10 mV bias with varying periods of time in the dark. Fig 6.12 shows PPC levels in the Emcore AlGaN sample to decay with a lifetime of $\sim$ 62 minutes. Previous work has suggested that the origin of ppc effects and large densities of point defects (previously described in chapter 5 as a YB PL peak in this sample) may arise from the same intrinsic defect [78].

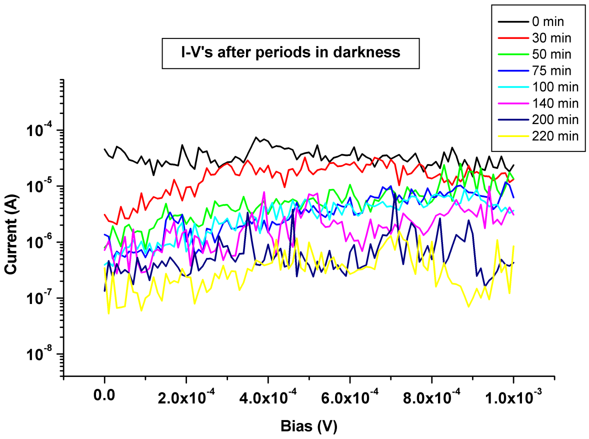

Figure 6.11: The drop in leakage current in AlGaN after periods in dark

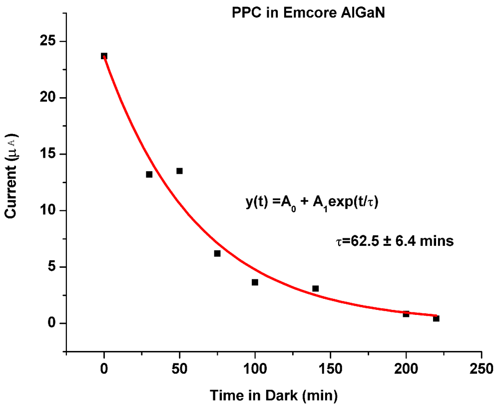

Figure 6.12: Example of PPC effects in AlGaN

6.3 Detector Optimisation

The following section will now report the work done on reducing leakage current levels in the detectors, including variation of the diode geometry. the operating temperature, inclusion of passivation layers and the use of different metals to increase the Schottky barrier height.

6.3.1 Variation of Diode Geometry

The I-V characteristics of diodes with finger pitches of 25, 50 and 100 μm are shown in Fig 6.13. The double Schottky junction can be seen from the symmetrical shapes of the I-V characteristics. Fig 6.13 shows that increasing the finger pitch increases leakage current levels. Fig 6.13 shows this in more detail, suggesting there is a power law dependence on leakage current with finger pitch. From these graphs, we see that

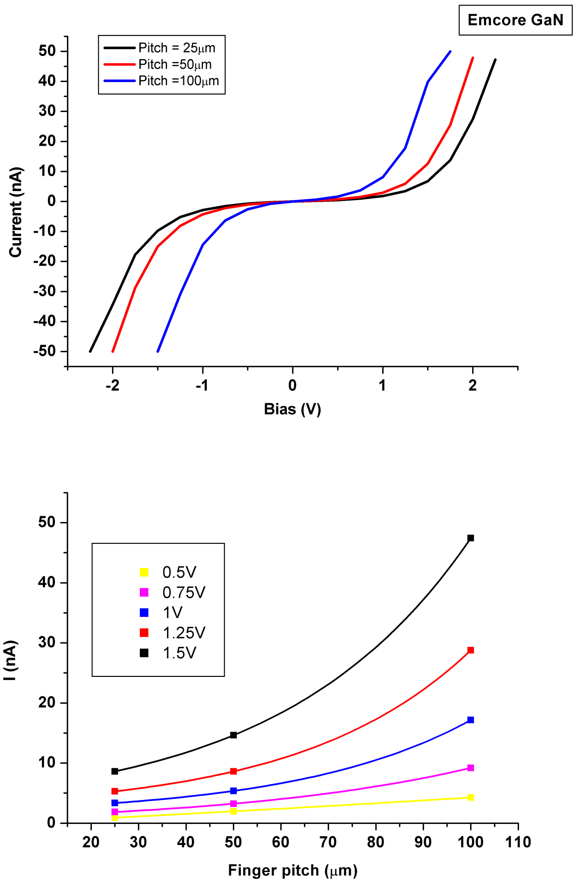

Figure 6.13: (top) - I-V characteristics for MSM GaN diodes; (bottom) - Effect of varying finger pitch on the I-V characteristics of MSM GaN diodes

- The smaller the finger pitch, the smaller the leakage current
- A larger variation of applied bias is allowed for a smaller finger pitch if the device is limited by leakage current

6.3.2 Variation of Operating Temperature

For silicon, the leakage current of a detector can be halved by decreasing the operating temperature by $\sim 7^oC$. This is because for a perfect intrinsic semiconductor the carrier concentration, n_i, is given by

$$n_i \propto T^2 \exp(-E_g/2kT) \tag{6.1}$$

where E_g is the bandgap and k is Boltzmann's constant. As GaN is extrinsic, experimentally there may be a less strong dependance of leakage curent with temperature. Using the TSC setup described in chapter 5, I-V characteristics were performed at 100, 200 and 300 K for various GaN materials.

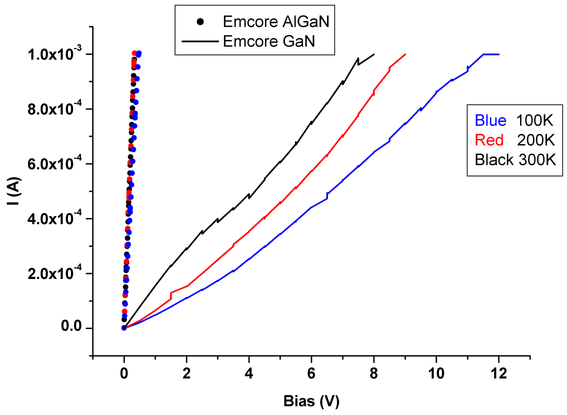

Figure 6.14: I-V characteristics for Emcore AlGaN & GaN taken at various temperatures

Emcore Material

Fig 6.14 shows the I-V characteristics for Emcore GaN & AlGaN at different temperatures. It can be seen that lowering the temperature does have an effect on the leakage current of the GaN samples, where the bias at which the compliance of 1 mA was reached was increased from 8 V to 12 V. However, the effect of lowering the temperature was negligible for the AlGaN diodes.

6.3.3 Surface Passivation

A possible cause of the high leakage current in the AlGaN material was surface states introduced through defects such as dangling bonds [24]. One way to suppress such effects is to passivate the surface of the material. For Si, passivation is most commonly achieved using Si_3N_4 or SiO_2. Si_3N_4 was then deposited on Emcore AlGaN material to assess any reduction in leakage current. Fig 6.15 shows that the use of Si_3N_4 passivation made no difference to levels of leakage current, and so would not be a beneficial fabrication step

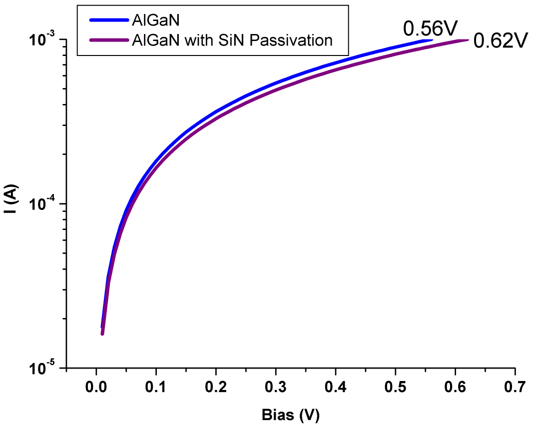

Figure 6.15: Effect of Si_3N_4 passivation on the I-V characteristics of Emcore AlGaN

Metal Recipes	ϕ_M (eV)	ϕ_B GaN (eV)
Ti/Ni/Al/Au	4.33	0.22
Au	5.1	1
Pd/Au	5.12	1.02
Ni/Au	5.15	1.05

Table 6.1: Work Functions and associated Schottky barrier heights for various metal contact schemes on GaN

for such diodes.

6.3.4 Schottky Metals

The influence of various metals on the Schottky barrier was investigated. The metals used for Schottky contacts were Pd, Au, Ni and Ti. The work functions and associated barrier heights of the metals on AlGaN & GaN can be seen in Table 6.1. Fig 6.16 shows I-V characteristics for Ti and Ni contacts on AlGaN, and Pd and Au contacts on GaN. The effect of using Au and Pd

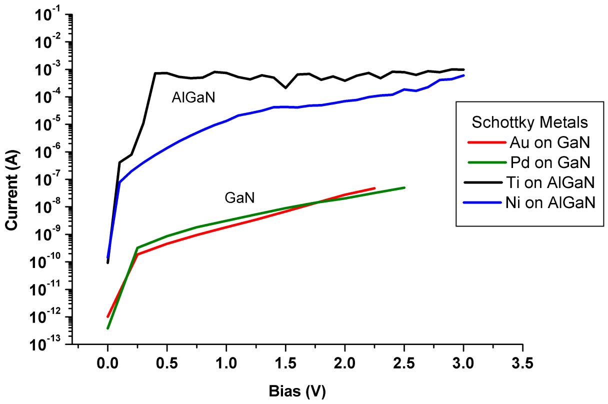

Figure 6.16: Effect of varying Schottky metals on the I-V characteristics of Emcore (Al)GaN

Schottky contacts can be seen in more detail in Fig 6.17. As Pd and Au are very similar in work function, using Pd instead of Au does not increase levels of leakage current. Furthermore, Pd has previously been shown to be more transparent to UV light than Au [79]. This means that Pd could be used for semi-transparent contacts. In this case, a portion of incident UV radiation could be detected by areas of GaN under the fingers themselves, thereby increasing the "fill-factor" of the device without increasing the physical dimensions of the diode structure.

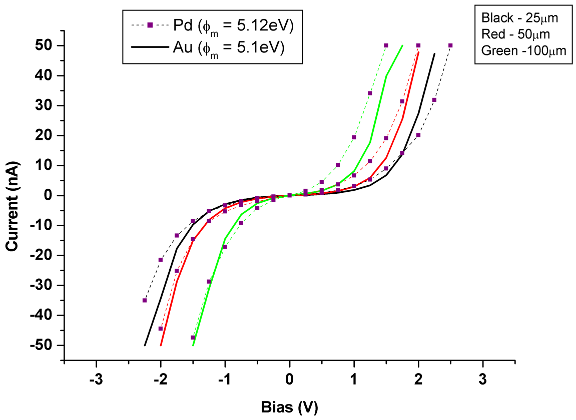

Figure 6.17: Effect of Pd and Au Schottky contacts on the I-V characteristics of Emcore GaN

6.4 UV Characterisation

The previous section described the development of the fabrication processes and electrical optimisation of the GaN detectors. An I-V characteristic was measured while the detector was illuminated by the source. Fig 6.18 shows an increase in current by 3 orders of magnitude for the unbiased sample. The following section will now describe a how a more detailed examination of spectral response was carried out using a deuterium lamp source coupled

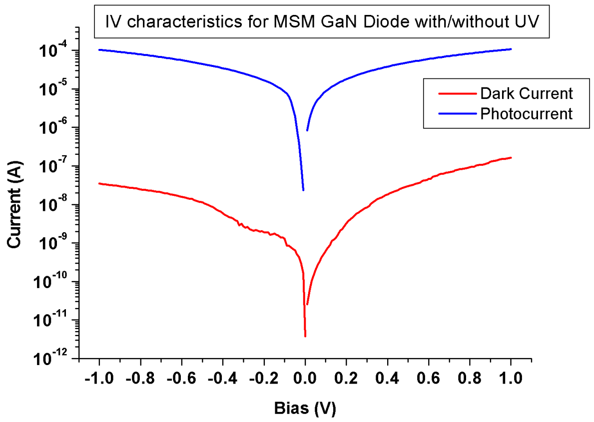

Figure 6.18: I-V characteristic for interdigitated GaN detectors with/without exposure to UV

to an automated monochromator.

6.4.1 Theory

A photodetector can be treated as an element capable of accepting an optical signal and producing an electrical signal proportional to the optical signal. When light is incident on a photodetector, a carrier is produced when the energy of the incident photon $h\nu > E_g$. Any excess energy $(h\nu - E_g)$ is dissipated as heat to the lattice. The wavelength of light which is needed to generated an intrinsic transition is defined by

$$\lambda_c = \frac{hc}{E_g} = \frac{1.24}{E_g(eV)}\ \mu m \tag{6.2}$$

The quantum efficiency of a photodetector is then defined as the number of carriers generated per incident photon. ie

$$\eta = \frac{(I_p/q)}{(P_{opt}/h\nu)} \tag{6.3}$$

where I_p is the generated photocurrent, P_{opt} is the optical power of the light source and $h\nu$ is the energy of the absorbed photon. Another important parameter concerning photodetectors is the responsivity, which is a ratio of photocurrent to optical power.

$$\Re = \frac{I_p}{P_{opt}} = \frac{\eta q}{h\nu} = \frac{\eta\lambda(\mu m)}{1.24}\ AW^{-1} \tag{6.4}$$

6.4.2 Experimental Setup

A schematic diagram of the experimental set-up is shown in Fig 6.19. A deuterium lamp was used as the UV source (λ_{out}= 180-400 nm). The monochromator was controlled by software on the PC. Using this software, the incident light could be scanned in wavelength across the spectrum of the lamp, and the photoresponse measured. Read-out electronics amplified the photoresponse signal. The amplified signal was passed to a 10 bit Analogue to Digital Converter (ADC), converting the output voltage signal into bins of fixed width. Each bin represents a voltage interval. The number of counts per bin ver-

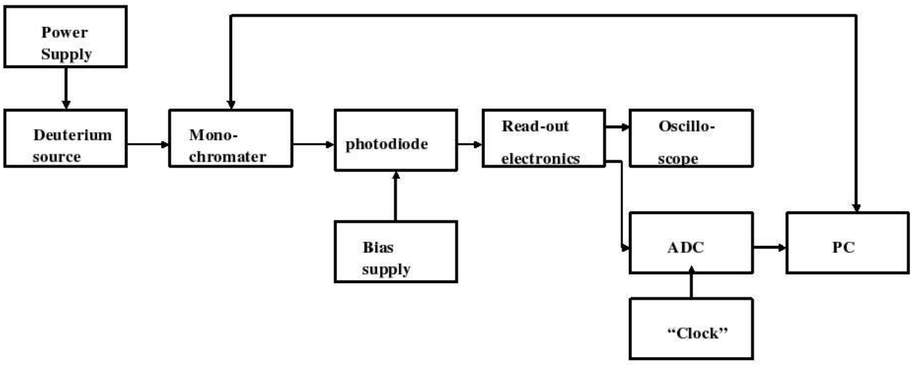

Figure 6.19: Experimental setup for photoresponse measurement

sus wavelength was displayed using software on the PC and displayed on an oscilloscope. For the spectral response measurements, scans were performed from 180 nm to 450 nm with 1 nm increments. The photogenerated current I_p is given by:

$$I_p = \frac{V_{out}}{G * R_f} \tag{6.5}$$

where V_{out} is the output voltage of the photodetector, R_f is the value of the feedback resistor and G is the gain. A Hamamatsu UV power meter was used to find the optical power output, P_{opt}, of the deuterium lamp in the range from 180 nm to 300 nm (Fig 6.20). The set-up was calibrated using a Hamamatsu silicon photodiode. An AlGaN photodetector which was also characterised allowed a comparison of the responsivity and quantum efficiency.

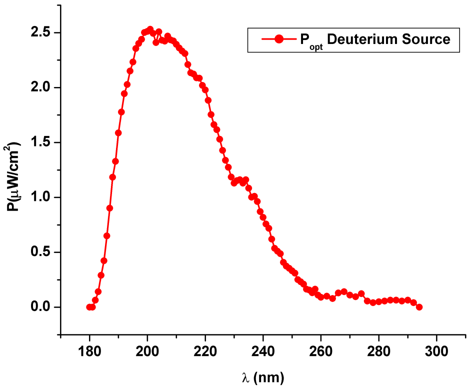

Figure 6.20: Output power of the deuterium Lamp

6.4.3 UV Response Measurements

The 25 and 100 μm interdigitated GaN detectors were connected in series with the trans-impedance amplifier with a 32 MΩ feedback resistor, designed

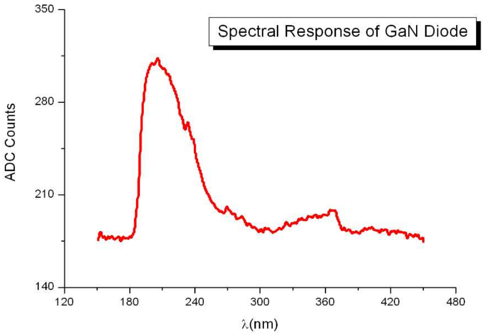

Figure 6.21: Spectral response for the 100μm GaN photodiode

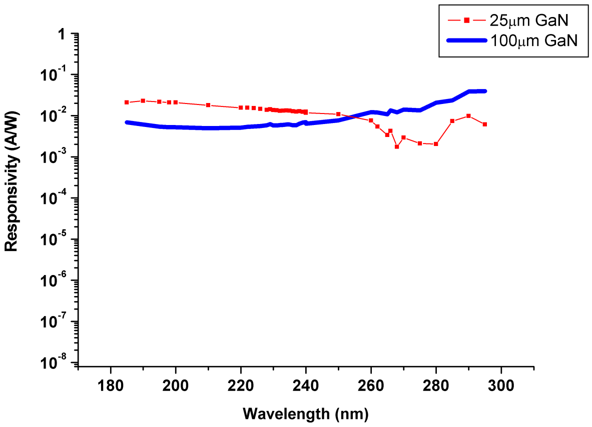

Figure 6.22: Responsivity measurements for 25 μm and 100 μm interleaving finger diodes (operated unbiased)

and built at RAL [80]. The detectors were operated unbiased. The spectral response of the 100 μm MSM GaN diode can be seen in Fig 6.21. The responsivity of these detectors (Fig 6.22) is relatively flat over the bandgap at $\sim 30\ mAW^{-1}$. The detectors show a response in the $\sim$ 190 nm wavelength region, essential for use in synchrotron applications. The low quantum efficiency (Fig 6.23) is thought to be caused by a combination of trapping [81] and the short diffusion length of minority carriers [82]. These measurements are in agreement with the simulation carried out by Monroy et al [83], where

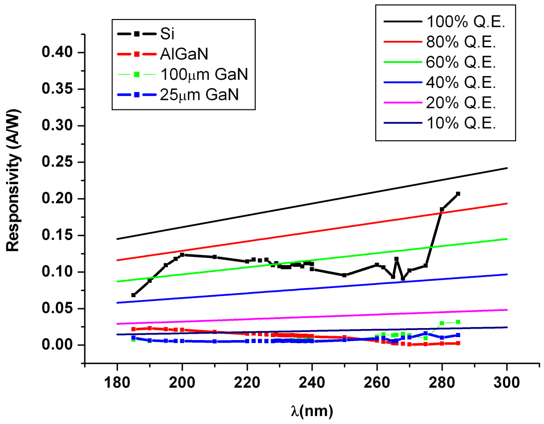

Figure 6.23: Relative quantum efficiencies for the 4 tested detectors

it is proposed that the quantum efficiency of interdigitated diodes is strongly influenced by the finger pitch. The next section will now describe a novel use for such interdigitated MSM GaN diodes - the study of protein folding

6.5 UV detectors for Proteomics

Proteomics is the study of the full expression of proteins by cells in their lifetime. Proteins are chains of amino acids. For amino acids to form a protein the extended chain of amino acids must "fold" into a compact globular object with exactly the right shape. It is important to know more about the dynamic and folded structures as this offers an insight to diseases such as Alzheimer's disease and cystic fibrosis, caused by mis-folding of proteins. One method of measuring the folding of proteins is possible through measurements of Circular Dichroism, as detailed in the next section.

6.5.1 Circular Dichroism

CD (fig 6.24) is the measurement of the difference in absorption between left and right circularly polarised light as it passes through an optically active medium. It is known that each secondary structure of a protein has its own characteristic CD spectrum. To study how a protein folds into its specific compact structure, CD measurements must be performed below 260nm.

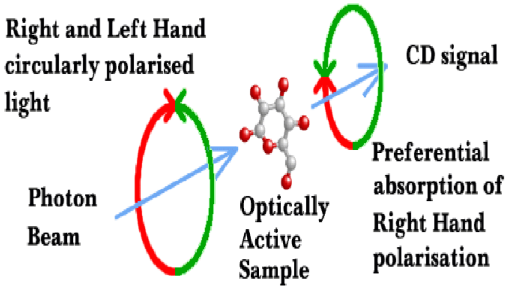

Figure 6.24: A schematic representation of Circular Dichroism

6.5.2 Synchrotrons for UV

The need to make measurements where the samples absorb strongly below 200nm gives rise to the need to use synchrotron machines as sources of intense light, utilising a range of UV not easily accessible using conventional CD instrumentation (Fig 6.25). A CD experiment is therefore to be performed at the Daresbury synchrotron radiation source (SRS) [72], utilising the higher intensity and range of electromagnetic radiation in the hard UV range offered by a synchrotron source ($<\sim$160 nm) [84]. Fig 6.26 shows an example of the characteristic CD spectra for various secondary structure states. The additional range of wavelength, and thus signal when using a synchrotron radiation source source can also be seen. As well as poor light sources,

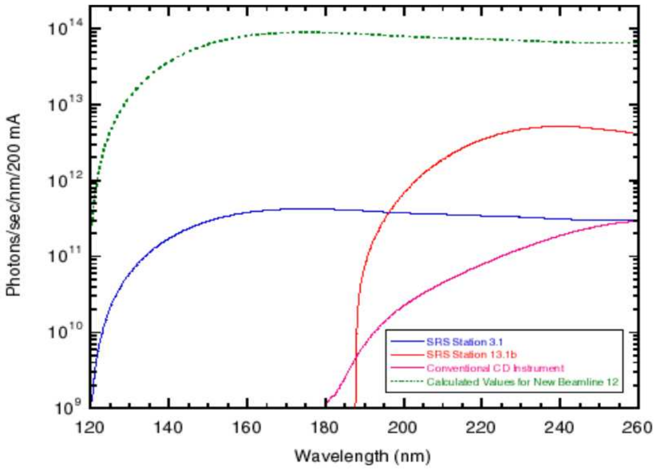

Figure 6.25: Comparative intensities of UV light from conventional CD instrumentation and a synchrotron radiation source

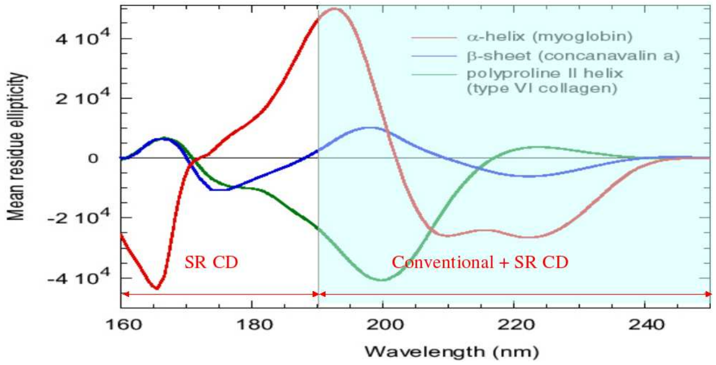

Figure 6.26: Spectral range possible using SR

CD measurements suffer from the length of time as well as the relatively large amounts of material needed for a complete measurement. In order to minimise the impact of these types of difficulties, a 46-channel array of UV diodes was proposed to measure the wavelengths 160-260 nm simultaneously through the use of a diffraction grating (Fig 6.27).

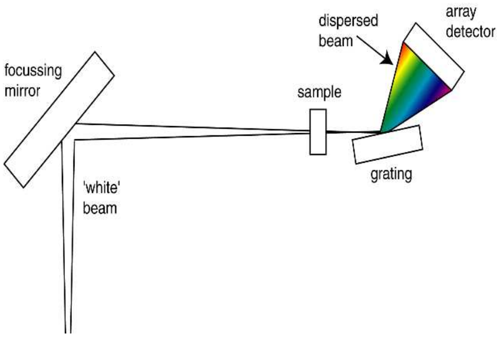

Figure 6.27: Energy dispersive grating for simultaneous CD measurements

6.5.3 Designs for GaN UV Detectors for Synchrotron Radiation Sources

A novel design was developed for the use of AlGaN as a position sensitive UV detector - a structure that would be ideal for energy dispersive measurements. Instead of using a single inter-digitated electrode structure for the diode, it utilises 46 diodes linked by a common ground. Each diode is then wire-bonded to a custom pcb, designed to fit into a commercially available DIP socket for connection to read-out electronics. This gives flexibility in the instrument's design by providing modularity and allowing for the independent development of detector and read-out electronics. The design for the pcb used is shown in Fig 6.28.

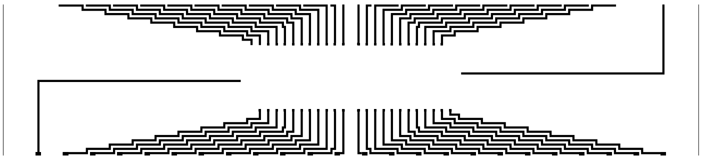

Figure 6.28: Schematic of the PCB for the 46 channel UV detector array on AlGaN

The initial design can be seen in Fig 6.29. To meet the requirement for minimal dead area, the 46 channels (23 on each side) are spaced evenly over the length of the array. In this example, both the pitch and width of the fingers was 50 μm.

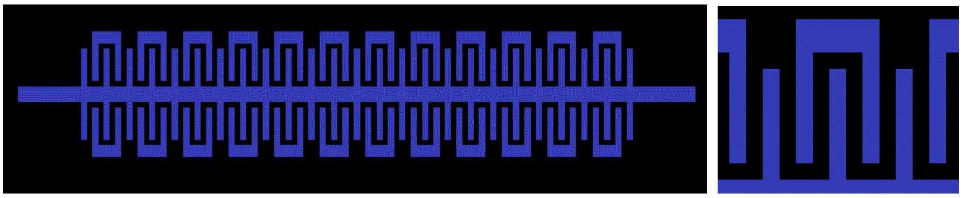

Figure 6.29: Initial design for 46 channel UV detector array on AlGaN

However, as seen from earlier work, the relative QE of an MSM detector is greatly reduced unless the finger pitch <10 μm. Such a parameter in the above design would either have the diodes bunched together, creating problems for the pcb read-out chip, or the diodes would be separated over large areas, inducing large dead areas. The design should consist of finger diodes with finger spacings of $\sim$ 10 μm and a regular separation. These parameters were incorporated in the final design detailed in Fig 6.30.

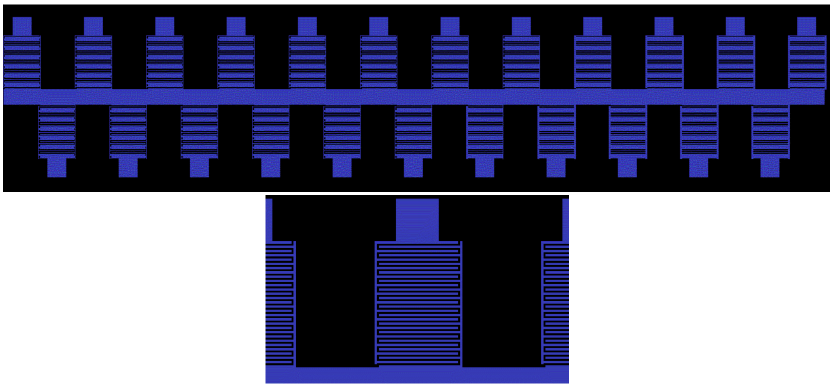

Figure 6.30: Completed design for 46 channel UV detector array on AlGaN

This design separates the crucial parameter of finger pitch from the spacing requirements. The number of diodes can be increased or decreased without affecting the finger pitch and thus the theoretical upper limit of QE of the detector. Moreover, the finger pitch can be reduced below 10 μm.

6.6 Summary & Future Work

The work in this chapter has detailed the development of fabrication processes in both photolithography and e-beam lithography for the production of MSM UV detectors on (Al) GaN. A practical process now exists for production of interdigitated MSM Diodes on GaN, with finger pitches < 5 μm. The fabrication process incorporates techniques such as using bi-layers of resist and chlorobenzene soaks for lift-off enhancement. Successfully fabricated detectors have been optimised for the metal contact shemes used for Schottky contacts, allowing for the possibility to use Pd contacts for semi-transparent contacts. Experiments showed that the leakage current could be reduced by decreasing the finger pitch of interdigitated MSM diodes.

A ratio of 10^3:1 is seen for levels of photocurrent against dark current. Full UV characterisation of the diodes shows good performance in the 190 nm region when unbiased, with the responsivity relatively flat over the bandgap. Although the level of responsivity is low, unlike UV silicon, there is still no need for filters for the visible range. Also unlike diamond (where the cut-off wavelength is $\sim$225 nm), all wavelengths under 365 nm are detectable. Using these results, a 46 channel diode array on GaN has been designed for use in CD measurements to be performed at the Daresbury Synchrotron Radiation Source. The dimensions were chosen so that the diode can be easily wire bonded to a commercially available DIP socket The finished design allows

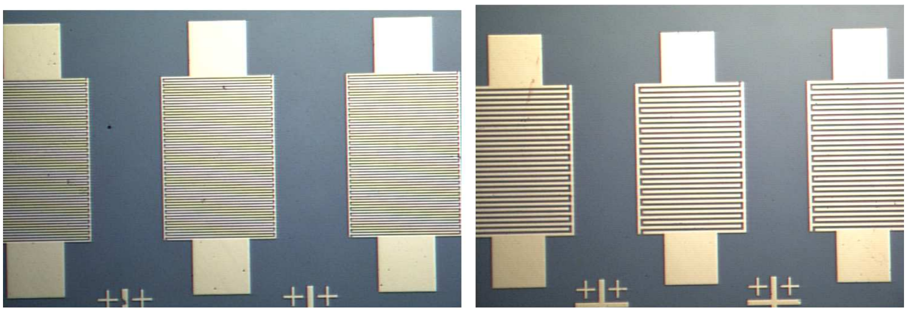

Figure 6.31: Example of fabricated 5μm and 10μm MSM diodes on GaN

the diodes to be separated by distances of millimetres, whilst the detectable quantum efficiency will be determined by the pitch of the fingers. Semi-transparent contacts are to be made using Pd metal to optimise the active area. The detector can also be operated unbiased. To test if the QE improves with a reduced finger pitch, a set of test arrays with both 5 μm and 10 μm fingers have been fabricated (Fig 6.31) and await characterisation.

Chapter 7

ICP etching

7.1 Introduction

This section will report on a study of the development of a dry etch process of silicon using a Surface Technology Systems (STS) inductively coupled plasma (ICP) machine [20]. The effect of varying the hole diameter on the etch rate of vias in silicon is shown, as well as the use of "parameter ramping" to increase the performance of the etch for deep holes. Results for proton irradiated silicon 3D detectors fabricated using the modified etch recipe are shown. A recipe was developed for etching vias $>$50 μm deep, allowing for the fabrication of a shadow mask for the realisation of metal contacts. Finally, preliminary results for ICP etching of GaAs using a non-carbon based chemistry are shown.

7.2 Etch Rate Tests

To fabricate successfully micromachined devices such as 3D detectors, it is important to calculate the (diameter dependent) etch rate of holes. For this, a photolithographic mask was fabricated using e-beam lithographic techniques. The mask consisted of arrays of circles with 10, 20, and 30 μm diameters.

4" diameter, 330 μm thick Si wafers were scribed into quarters and solvent cleaned (as described in chapter 2). After spinning on HMDS, AZ4562 photoresist was applied using a syringe. AZ4562 is a relatively high viscosity resist compared to classical resists used in thin-film lithography, such as S1818, resulting in a thicker layer of resist. However, spinning this resist at the standard speed (4000 rpm) produces a layer of just 6.2μm. In order to increase the thickness of the layer, the spin speed was reduced to 1500 rpm, producing in a resist layer of ~15 μm thickness. The increased thickness of the layer is necessary to ensure the mask survives for the duration of the etch. The sample was baked for 30 minutes at 90^{o}C to remove all solvents in the photoresist. The samples were exposed on a MA6 mask aligner for 30 seconds. The samples were developed for 4 minutes in a solution of 1:4 AZ 400K developer. A post-bake of 15 minutes was done at 90^{o}C. Starting from an etch duration of 40mins, the samples were etched with 20 min increments with an STS ICP machine using an optimised recipe (shown in Table 7.1). After etching, the samples were then cleaned, cut either side of the arrays using a wafer scriber, and cleaved. The depth of the holes was measured using a scanning electron microscope. Fig 7.1 shows samples of the holes as viewed with the SEM, while Fig 7.2 shows the etch hole depth for varying

Step	Etch	Passivation
Gas	SF_6/O_2	C_4F_8
Flow Rate (sccm)	130/10	85
Time (s)	13	7.5
Platen Power (W)	15	15
Coil Power (W)	600	600

Table 7.1: Etch chemistry used for holes $< 30\mu$m diameter

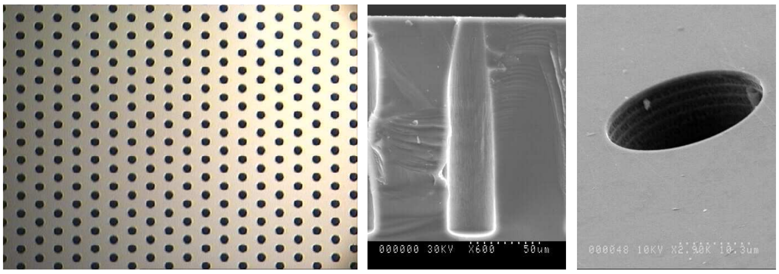

Figure 7.1: Examples of ICP etched silicon using an ASE^{TM} process at Glasgow

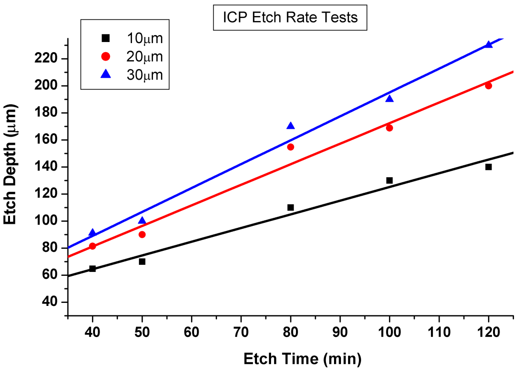

Figure 7.2: Etch rates for varying diameters of holes using an ICP system

nominal hole diameters over a range of etch times. The graph shows that there is a lower etch rate for smaller features. This is primarily due to the finite distance the etchant ions can travel down the holes. This eventually puts a limit on the depth of these features for a decreasing diameter of holes. At this point, etch damage from physical sputtering can dominate, and the holes are often seen to widen at the top, creating a conical-shaped feature. The best aspect ratio (depth/diameter) achieved was 14:1 for 10μm holes. In parallel, prepared silicon samples were etched using STS's R&D section at

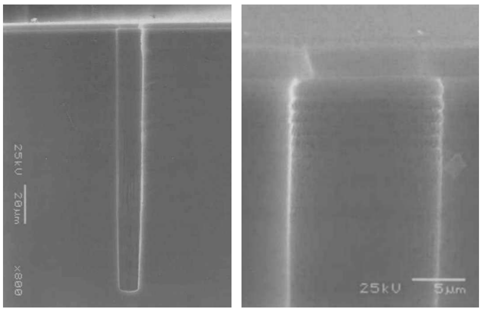

Figure 7.3: Examples of ICP etched silicon using an ASE^{TM} process at STS

their Newport plant. STS used an optimised modification of the recipe used at Glasgow. SEM's of the etched samples are shown in Fig 7.3. Etch depths for 10μm diameter holes of up to 170μm (aspect ratios of 17:1) produced by STS have been achieved.

7.2.1 Parameter Ramping

For the etching of very high aspect ratio features, it is frequently necessary to make alterations to the etch parameters as the process continues. This arises from the fact that the parameter settings needed for a vertical profile at the start of the etch are different from those at the end when the aspect ratio is high. By altering - or ramping - the following parameters, we can increase the maximum achievable aspect ratios without sacrificing features such as sidewall smoothness and verticality.

Process pressure

In general terms, the deeper the hole, the fewer the etchant species present at the bottom. Increasing the process pressure results in a higher etch rate mainly due to increasing the number of fluorine radicals present in the hole. Unfortunately, this can lead to poor profile control in the case of high aspect ratio features. Because of the increased isotropy of the etch, bowing and closing up of features can occur. This is mainly due to the increased scattering of ions at higher pressures, increasing the tendency to etch laterally. Feature control can be improved by reducing the process pressure, but with this comes an increase in mask etch rate, and so a reduction in process selectivity as a consequence of the increased ion energy.

Platen power

For high aspect ratio features, applying a high platen power can avoid the closing up of trenches towards the bottom of the features. A higher platen power can also help remove the passivation layer at the base of the features but this may lead to an increase in the mask erosion rate, resulting in a reduction in selectivity.

Parameter Ramping Etch Tests

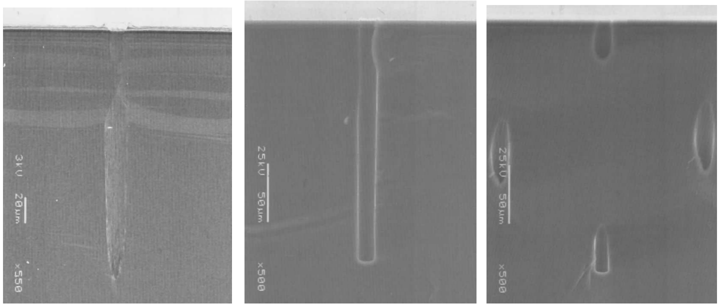

Figure 7.4: 10 μm holes - (left) start, (middle) finish and (right) ramped parameters

Samples with 10, 20 and 30 μm holes were sent to STS for etching in an ICP which had ramping software installed. To compare the etches with and without ramping, three 100 minute runs were etched: one at the starting

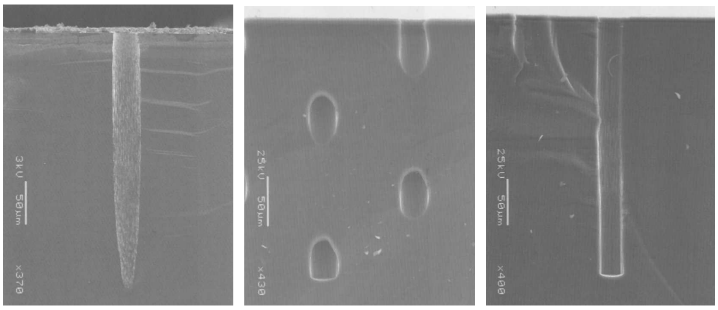

Figure 7.5: 20 μm holes - (left) start, (middle) finish and (right) ramped parameters

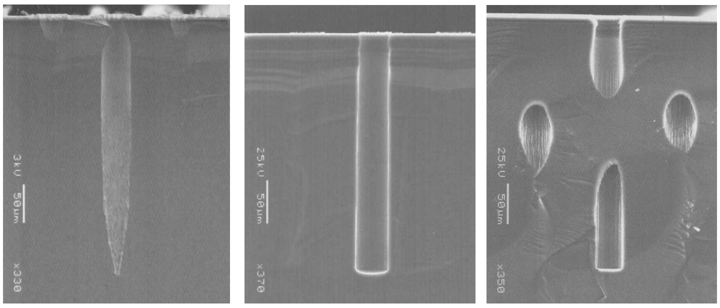

Figure 7.6: 30 μm holes - (left) start, (middle) finish and (right) ramped parameters

conditions, a second at the finishing conditions, and a third ramping between the start and finishing conditions (where the pressure was reduced and the platen power increased through the course of the etch). The details from each run are listed in Table 7.3. SEM pictures of the finished etches for each run can be seen in Figs 7.4, 7.5 & 7.6. The results show that with low platen power and high pressure, selectivity is high but the holes tend to close up. This closing of the holes limits the achievable depth. With high platen power and low pressure the holes are vertical with no indication at this depth of closing up, but the selectivity is poor and so the hole depths are limited by the mask thickness. By ramping the platen power up and the pressure down vertical holes can be etched with reasonable selectivity and a favourable compromise is reached. Aspect ratios of ~20:1 for 10 μm holes were achieved, providing an additional depth of 30 μm over conventional ASE^{TM} techniques.

Recipe	Start			Ramped			Finish		
Mask ER (nm/min)	11			18			63		
Hole Diameter (μm)	10	20	30	10	20	30	10	20	30
ER (μm/min)	1.9	2.7	3.3	2	2.7	3	2	2.5	2.7
Profile (^{o})	89.5	89.5	90.6	89.4	89.8	89.7	89.9	90.1	90.1

Table 7.2: Details of the ICP etching of Si using parameter ramping

This section has shown how it is possible to create features with small diameters and large aspect ratios. The ability to fabricate such features in silicon has been utilised for several applications. These include microfluidic devices (an example of which is shown in section 7.4), gaseous electron multipliers (GEMs) and particle detectors implementing a 3D topology. Using such a geometry has major possible advantages over traditional planar detectors fabricated from silicon. The theory, fabrication and characterisation of such detectors will now be shown in the following section.

7.3 3D Detectors

In order to counteract the need for high bias voltages for high charge collection efficiency in radiation damaged planar silicon radiation detectors, geometries exploiting 3D structures etched deep into the bulk of a material have been proposed [85]. The planar contacts to the front and back are replaced by cylindrical electrodes running through the bulk of the material (Fig 7.7). The electrodes can be arranged in a hexagonal closed packed geome-

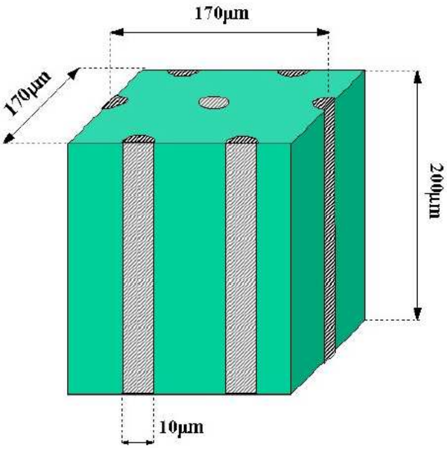

Figure 7.7: The geometry of a 3D detector [30]

try, giving a more uniform electric field between the central and surrounding electodes. The e-h pairs created by an incoming particle are accelerated in a direction parallel to the wafers surface, towards the nearest electrodes.

The topology of 3D detectors means the depletion depth needs to extend only as far as the distance between each pair of oppositely biased electrodes. For example, if the distance between pairs of electrodes is 25 μm, the depletion voltage would be ~1-5 V, in contrast to a standard 300 μm thick silicon pixel detector, where depletion occurs at ~50-70 V. 3D detectors may also offer improved radiation tolerance of detectors. The short collection times achievable due to the close approximity of the electrodes may mean created e-h pairs might not be trapped by radiation induced defects, as the collection time is shorter than the trapping time of this material in this configuration.

Another advantage is that the lateral depletion length is equal to half the distance of the pixel pitch, no matter which thickness of detector. This is plainly not the case for standard planar detectors, where the depletion depth is the thickness of the detector. This means that the lateral dead area of the

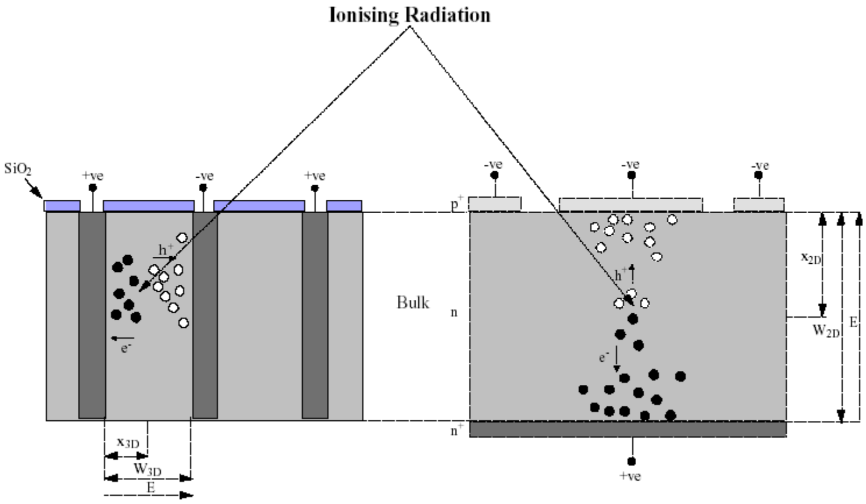

Figure 7.8: Cross-section of charge collection in (left) standard planar and (right) 3D detectors [30]

detectors is minimised, as the active area can be close to the cut edges of the detector. Another advantage of the 3D topology is that the active volume can be increased without increasing the operating voltage. This is achieved by increasing the thickness of the material used for the detector. This technology could be used to increase the effective stopping power of materials and make them useful for energy ranges previously considered unpractical for X-ray detection.

As stated in chapter 4, along with investigation of new materials, research has begun into alternative detector geometries for a possible improvement in radiation hardness. Such examples are edgeless [86] and thinned detectors [87]. The following section will now describe some of the work carried out on investigating 3D detectors for radiation hardness.

7.3.1 3D Schottky Si Detectors

Schottky contact 3D silicon detectors were fabricated by Patrick Roy and Giulio Pellegrini using holes drilled with an ICP recipe optimised for 10 μm holes [30]. Holes were etched using an ICP to a depth of 130 μm, with a diameter and pitch of 10 and 85 μm, respectively. Schottky metal contacts were formed using 50 nm Ti and 100 nm Au. 150nm Al interconnecting tracks (15 μm wide) were realised on the wafer surface (Fig 7.9). The devices were irradiated with the proton range listed in Table 7.3. The proton irradiations were carried out at CERN in the facility described in chapter 4.

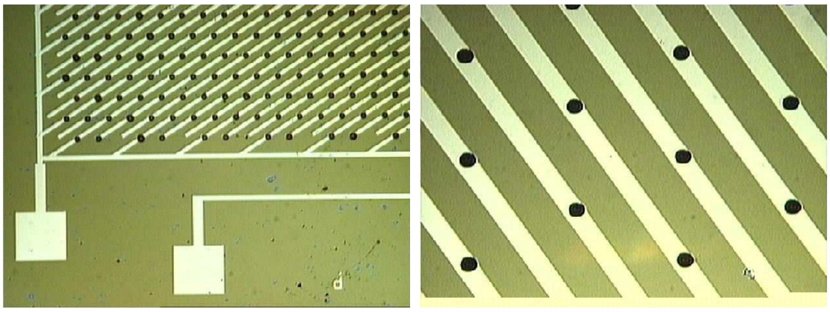

Figure 7.9: Geometry of holes and contacts on 3D Schottky Si detectors

Sample	Fluence ($\times 10^{13} pcm^{-2}$)
1	1.06
2	8.11
3	45.2

Table 7.3: Range of proton fluences used to irradiate Schottky 3D silicon detectors

7.3.2 Results

Fig 7.10 shows the I-V characterstics that were obtained from the irradiated diodes. Using the I-V characteristics, the linear dependence between

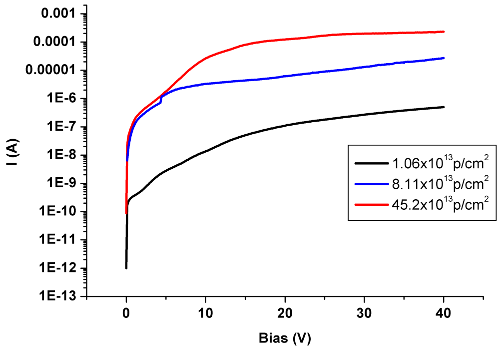

Figure 7.10: Current-Voltage characteristics for proton irradiated 3D Schottky Si detectors

increased leakage current and irradiating fluence, α [as defined in chapter 4] was used to calculate the damage coefficient α to be 1.62×10^{-7} $nAcm^{-1}$ (Fig 7.11). CCE measurements were carried out (according to the method used

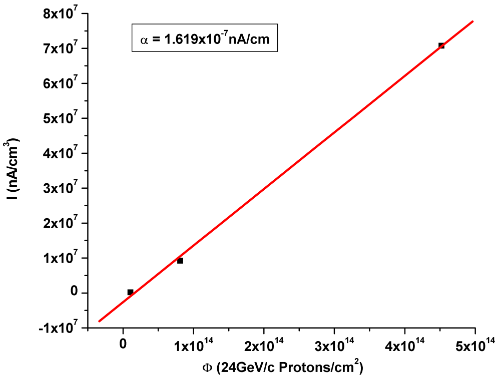

Figure 7.11: The linear increase of leakage current with proton fluence

in chapter 4) using an Am^{241} α source. The maximum achievable CCE was calculated to be ∼60% for the unirradiated detectors. The CCE was then seen to fall to $\sim$ 5% after 4.52×10^{14}p/cm^{2} (Fig 7.12).

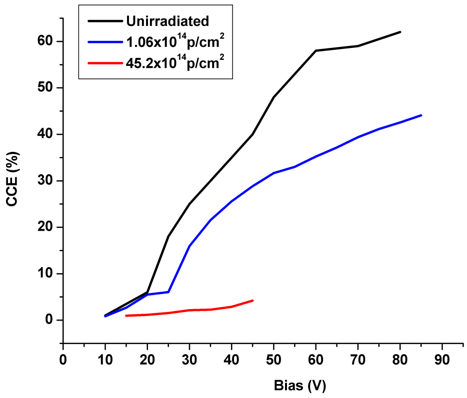

Figure 7.12: CCE levels for proton irradiated 3D Schottky Si detectors

The poor performance of the CCE levels after irradiation [85] [88] may be due to a variety of reasons. These include the possible inhomogeneities in the Schottky metal / hole sidewall interface or the generally poor performance of Schottky contacts on silicon due to the low barrier height. The samples were also held at -5^{o}C for a sustained period of time, and although annealing should not have taken place, some detrimental effect may have occurred. 3D p-n detectors utilising doped holes (a configuration which has proved successful in other work [89]) are to be fabricated for comparative testing.

7.4 Additional ICP Etching Techniques

So far, this chapter has discussed the optimisation of an ICP system and its use for the fabrication of 3D detectors from silicon. However, such technology can be used for a wider range of applications. This section will now describe the work carried out on some of these, including the use of a through-etched silicon wafer for metal masks and for the fabrication of a microfluidic mixing device. Additionally, results are shown for the etching of small diameter holes (10 μm) in GaAs using an STS ICP machine.

7.4.1 Silicon Devices

One possible application of through-etched silicon wafers is in the field of shadow masks for the realisation of metal contacts. Prof. Mohan Lal from Indian Imperial University required a through etched silicon wafer for metal deposition for solar cells on Kapton. The design featured fingers with a width and length of 650 and 18000 μm respectively, with 325 μm spacings. To optimise the etch recipe for fabrication of features >50 μm, a test structure mask was processed with various feature shapes and dimensions. Variations were applied to the platen power and deposition time. An example using the resultant optimised etch is shown in Fig 7.13, with the parameters of the recipe detailed in Table 7.4. Fig 7.13 also shows the finished shadow mask. The wafer was subsequently fabricated and etched as in section 7.2.1. The etch time was increased to 120 minutes. A further example of the use of the optimised recipe described is shown in Fig 7.14 & 7.15, illustrating sections of a silicon etched microfluidic mixing device.

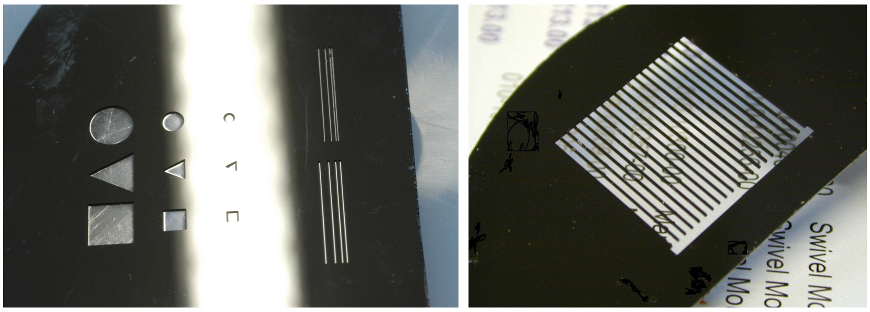

Figure 7.13: Pictures of (left) - a test structure with varying through-etch dimensions; (right) - a shadow mask for metal contact realisation

	Etch	Passivation
Gas	SF_6	C_4F_8
RF (W)	600	600
Platen (W)	12	12
Time (s)	13	7
Flow Rate (sccm)	130	85
Platen Temp(K)	293	293

Table 7.4: ICP Etch recipe for Si with features $>50\mu$m

This device had 50 μm deep channel features. The gap between the channel and chamber is 5 μm wide. The high quality of the etch is evident in the sidewall formation, where the polygonal nature of the circles defined by the CAD program WAM is visible on the circular chamber after etching.

7.4.2 ICP etching of GaAs

While a significant body of work has been published on the etching of silicon using a switched process, this is not the case for GaAs. Instead of using SF_6 and C_4F_8, Cl_2-based gases and a mixture of CH_4 and $SiCl_4$ are used for the etch and passivation chemistries, respectively. For the case of carbon based chemistries, the contamination in the chamber is a major detrimental factor: carbon build up in the chamber walls can lead to flakes falling on the sample, ruining the etch. Hitherto no results have produced evidence of a switched process (eg scalloping) or of aspect ratios greater than 3:1 [90] using non carbon based chemistries. Work was carried out using STS R&D facilities into alternative chemistries for the etching of GaAs.

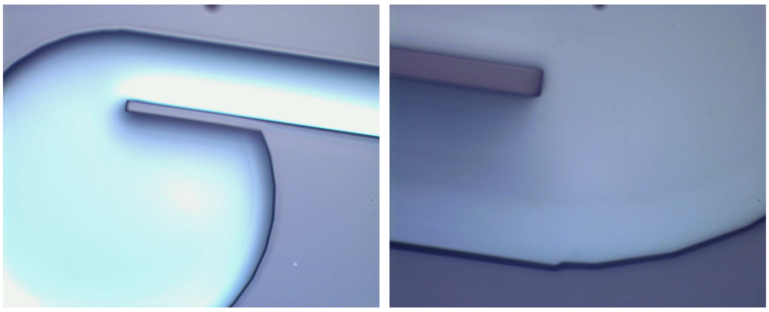

Figure 7.14: Pictures of the Etched Micromixer; (left) - chamber and channel, (right) - chamber in more detail

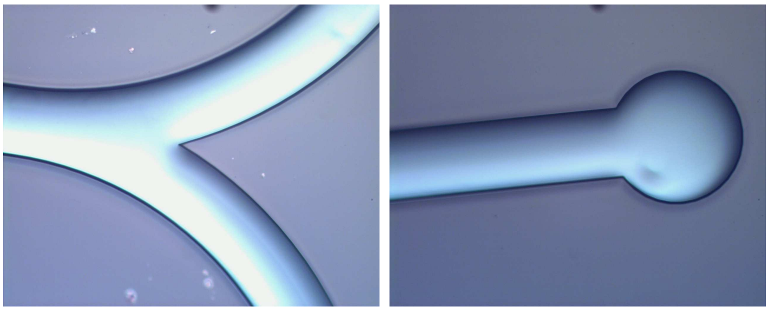

Figure 7.15: Pictures of the Etched Micromixer; (left) - merging of input and output channels section, (right) - output chamber

Results

A set of GaAs samples with arrays of 10 μm holes were fabricated as described in section 7.2.1. Plastic tweezers were used for handling the GaAs wafers to inhibit the introduction of microcracks into the material. An initial sample was etched with a starting recipe, using Cl_2 as the etch gas and BCl_3 and O_2 in the deposition step. An adjustment was made to one parameter at a time. The modifications to the recipe are shown in table 7.5, with results of the changes in the etch properties shown in Fig 7.15.

A significant improvement can be seen from the starting to the finishing etch. The striations evident in picture 4 and 5 were caused by the failure

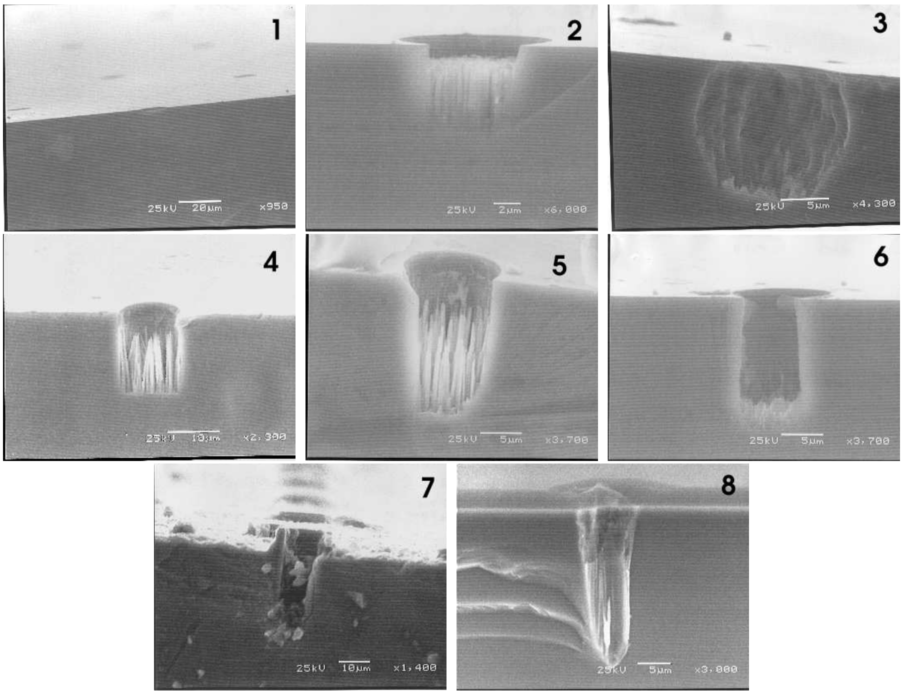

Figure 7.16: Examples of the improvement in etch quality and rate for ICP processed GaAs

to remove fully the passivating layer from the bottom of the holes. The isotropic - or strawberry - etch (3) was caused by not enough passivation on the side wall. The final picture (8) shows a hole with the first oberved example of scalloping (showing evidence of a switched process) in GaAs using a non-carbon-based chemistry. Aspect ratios of 4.5:1 were achieved.

7.5 Summary & Future Work

In this chapter, a relationship between hole diameter and etch rate has been successfully established, allowing greater control over etch depths. An upper limit aspect ratio for 10 μm holes of 14:1 was achieved using the ASE^{TM} process in an STS ICP. An improved aspect ratio of 17:1 was achieved us-

Step	Comment
1	Starting Conditions
2	Add BCL_3 to the etch step
3	Reduce pass time
4	Increase etch time
5	Increase process time
6	Reduce platen power on pass step
7	Increase etch time
8	Increase process time

Table 7.5: Optimisation of GaAs ICP etch recipe

ing STS's own R&D ICP machine. Varying the platen power and pressure throughout the course of an etch has shown the advantages of utilising parameter ramping to increase the performance of the etch. Using the optimised recipes, fabricated 3D silicon detectors were tested after proton irradiations for their radiation hard properties. The CCE was found to drop significantly after irradiation (from 60 to 5% after $5\times10^{14}\text{p}cm^{-2}$), although this is thought to be due to the inhomogeneities in the Schottky metal / hole sidewall interface. 3D p-n silicon detectors are currently being fabricated for comparative testing. The recipe has been modified for etching of vias $>$50 μm. This allowed the fabrication of a shadow mask for the realisation of metal contacts. The recipe was also demonstrated to be of use in fabricating microfluidic devices. Improvements in the ICP etching of GaAs using a non-carbon based chemistry were shown to be possible. The ability to create such vias in GaAs opens the possibility for improved X-ray detection using 3D GaAs detectors. However, the aspect ratio and achievable etch depth need to be much improved in order for this to become attractive. Similar process development is also under investigation using the photochemical etching of GaAs for such purposes.

Chapter 8

Conclusions

8.1 Conclusions

In this thesis, a range of GaN samples tested were shown to possess good electrical properties, ensuring its effectiveness as a detection material. The low leakage currents measured allow detectors to operate with low noise levels at high biases. A drop of 18% in CCE is measured after Tokushima grown material is irradiated with a fluence of 10^{14}ncm^{-2}. Although this drop is significant, the diode requires no increase in operating voltage. The diodes were also tested pre- and post-irradiation at room temperature. Stabilising both the operating bias and temperature is beneficial when considering the power necessary for continuous operation of a detector. The tested irradiated detectors, however, showed a rapid decrease in CCE values for very high hadronic fluences (10^{16}particles cm^{-2}).

Within this work photoluminescence spectroscopy, microwave absorption, photoconductivity and thermally stimulated current measurements were used to characterise defects in a wide range of GaN materials. These included Tokushima grown material irradiated with X-rays, protons and neutrons, Emcore grown GaN and AlGaN and CST grown Mg doped GaN. Investigation of the irradiated samples indicated an increase in non-radiative recombination centres. This was shown through a decrease in all PL peaks, and through the decrease in the instantaneous carrier lifetimes from MWA and PC measurements. An increase in asymptotic lifetimes suggests that excess carriers undergo a multi-trapping process after irradiation. PL measurements also indicate a rapid decrease in intensity for the YB peak, indicating a transformation of point defects into non-radiative centres. Dislocation defects appear to be unchanged with irradiation.

Photoluminescence spectra were also used to identify the molar fraction of Al present in an Emcore AlGaN wafer, which was found to be ∼10%. PL was used to show that increasing TMG flow rates in MOCVD growth can significantly increase both point and dislocation defects. The activation of Mg doped GaN was also verified using PL spectra. A common defect with activation energy of ∼0.675 eV is found for two types of Emcore GaN material using both TSC and MWA measurements. The variety of trap levels found throughout the materials is consistent with previous results, suggesting numerous material dependent defect levels in thin GaN films.

Photolithographic and e-beam lithographic fabrication techniques were developed in this work for the production of MSM UV detectors on Emcore grown (Al)GaN. A practical process now exists for production of interdigitated MSM Diodes on GaN, with finger pitches < 5 μm. The fabrication process incorporates techniques such as using bi-layers of resist and chlorobenzene soaks for lift-off enhancement. Successfully fabricated detectors have optimised metal contact schemes used for Schottky contacts, allowing for the use of Pd contacts for semi-transparent contacts. Experiments showed that the leakage current could be reduced by decreasing the finger pitch of interdigitated MSM diodes. A ratio of 10^3:1 is seen for levels of photocurrent against dark current. Full UV characterisation of the diodes showed good performance in the 190 nm region when unbiased, with the responsivity relatively flat over the bandgap. Although the level of quantum efficiency is low, unlike UV silicon, there is no need to filter out the visible range. Also unlike diamond (where the cut-off wavelength is $\sim$225 nm), all wavelengths under 365 nm are detectable.

Using fabrication processes developed in this work, a 46 channel diode array on GaN has been designed for use in CD measurements to be performed at the Daresbury Synchrotron Radiation Source. This design incorporated the first ever use of interdigitated finger diodes on GaN for position sensitive light detection. The dimensions of the finger didoes have been chosen so that the detector can be easily wire bonded to a commercially available DIP socket. The finished design allows the diodes to be separated by distances of millimetres, whilst the detectable quantum efficiency will be determined by the pitch of the fingers. The detector can also operate unbiased.

Finally in this work, an STS ICP system has been used for the creation of vias in silicon and gallium arsenide, for the production of 3D detectors. A relationship between hole diameter and etch rate has been successfully established, allowing greater control over etch depths. An upper limit of 14:1 aspect ratio for 10 μm holes was achieved using the ASE^{TM} process in an STS ICP. An improved aspect ratio of 17:1 was achieved using STS's own R&D ICP machine. Varying the platen power and pressure throughout the course of an etch has shown the advantages of utilising parameter ramping to increase the performance of the etch, where an aspect ratio of 20:1 was achieved. Using the optimised recipes, fabricated 3D silicon detectors were tested after proton irradiations for their radiation hard properties. The CCE was found to drop significantly after irradiation (from 60 to 5% after 5×10^{14}pcm^{-2}), although this is thought to be due to the inhomogeneities in the Schottky metal / hole sidewall interface. The recipe was then modified for etching of vias $>$50 μm. This enabled the fabrication of a shadow mask for the realisation of metal contacts. The recipe was used in fabricating microfluidic devices. Improvements in the ICP etching of GaAs using a non-carbon based chemistry were shown.

8.2 Future Work

To use GaN as a particle detecting material for large experiments, the yield of material must increase. GaN grown on sapphire cannot utilise many diode configurations, as contacts cannot be realised to the back of the substrate. An increase in thickness of GaN from 2 μm would also be necessary for its use as a tracking detector. Currently, investigations are about to begin using thicker GaN. This will involve the fabrication and testing of detectors made from both 25 μm thick and bulk (>250 μm) GaN.

Initial characterisation of the diode designed in this work for circular dichroism measurements is required. For this, fabricated arrays with 5 μm and 10 μm fingers are to be tested for improvement of leakage current, responsivity and quantum efficiency. Results from this work have suggested optimisation of the active area can be made using semi-transparent Pd metal contacts. Testing of the finished device should begin in Spring 2005 in conjunction with the Daresbury synchrotron radiation source and Rutherford Appleton Laboratories

The recipes developed for use with an STS ICP for the etching of silicon will form the basis of several projects. The ability to etch deep holes in silicon can now be utilised for the fabrication of gaseous electron multipliers (GEMs), microfluidic devices and p-n based 3D detectors. Such p-n junctions are now being fabricated and their radiation hard properties will be characterised again using protons and neutron irradiation and CCE degradation and increased leakage currents. The ability to create vias in GaAs has opened the possibility for the fabrication of 3D GaAs detectors. Such detectors could be used for improved X-ray detection. Similar process development is also under way into the photochemical etching of GaAs for such purposes.

Bibliography

[1] R. Juza, H. Hahn, Z. Anorg, Angg. Chem. 234 (1938) p 248

[2] H.P. Maruska, J.J. Tietjen, Apl. Phys. Lett. 185 (1967) p 327

[3] M.A. Kahn, R.A. Skogman, J.M. Van Hoe, Apl. Phys. Lett. 56 (1990) p 1257

[4] Y. Koide, H. Itoh, M.R. Khan, K. Hiramatsu, W. Sawaki, I. Akaaski, J. Apl. Phys. 61 (1987) p 4540

[5] S. Nakaruma, T. Mukai, M. Senoh, Jpn. J. Aply. Phys. Part 2 32 (1993) p 8

[6] S. Nakurana, MRS Bull. 22 (1997) p 28

[7] S. Nakurana, Science. 281 (1998) p 956

[8] H. Morkoc, A. Di Carlo, R. Cingolani, Sol. St. Elec. 46 (2002) p 157

[9] S.C. Jain, M. Willander, J. Nayaran, R. Van Overstraeten, Apl. Phys. Rev. 87 (200) p 965

[10] M. Moll, Nucl. Instr. and Meth. A 511 (2003) p. 97

[11] 'GaN and Related Materials', G. Popovici, H. Morkoc, Gordon and Breach Science Publishers, 2001

[12] Surface Technology Systems, http://www.stsystems.com

[13] 'Semiconductor devices: Physics and technology', S.M. Sze, John Wiley and Sons, New York, 1985

[14] 'The science and technology of microelectronic fabrication', S.A. Campbell, Oxford University Press, New York, 2001

[15] Course notes for 'Micro-and nano-electronics fabrication' by Prof. C.D.W. Wilkinson, Dept. of Electrical and Electronic Engineering, University of Glasgow, 2000

[16] G Pellegrini, P. Roy, A. Al-Ajili, R. Bates, L. Haddad, M. Horn, K. Mathieson, J. Melone, V. O'Shea, K. M. Smith, I. Thayne and M. Rahman, Nucl. Instr. and Meth. A 504, (2003) p 149

[17] Industrial plasma engineering, Volume 1, J.R. Roth, Institute of physics publishing, 2000

[18] J. Bhardwaj, H. Ashraf, A. McQuarrie, Surface Technology Systems, Internal Publication

[19] Industrial plasma engineering, Volume 2, J.R. Roth, Institute of physics publishing, 2000

[20] S.A. McAuley, H. Ashraf, L. Atabo, A. Chambers, S. Hall, J. Hopkins, G. Nicholls, J. Phys. D: Apl. Phys. 34 (2001) p 2769

[21] H. Ashraf et al., 'Dry Silicon etching for MEMS', Symposium on Microstructures and Microfabricated Systems" at the Annual meeting of the electrochemical society, Montreal, Quebec, Canada May 4-9, 1997

[22] H. Ashraf et al., 'Defining Condition for the etching of Silicon in an ICP reactor', Materials Research Society Fall Meeting, Boston Massachusetts, USA, Nov 29 - Dec 03, 1998

[23] 'Physics of semiconductor devices, 2^{nd} edition', S.M. Sze, John Wiley and sons, New York, 1981

[24] 'Metal semiconductor contacts, 2^{nd} edition', E.H. Rhoderick, E.H. Williams, Oxford University Press, 1988

[25] Radiation detection and measurment, 3^{rd} edition', G.F. Knoll, John Wiley and sons, 1999

[26] International society for optical engineering, http://www.spie.org/web/oer/february/feb99/home.html

[27] 'Principles of Semiconductor devices', B. Van Zeghbroeck, http://ece-www.colorado.edu/ bart/book/book/chapter3/ch3-3.htm

[28] S. Ramo, Proc. IRE 27 (1939) p 584

[29] J.F. Ziegler, J.P. Biersack, IBM-Research, Yorktown Heights, New York, USA, 1996

[30] G. Pellegrini 'Technology & Development of 3D detectors for High Energy Physics and Medical Imaging' PhD Thesis, University of Glasgow (2002)

[31] F. Gianotti et al. hep-ph/0204087 Apr (2002)

[32] M. Moll, 'Radiation Damage in Silicon Particle Detectors', PhD Thesis, University of Hamburg (1999)

[33] Particle Data Group, Phys. Lett. B 592 (2004) p 1

[34] K. Saarinen, T. Suski, I. Grzegory, D.C. Look, Physica B 77 (2001), p 308

[35] S.J. Zinkle, C. Kinoshita, J Nucl. Mater. 251 (1997) p 200

[36] G. Lindstrom, A. Vasilescu, Displacement Damage in Silicon, http://sesam.desy.de/members/gunnar/Si-dfuncs.html

[37] J. Lindhard et al., Mat. Fys. Medd. Dan. Vid Selsk 33 (1963) p 14

[38] G. Lindstrom. Nucl. Instr. and Meth. A 512, (2003) p 30

[39] A. Chilingarov, J.S. Meyer, T. Sloan, Nucl. Instr. and Meth. A 395, Issues 1-2 ,(1997) p 35

[40] K.K. Lee, T. Ohshima, A. Saint, T. Kamiya, D.N. Jamieson, H. Itoh, Nucl. Instr. and Meth. B 210, (2003) p 489

[41] S. Dittongo, 'Studies of bulk damage induced in different silicon materials by 900 MeV electron irradiation', 4^{th} International Workshop on Radiation Imaging Detectors, Glasgow, UK, 25-29 July, 2004

[42] NIST ESTAR database, http://physics.nist.gov/PhysRefData/Star/Text/ESTAR.html

[43] T. Dubbs et al., IEEE Trans. Nucl. Sci. NS-46 (1999) p 839

[44] T. Wang, T. Shirahama, H.B. Sun, H.X. Wang, J. Bai and S. Sakai, Apl. Phys. Lett. 76 (2000) p 2220

[45] D. Zontar, V. Cindro, G. Kramberger, M. Mikuz, Nucl. Instr. and Meth. A 426 (1999) p 51

[46] M. Rogalla, K. Runge, A. Soldner-Rembold, Nucl. Phys. B 78 (1999) p 516

[47] Imperial College Reactor Centre, http://www.imperial-consultants.co.uk

[48] G. Casse, LHCb UK Collaboration Meeting, July (2004)

[49] Technologies & Devices Int., http://www.tdii.com/ganbulk.htm

[50] H. Kagan, 'Diamond (Radiation) Detectors Are Forever', 4th International Workshop on Radiation Imaging Detectors, Glasgow, UK, 25-29 July, 2004

[51] Emcore Corporation, http://www.emcore.com

[52] R. Dingle, I. Ilegems, Solid State Commun. 9 (1971) p 175

[53] O. Lagerstedt, A. Monemar. J. Apl. Phys. 45 (1974) p 2266

[54] V.S. Vavilov, S.I. Makarov, M.V. Chukichev, I.F. Chetverikova. Sov. Phys. Semicond. 13 (1979) p 1259

[55] 'Properties of Advanced Semiconductor Materials GaN, AlN, InN, BN, SiC, SiGe', V.Bougrov, M.E. Levinshtein, S.L. Rumyantsev, A. Zubrilov, John Wiley and Sons, New York, 2001,

[56] National Renewable energy laboratory http://www.nrel.gov/

[57] R. Y. Korotkov, M. A. Reshchikov, B. W. Wessels. Physics B 325 (2001) p 1

[58] Z. C. Huang, K. Xie, C. R. Wie, Rev. Sci. Instrum. 62 (1991) p 1951

[59] M. Albrecht, H. P. Strunk, J. L. Wehher, I. Grzegory, S. Poworski, T. Wosinski. J. Apl. Phys. 92 (2002) p 2000

[60] E. Gaubas, K. Kazukauskas, R. Tomasiunas, J. Vaitkus, A. Zukauskas. Apl. Phys. Lett. 84 (2004) p 5258

[61] A.Y. Polyakov, N.B. Smirnov, A.S. Usikov, A.V. Govorkov, B.V. P ushyini, Solid St. Electron. 42 (1998) p 1959

[62] Compound Semiconductor Technologies, http://www.compoundsemi.co.uk

[63] E. Gaubas, J. Vaitkus, K.M. Smith, Nucl. Instr. and Meth. A 460 (2001) p 35

[64] E. Gaubas, A. Kaniava, J. Vaitkus., Semicond. Sci. Tchnol. 12 (1997) p 1

[65] J. Vanhellemont, E. Gaubas, J. Apl. Phys. 80 (1996) p 6293

[66] A. Y. Polyakov, N. B. Smirnov, A. V. Govorkov, J. M. Redwing, Solid State Electron. 42 (1998) p 831

[67] P. Hacke, H. Nayakama, T. Detchprohm, K. Hiramatsu, N. Sawaki, Apl. Phys. Lett. 68 (1996) p 1362

[68] Y. Shon et al., Current Apl. Phys. 1 (2001) p 191

[69] Z.C. Haung, J.C. Chen, D. Wickenden, J. Crys. Growth. 170 (1997) p 362

[70] S.N. Mohammad, H. Morkoc, Prog. Quant. Electr. 20 (1996) p 361

[71] M. Razeghi, A. Rogalski, J. Apl. Phys. 79 (1996) p 7433

[72] S. Manolopoulos, (Al)GaN VUV detectors for proteomics, 3^{rd} International Workshop on Radiation Imaging Detectors, Riga, Latvia, 7-11 September, 2003

[73] E. Monroy, F. Calle, J.L. Pau, E. Munoz, F. Omnes, B. Beaumont, P. Gibart, Journal Crys. Gro. 230 (2001) p 537

[74] E. Monroy, F. Calle, E. Munoz, F. Omnes, B. Beaumont, P. Gibart, Journal Elect. Mat. 28 (1999) p 238

[75] J.J.L. Pau, E. Monroy, F.B. Naranjo, E. Munoz, F. Calle, M.A Sanchez-Garcia, Apl. Phys. Lett. 76 (2000) p 2785

[76] E. Monroy, M. Hamilton, D. Walker, P. Kung, F. J. Sánchez, M. Razeghi, Apl. Phys. Lett. 74 (1999) p 1171

[77] E. Monroy, F. Calle, E. Munoz, F. Omnes, Apl. Phys. Lett. 74 (1999) p 3401

[78] H.M. Chen, Y.F. Chen, M.C. Lee, M.S. Feng, J. Apl. Phys. 82 (1997) p 899

[79] C. Touzi, A. Rebey, B. Eljani, Mic. Elec. J. 33 (2002) p 961

[80] Rutherford Appleton Laboratory (RAL) http://www.cclrc.ac.uk

[81] T. Wang. T. Shirahama, H.B. Sun H.X. Wang, J. Bai, S. Sakai, H. Misawa, Apl. Phys. Lett. 76 (2000) p 2220

[82] L. Chernyak, A. Osinsky, H. Temkin, J.W. Yang, Q. Chen, M.A. Khan, Apl. Phys. Lett. 69 (1996) p 2531

[83] E. Monroy, T. Palacios, O. Hainout, F. Omnes, F. Calle, J.F. Hochendez, Apl. Phys. Lett. 80 (2002) p 3198

[84] B.A. Wallace, R. W. Janes, Curr. Opin. Chem. Bio. 5 (2001) p 567.

[85] S. Parker, C.J. Kenney, J. Segal, Nucl. Instr. and Meth. A 395 (1997) p 328

[86] L. Zhang, M. Abreu, V. Eremin, V. Granata, J. Mariano, P.R. Mendes, T.O. Niinikoski, P. Sousa, E. Verbitskaya, W. Zhang, IEEE Trans. Nucl. Sci 49 (2002) p 1040

[87] F.Moscatelli et al. 'Radiation hardness simulation of silicon thin detectors', 4th RD50 Workshop on Radiation hard semiconductor devices for very high luminosity colliders, CERN, 5-7 May, 2004

[88] S. Parker, C.J. Kenney, IEEE Trans. Nucl. Sci. Vol 48 N5 (2001) p 1629

[89] S. Parker, 'Semiconductor track detectors: a brief history from 0D to 3D', 4th International Workshop on Radiation Imaging Detectors, Glasgow, UK, 25-29 July, 2004

[90] Oxford Technologies, www.oxfordplasma.de/process/gaas-icp.htm